



HAL
open science

Image reconstruction for three-gamma PET imaging

Debora Giovagnoli

► **To cite this version:**

Debora Giovagnoli. Image reconstruction for three-gamma PET imaging. Medical Imaging. Ecole nationale supérieure Mines-Télécom Atlantique, 2020. English. NNT : 2020IMTA0219 . tel-03123557

HAL Id: tel-03123557

<https://theses.hal.science/tel-03123557>

Submitted on 28 Jan 2021

HAL is a multi-disciplinary open access archive for the deposit and dissemination of scientific research documents, whether they are published or not. The documents may come from teaching and research institutions in France or abroad, or from public or private research centers.

L'archive ouverte pluridisciplinaire **HAL**, est destinée au dépôt et à la diffusion de documents scientifiques de niveau recherche, publiés ou non, émanant des établissements d'enseignement et de recherche français ou étrangers, des laboratoires publics ou privés.

THESE DE DOCTORAT DE

L'ÉCOLE NATIONALE SUPERIEURE MINES-TELECOM ATLANTIQUE
BRETAGNE PAYS DE LA LOIRE - IMT ATLANTIQUE

ÉCOLE DOCTORALE N° 601
*Mathématiques et Sciences et Technologies
de l'Information et de la Communication*
Spécialité : Image, signal, vision

Par

Debora GIOVAGNOLI

Image Reconstruction for Three-gamma PET Imaging

Thèse présentée et soutenue à Brest le 27/11/2020
Unité de recherche : Latim U1101
Thèse N° : 2020IMTA0219

Rapporteurs avant soutenance :

David Brasse	Chercheur CNRS IPHC Strasbourg, France
Antonio Gonzalez Martinez	Researcher, Spanish National Research Council, Madrid, Spain

Composition du Jury :

Président :	
Dominique Thers	Maitre de conférences, HDR, IMT-Atlantique, Subatech, Nantes, France

Examineurs :	
David Brasse	Chercheur CNRS IPHC Strasbourg, France
Antonio Gonzalez Martinez	Researcher, Spanish National Research Council, Madrid, Spain
Sara Diglio	Chercheur CNRS Subatech, Nantes, France
Lucia Gallego-Manzano	Researcher, Cern, Switzerland

Dir. de thèse : Dimitris Visvikis	Directeur de recherche INSERM, Latim, Brest
Invité : Alexandre Bousse	Maitre de conférences, HDR, UBO, Brest

A collaboration between

Latim U1101, Brest, under the supervision of Dimitris Visvikis



and Subatech, Nantes, under the supervision of Dominique Thers



Declaration of Authorship

I, Debora Giovagnoli, declare that this thesis titled, "Image Reconstruction for Three-gamma PET Imaging" and the work presented in it are my own. I confirm that:

- This work was done wholly or mainly while in candidature for a research degree at this University.
- Where any part of this thesis has previously been submitted for a degree or any other qualification at this University or any other institution, this has been clearly stated.
- Where I have consulted the published work of others, this is always clearly attributed.
- Where I have quoted from the work of others, the source is always given. With the exception of such quotations, this thesis is entirely my own work.
- I have acknowledged all main sources of help.
- Where the thesis is based on work done by myself jointly with others, I have made clear exactly what was done by others and what I have contributed myself.

Signed:



Date:

27/11/2020

Contents

Declaration of Authorship	i
Contents	iii
List of Figures	vii
List of Tables	xiii
List of Acronyms	xv
Resumé	1
Introduction	19
1 General principles of nuclear imaging	23
1.1 Introduction	24
1.2 Physical principles	24
1.2.1 Radioactive decay	24
Mathematics of radioactive decay	26
1.2.2 Charged particle's energy loss	26
1.2.3 Positron range	27
1.2.4 Photon interactions with matter	28
1.2.5 Photon attenuation	32
1.3 PET imaging	33
1.3.1 Detection	34
Scintillation in LXe	35
Photodetectors	35
1.3.2 Coincidences	36
1.3.3 Sensitivity and Depth Of Interaction	37
1.3.4 Time of Flight PET	38

2	Image Reconstruction	41
2.1	Introduction	42
2.2	Data acquisition	43
2.2.1	Deadtime	44
2.3	Analytic Image Reconstruction	44
2.3.1	2D analytic image reconstruction	45
2.3.2	Back-projection	47
2.3.3	3D analytic image reconstruction	49
2.3.4	Back-projection	50
2.4	Model-based Image Reconstruction	51
2.4.1	Iterative algorithms	53
2.5	System modelization and corrections	58
2.6	System matrix	58
2.6.1	Detector geometry	59
2.6.2	Attenuation and normalization	59
2.6.3	Positron range	60
2.7	Scattering and random coincidences	60
3	3-γ Image Reconstruction	63
3.1	Introduction	64
3.2	The XEMIS2 project	65
3.2.1	Scanner geometry	65
3.2.2	Radio-isotope	66
3.2.3	Detection	67
3.3	Proposed 3- γ image reconstruction technique	69
3.3.1	LOR/cone intersection	69
3.3.2	Requirements for 3- γ imaging	72
	Energy resolution	72
	Spatial resolution	74
	Angular resolution	75
3.3.3	Pseudo-TOF image reconstruction	76
3.4	Simulation	79
3.4.1	Phantoms	80
3.5	Image reconstruction software	82
3.5.1	Pseudo-TOF system matrix	82
3.5.2	Pseudo-TOF algorithm in CASToR	83
3.5.3	XEMIS2 geometry in CASToR	84

Sensitivity image	86
4 Results	87
4.1 Introduction	87
4.2 Figures of merit	88
4.2.1 NEMA-like phantom analysis	88
4.2.2 Digimouse phantom analysis	89
4.3 NEMA-like phantom results	90
4.4 Digimouse phantom results	91
4.5 Discussion	95
5 Positron range correction	99
5.1 Introduction	100
5.2 Positron range estimation	101
5.3 Positron range correction	103
5.3.1 Positron range reduction	103
5.3.2 Positron range correction pre-, post- and during recon- struction	103
5.4 Proposed correction	106
5.4.1 Simulation and phantoms	106
5.4.2 Reconstruction and positron range correction estimation	107
5.5 Results	109
5.5.1 Figures of Merit	109
5.5.2 Invariant and variant kernel convolution	110
5.6 Discussion	112
Conclusion and perspectives	117
Bibliography	123
Publications and Oral Communications	143

List of Figures

1	Geometrie du xenon medical imaging system 2 (XEMIS2). . .	4
2	Vision transversale du scanner.	4
3	Schéma de la désintégration β du Sc-44 [1].	5
4	Influence de l'erreur lie a l'angle Compton sur la LOR.	7
5	(a) Événement sans diffusion. (b) Événement où un des photons diffuse avant d'être détecté. (c) Événement où le troisième gamma diffuse dans le corps.	8
6	Étude sur d , la distance entre la projection du point d'émission du troisième gamma sur la LOR et les coordonnées LCI.	9
7	Incertitude sur la position du LCI.	9
8	Coupe axiale du fantôme type NEMA.	10
9	Coupe axiale du Digimouse avec les structures internes.	11
10	Coupe axiale du fantôme type NEMA après avoir applique un filtre gaussien ($\sigma = 1$ mm). Images reconstruite utilisant (a) reconstruction TEP classique, et la technique proposée dans ce travail (3- γ) avec (b) 70-ps et (c) un écart type variable événement par événement. Les images sont les résultats a la 30 th itération. (d), (e) et (f) montrent les profiles sur la ligne jaune.	12
11	Images reconstruites du Digimouse: reconstruction 2- γ , reconstruction pseudo-TOF avec un ecart type de 200 ps, 150 ps, 100 ps, et 70 ps.	13
12	Profile sur la ligne qui croise la ROI dans le cerveau du Digimouse.	13
13	Coupe axiale du fantôme pour l'étude sur la correction de range du positon.	14
14	Coupe transversale du fantome. Images reconstruites avec differents techniques: (a) TEP classique et (b) 3- γ , pas corrigeé; (c) 2- γ et (d) 3- γ convolues avec des noyaux variantes, (e) 2- γ et (f) 3- γ convolues avec un noyau stationaire.	16
15	Profile sur la ligne jaune.	17

1.1	Positron emission and annihilation scheme for Fluor-18 (F-18) [29].	25
1.2	Normalized energy spectra distributions for Scandium-44 (Sc-44) (green) and F-18 (blue).	29
1.3	Scheme of positron decay: the range r is the distance from the annihilation point. The real effect is the line of response (LOR) displacement, measured as the distance d between the annihilation point and the LOR.	29
1.4	The Klein-Nishina distribution of Compton scattering angles over a various range of energies.	30
1.5	Photon interactions with matter: (a) photoelectric effect, (b) Compton scattering and (c) pair production [43].	31
1.6	Main photon interactions versus photon energies for different atomic number [43].	32
1.7	Complete process of a positron emission tomography (PET) scan exam [53].	34
1.8	Schematic functioning of a photomultiplier (PMT).	36
1.9	Event 1 represents a double scattered event, events 2 and 3 show a random coincidence. [29]	37
1.10	Parallax error due to the unknown event depth of interaction (DOI) [29].	37
1.11	time of flight (TOF)-PET scan model: A and B represent the detectors and X the position of the annihilation respect to the scanner center. The time registered in A and B is proportional to the distance TOF_A and TOF_B [60].	38
1.12	(a) classical PET reconstruction, (B) TOF probability, in which the time resolution δt limits the number of voxels contributing to the event [60].	39
2.1	From projections to sinograms. [29]	43
2.2	Projection of an image and its Radon transform [68].	45
2.3	Central section theorem in 2D [72].	47
2.4	Integral of a two-dimensional (2D) plane used for the Radon transform of a 3D object [75].	49
2.5	From left to right: reconstructions from fully 3D PET data on the left, 2D rebinned non-TOF, three-dimensional (3D) rebinned non-TOF and fully 3D PET-TOF [82].	50

2.6	Convergence properties of maximum likelihood expectation maximization (MLEM) algorithm from simulated SPECT brain data. First row noise-free images, second row noisy, third row noisy filtered reconstruction [92].	56
2.7	The images show the iterated image estimates of ordered subset expectation maximization (OSEM) for single photon emission tomography (SPECT) brain data. For every image, we indicate the iteration number while the subsets number is reported on the left of each row [92].	57
3.1	Transversal view of the scanner to show where the small animal is positioned, how the three gammas are emitted and where they are detected.	66
3.2	Scheme of the XEMIS2: layer and dimensions for one quarter of the scanner, the rest being similar through symmetry.	67
3.3	XEMIS2 experimental setup at the Subatech laboratory: on the left the cryostat and on the right the camera.	68
3.4	Decay scheme of Sc-44 [1].	68
3.5	Vectorial diagram of the cone/LOR intersection: C and A are respectively the first and second third-gamma interaction point, $\theta = \theta_C$ is the scattering angle, the vector D represents the LOR direction and the points P and Q the two intersections between the cone and the infinite line.	70
3.6	Scheme of the influence of the scattering angle's error on the LOR.	72
3.7	(a) Event with no scattering. (b) Event in which one coincidence photon scatters with a small angle before reaching the liquid xenon (LXe), causing a change in the LOR/cone intersection (LCI) coordinates. (c) Event with an 1157-keV gamma scatter in the phantom: depending on the angle width the cone can or not intersect the LOR, anyways the LCI determination is highly affected.	73
3.8	Scheme of the vectors involved in the spatial resolution calculation.	74

3.9	(a) Angular resolution as a function of the scatter angle, in red the energy resolution, in green the spatial resolution, in black the total resolution. (b) The recoil energy of the electron coming from Compton scattering as a function of the scatter angle. The red lines determine the energy interval in which we have an acceptable angular resolution [4].	75
3.10	Probability on the LOR for different image reconstruction techniques: (a) classical PET with a uniform probability, (b) TOF-PET with a Gaussian distribution in which the full width half maximum (FWHM) is due to the time resolution and (c) pseudo-TOF with a Gaussian distribution centered on the LCI coordinates.	77
3.11	LCI coordinates' uncertainty scheme: d is the distance between the projection of the third-gamma emission point on the LOR and the LCI coordinates computed through the geometrical intersection.	78
3.12	Study on the LCI coordinates' uncertainty on a NEMA-like phantom: in the histograms the distance between the computed LCI coordinates and the projection of the third-gamma emission point on the LOR.	78
3.13	Overview of the XEMIS2 simulated as a multi-layer cylinder in Geant4 Application for Emission Tomography (GATE). We can see the phantom in pink, the LXe in green and the PMTs around the active volume in red.	79
3.14	Axial view of the central slice of the NEMA-like phantom showing the five hot spheres of 2, 4, 8, 10, and 12-mm radius.	80
3.15	Axial view of the central slice of the Digmouse phantom showing some of the internal structures.	81
3.16	Virtual elements discretization of a monolithic detector: from 8 detector blocks to 32 virtual elements.	84

3.17	(a) Discretization of the XEMIS2 considering the total active volume, we obtain 234337008 virtual elements, a number too high to be treated by any software in a reasonable amount of time. (b) Discretization of the XEMIS2 considering only the first layer around the field of view (FOV). In (c) we show how the events are registered: the LOR length considered in customizable and advanced software for tomographic reconstruction (CASToR) is the length between the two red elements, whose element ID is used during reconstruction to get the event LOR position.	85
4.1	Transaxial section of the Digimouse phantom mask to show the volume of interest (VOI) (red sphere) and the 4 background (green, purple, blue and yellow).	90
4.2	Transversal view of the central slice of the NEMA-like phantom at the 30 th iteration and plot profiles along the yellow line crossing two spheres. We show results for (a, d) conventional two-gamma ($2\text{-}\gamma$) reconstruction, (b, e) proposed pseudo-TOF approach with a Gaussian standard deviation of 70 ps and (c, f) with an event-by-event variant pseudo-TOF resolution.	91
4.3	Axial view of the NEMA phantom after Gaussian filtering ($\sigma = 1$ mm) using (a) classical PET reconstruction and the proposed three-gamma ($3\text{-}\gamma$) technique with (b) 70-ps and (c) variant standard deviation. Images are the results of the 30 th iteration. In (d), (e) and (f) the corresponding plot profiles along the yellow line. The high contrast ring around the FOV in the first image on the left is due to a CASToR misinterpretation of the activity value on the FOV edge and it does not affect image reconstruction.	92
4.4	Sphere-by-sphere metrics results, from top to bottom the (1) 2-mm, (2) 4-mm, (3) 8-mm, (4) 10-mm, and (5) 12-mm radius sphere with the respective values of signal to noise ratio (SNR), contrast to noise ratio (CNR) and recovery coefficient (RC).	93
4.5	Reconstructed images of the Digimouse, from left to right: $2\text{-}\gamma$ reconstruction, pseudo-TOF with 200-ps, 150-ps, 100-ps, and 70-ps resolution.	94
4.6	Metrics results of the Digimouse reconstruction	94

4.7	Line profile plot of the mouse's head's hot spot for all the different reconstructions on the last iteration.	95
5.1	Fractional energy loss for positron and electrons in lead as a function of the particle energy [189].	102
5.2	Reconstructed images using different positron range correction, β indicates the noise level [203].	105
5.3	Axial view of the central slice of the phantom showing the three spheres of 2, 4, and 8-mm radius made of water and the two with a 10 and 12-mm radius made of lung and bone.	107
5.4	Transaxial view of the central slice of the point spread function (PSF) study phantoms showing the three point-source spheres made of bone, water and lung, from left to right.	108
5.5	PSF plot and Gaussian fit for the bone sphere in (0, 0, -60). . .	109
5.6	PSF plot and Gaussian fit for the water sphere in (0, 0, 0). . . .	109
5.7	PSF plot and Gaussian fit for the lung sphere in (0, 0, 60). . . .	110
5.8	Transaxial view of the NEMA-like phantom, reconstructed with four different techniques: (a) conventional 2- γ PET and (b) 3- γ , with no positron range correction; (c) 2- γ and (d) 3- γ reconstruction convolved with a variant kernel, (e) 2- γ and (f) 3- γ reconstruction convolved with a stationary kernel.	111
5.9	Plot profiles of the six different reconstructions through the yellow line seen in Fig. 5.8.	112
5.10	SNR and CNR plots of the three smallest spheres, water-made: in numerical order sphere of 2-mm, 4-mm and 8-mm radius. With "conv" we refer to variant kernel convolution, while "stat conv" refers to the invariant kernel convolution correction. . . .	113
5.11	SNR and CNR plots of the two biggest spheres: sphere number 4, 10-mm radius with lung density and sphere number 5, 12-mm radius with bone density. With "conv" we refer to variant kernel convolution, while "stat conv" refers to the invariant kernel convolution correction.	114
5.12	Distance study to determine the D_{cut} to use in the interactions clustering.	118

List of Tables

1	Dimensions et positions des cinq sphères dans le fantôme. . .	10
2	Biodistribution du [⁴⁴ Sc]Sc-J591 dans le corp du Digimouse. .	11
3	Description des sphères a l'intérieur du fantôme.	14
1.1	Mean positron range in water for isotopes of interest in PET [40, 41].	28
1.2	Common radiotracers and some of their specific applications.	33
1.3	Physical properties of some common detectors in PET.	34
3.1	Dimensions and coordinates of the five hot spheres in the phantom, the origin being the center of the scanner.	80
3.2	Radiopharmaceutical uptake distribution for the mouse phantom with $0.8 \times 0.8 \times 0.8$ -mm ³ voxels: [⁴⁴ Sc]Sc-J591 uptake values in the Digimouse computed from the data in Holland, 2010 [3].	81
4.1	Percentage gain in SNR for pseudo-TOF over non-TOF for all spheres, computed on the last iteration.	92
4.2	Percentage gain in CNR for pseudo-TOF over non-TOF for all spheres, computed on the last iteration.	92
5.1	Some positron range properties of common radioisotopes used in PET imaging.	100
5.2	Description of the spheres in the cylindrical phantom: reference number, position in mm considering the center of the FOV as the origin, and radius size.	107
5.3	Transaxial and axial FWHM values of the kernel used to correct for Sc-44 positron range in water, bone and lung.	108

List of Acronyms

Acronyms

2D two-dimensional

2- γ two-gamma

3D three-dimensional

3- γ three-gamma

ART algebraic reconstruction technique

Bi₄Ge₃O₁₂ bismuth germanate

BR branching ratio

Ca-44 Calcium-44

Ca*-44 Calcium*-44

CASToR customizable and advanced software for tomographic reconstruction

CNR contrast to noise ratio

CSP collision stopping power

CT computed tomography

DOI depth of interaction

F-18 Fluor-18

FBP filtered backprojection

FOV field of view

FWHM full width half maximum

GATE Geant4 Application for Emission Tomography

Geant4 GEometry ANd Tracking

Gd₂SiO₅ gadolinium oxyorthosilicate

GT ground truth

LCI LOR/cone intersection

LM list mode

LMEM list-mode expectation maximization

LOR line of response

LS least-square

Lu₂SiO₅ lutetium oxyorthosilicate

LXe liquid xenon

MART multiplicative algebraic reconstruction technique (ART)

ML maximum-likelihood

MLEM maximum likelihood expectation maximization

MRI magnetic resonance imaging

Na-22 Sodium-22

OSEM ordered subset expectation maximization

PDF probability distribution function

PET positron emission tomography

PMT photomultiplier

PSF point spread function

RC recovery coefficient

RMS root mean square

ROI region of interest

RSP radiation stopping power

SART simultaneous ART

Sc-44 Scandium-44

SIRT simultaneous iterative reconstruction technique

SM system matrix

SNR signal to noise ratio

SPECT single photon emission tomography

SSS single scatter simulation

TOF time of flight

TPC time-projection chamber

VOI volume of interest

VOR volume of response

WLS weighted-least squares

XEMIS xenon medical imaging system

XEMIS1 xenon medical imaging system 1

XEMIS2 xenon medical imaging system 2

*A Vincent e a Jean,
per avermi resa mamma
prima di diventare dottore.*

Resumé

Note: the following chapter is a resumé in French from a non-mother tongue speaker, it is not 100% accurate, nevertheless it is a clear sum up of the work I carried on, and please appreciate the effort.

On peut considérer que la médecine nucléaire clinique a commencé dès 1927 avec l'analyse de la circulation sanguine normale et pathologique par Blumgart et Weiss par l'utilisation du radio-isotope Bi^{214} . Les premiers détecteurs médicaux, principalement issus de la physique expérimentale nucléaire, étaient constitués de scintillateurs couplés à des photomultiplicateurs via un guide d'onde pour lire le signal. Dans les années 1970, les systèmes de tomodensitométrie ont été inventés suite à la découverte des principes de reconstruction tomographique. Dans les mêmes années, l'imagerie de résonance magnétique a été développée, et plus tard, les systèmes d'imagerie de tomographie d'émission de reconstruction (TEP) et de tomographie d'émission monophotonique (TEMP).

Aujourd'hui, la médecine nucléaire permet l'étude de la biologie *in vivo* et des processus métaboliques dans le corps utilisant principalement deux modalités d'imagerie fonctionnelles : l'imagerie TEMP et TEP. Ces deux modalités d'imagerie sont basées sur l'utilisation de radiopharmaceutiques (ou radiotraceurs), dont la biodistribution dans le corps peut être évaluée par détection externe en utilisant la reconstruction tomographique. Le radiotraceur est composé d'une substance qui suit un processus physiologique, marqué par un isotope radioactif qui émet un rayonnement détectable depuis l'extérieur du corps. Pour le diagnostic TEMP, le radiopharmaceutique est un émetteur d'un seul photon, détecté par une caméra gamma tournant autour du patient, tandis que dans les études TEP, des émetteurs de positons sont utilisés et la détection se produit dans un détecteur de forme annulaire autour du patient.

Bien que l'imagerie nucléaire permette d'améliorer le dépistage, le diagnostic et le suivi de plusieurs maladies, elle introduit également certains risques liés à la radio-exposition. De nos jours, les facteurs qui guident la recherche et le développement de l'imagerie nucléaire sont principalement la réduction de la dose et la réduction du temps d'acquisition, pour des raisons autant pratiques qu'en terme de sûreté radiologique.

Ces deux facteurs ont une influence critique sur la qualité de l'image car le rapport signal sur bruit (SNR) dépend principalement du nombre de photons dans les détecteurs. Pour maintenir des normes de qualité d'image requises par la médecine moderne tout en diminuant l'activité totale, un certain nombre de méthodes software de traitement d'image ont été mises en œuvre en parallèle de l'utilisation de nouveaux systèmes d'imagerie.

De nouveaux systèmes, appelés TOF-PET (imagerie temps de vol), ont d'abord été conçus dans les années 1970. Leur objectif est de mesurer la différence de temps entre les deux arrivées de photons par coïncidence dans des détecteurs opposés dans l'espace pour estimer la position le long de la ligne de réponse (LOR) où l'annihilation a eu lieu. L'incertitude de localisation est déterminée par la résolution temporelle du détecteur, qui peut être caractérisée par la largeur à mi-hauteur de la distribution centrée sur $x = c \cdot \Delta t$, où c est la vitesse de la lumière et Δt la différence de temps. En utilisant un détecteur idéal avec une résolution temporelle infiniment précise, on pourrait localiser exactement la position d'annihilation et donc avoir directement accès à la biodistribution des radiotraceurs. Cependant, en raison des limites de techniques d'instrumentation actuelles, les techniques tomographiques sont toujours nécessaires.

Les algorithmes utilisés pour reconstruire les images tomographiques peuvent être classés en deux groupes principaux: les méthodes analytiques et itératives. Dans le premier cas, nous traitons un problème d'inversion entre une fonction et son intégrale curviligne. Dans le second cas, nous modélisons tous les aspects possibles de l'acquisition de données et toutes les interactions physiques qui peuvent se produire et nous cherchons l'image qui correspond le mieux aux données de manière itérative. Les données sur lesquelles nous basons notre la reconstruction sont acquises en détectant des photons de coïncidence de 511 keV en TEP et photons uniques en SPECT. Dans les deux cas, le nombre limité d'événements

et le comportement stochastique des particules entraîne l'apparition de

bruit. Historiquement, la justification du passage d'une reconstruction d'image analytique à une reconstruction d'image itérative était liée à une meilleure modélisation du bruit par les algorithmes itératifs. Shepp et Vardi ont été les premiers à proposer une méthode MLEM qui a montré une amélioration significative sur l'approche de rétroprojection filtrée (FBP). Aujourd'hui l'algorithme de reconstruction d'image le plus utilisé est basé sur leur premier modèle et ses variations (LM-MLEM, OSEM).

Dans cette thèse, nous présentons l'imagerie three-gamma ($3\text{-}\gamma$), où le système d'imagerie repose sur le principe de l'acquisition de trois photons gammas, venants d'un émetteur β^+ et γ . Les motivations du principe de l'imagerie $3\text{-}\gamma$ sont que les informations de détection du troisième gamma peuvent aider à fournir une meilleure localisation du point d'annihilation, permettant ainsi une meilleure qualité d'image et moins de dose administrée au patient. Des détecteurs profitant d'un troisième gamma ont déjà été proposés dans un certain nombre d'études. Parmi ces efforts, nous présentons dans ce travail le XEMIS2, un scanner $3\text{-}\gamma$ préclinique développé à Nantes, France. Deux caractéristiques principales de XEMIS2 le rendent adapté à l'imagerie $3\text{-}\gamma$: l'utilisation du liquid xenon (LXe) comme milieu de scintillation, qui offre une géométrie continue, et l'utilisation du Scandium-44 (Sc-44), un émetteur β^+ et γ , qui permet la détection $3\text{-}\gamma$.

Le système XEMIS2 est une caméra corps entier pour le petit animal qui présente une géométrie particulière: un champ de vue allongé dans la direction axiale et un détecteur monolithique, afin de maximiser la sensibilité du scanner. Dans le système XEMIS2, à l'inverse de détecteurs cristaux ou bloc, tout le volume entourant le petit animal est rempli du milieu de détection LXe. Le scanner est un cylindre composé de deux TPCs remplis de LXe; les TPC sont placées côte à côte et séparées par une cathode partagée entre elles. La zone de détection active est située entre 7 cm de rayon intérieur au cylindre jusqu'à 19 cm de rayon extérieur et mesure 24 cm de long (12 cm pour chaque TPC).

Tout autour du cylindre détecteur, 380 PMTs sont utilisés pour détecter la lumière de scintillation générée pendant l'interaction photon-LXe. Un champ électrique homogène est appliqué entre la cathode et les anodes, afin de dériver les charges d'ionisation et les mesurer sur les anodes. Dans la Fig. 1, nous montrons un diagramme de la zone active, montrant seulement un quart du scanner, le reste étant symétrique. L'animal est positionné dans

le cylindre de 7 cm de rayon. Pour empêcher toute hypothermie, 7,5 mm de vide et un cylindre supplémentaire en acier inoxydable de 1,5 mm d'épaisseur sont placés autour du premier tuyau en aluminium.

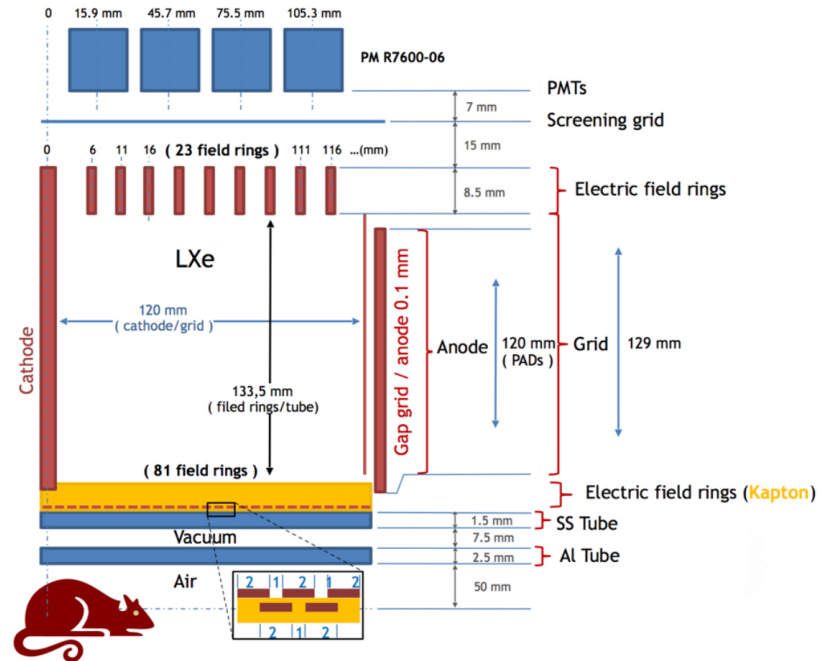


FIGURE 1: Geometrie du XEMIS2.

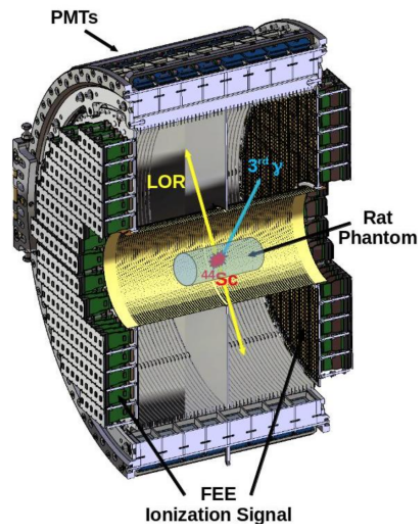


FIGURE 2: Vision transversale du scanner.

L'émetteur *trois gammas* (positon et γ) choisi pour le projet XEMIS2 est le Scandium-44. Ce radioisotope est un bon candidat pour notre étude en raison de sa durée de vie de 4 heures, idéal pour des applications médicales. L'interaction la plus probable se fait par la désintégration β , avec un rapport

d'embranchement (branching ratio, BR) = 94,27% lors de laquelle il transmute en Calcium*-44 (Ca^*-44) avec émission d'un positron et d'un neutrino. Le positron émis connaît un parcours dans le corps jusqu'à s'annihiler avec un électron de l'environnement, tandis que le Ca^*-44 se désexcite en émettant un photon de 1157 keV avec une distribution isotrope de probabilité dans l'espace (Fig. 3). Ainsi, le rayonnement que nous pouvons détecter est composé des deux gamma dos à dos générés lors de l'annihilation, et du troisième gamma émis pendant le processus de désexcitation. En raison des différences d'énergie entre les photons de coïncidence (511 keV) et le troisième gamma (1157 keV), nous sommes en principe en mesure de discriminer les interactions dans le processus d'acquisition, et nous pouvons également exclure les cas à trois gammas dérivant de l'état ortho-positronium pendant la désintégration du positron. Une caractéristique importante du Sc-44 comme émetteur de positons est le parcours du positon. La particule est émise dans une gamme d'énergie qui va de 0 à 1474 keV, ce qui conduit à une plage moyenne de positons de 2,4 mm, par rapport aux 0,5 mm du radio-isotope TEP le plus courant, le Fluor-18.

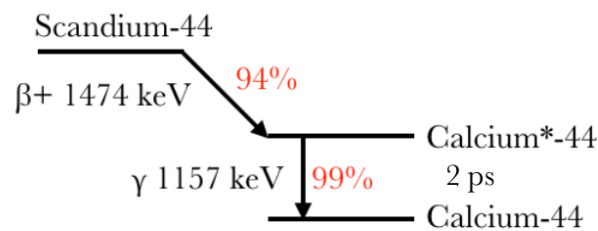


FIGURE 3: Schéma de la désintégration β du Sc-44 [1].

L'objectif de ce travail est de présenter une nouvelle méthode de reconstruction d'image basée sur la détection 3- γ ayant le double objectif de permettre une meilleure qualité d'image et une réduction de la dose administrée. Le principe de la reconstruction d'image 3- γ est basé sur l'utilisation des deux photons de coïncidence pour déterminer une ligne de réponse (LOR) et sur la détection d'un troisième gamma pour obtenir un cône Compton permettant d'affiner la localisation de la position d'annihilation sur la ligne de réponse. Le troisième photon est le plus susceptible de subir une diffusion Compton dans le LXe en raison de son énergie initiale plus élevée (1,157 MeV). L'objectif est ainsi d'identifier un cône Compton pour définir la direction dans laquelle le photon a été émis. Pour y parvenir, la connaissance de la position et de

l'énergie des deux premières interactions du troisième gamma dans LXe sont nécessaires. Une fois le cône construit, on l'intersecte avec la LOR pour obtenir les coordonnées de l'intersection cone-LOR (LCI). Ce point peut alors être identifié, lors de la reconstruction de l'image, au centre d'une densité Gaussienne de probabilité d'annihilation le long de la LOR de manière similaire à une différence temporelle en TOF, donnant lieu à l'appellation "pseudo-TOF" de la méthode proposée. Dans ce cas, nous avons conduit une étude sur la largeur de la distribution qui dépend non seulement de la résolution du scanner mais aussi de plusieurs facteurs (parcours du positon, résolution énergétique, diffusion Compton, etc.).

Le calcul est effectué pour un cône et une ligne infinis, ainsi seules les solutions à l'intérieur du FOV sont acceptées. Nous avons aussi décidé de supprimer tous les événements présentant une double intersection (2%), ainsi que les événements sans point commun entre la LOR et le cône (4%). Ces deux types d'événements se produisent principalement en raison de la diffusion Compton avant d'atteindre le détecteur. Il y a plusieurs couches métalliques entre le FOV et le volume LXe, qui augmentent la probabilité de diffusion avant détection, qui doivent alors être ajoutées à la probabilité déjà existante de diffusion dans le corps du patient. Cela peut conduire à une erreur de calcul du point d'intersection, soit par une erreur dans la LOR ou dans le calcul du cône. Nous voyons sur la Fig. 4 comment une petite erreur sur l'angle de Compton peut donner une incertitude beaucoup plus grande sur la LOR. Dans notre cas, où nous traitons de trois photons, des événements sans diffusion sont rares et même de petits écarts peuvent être un problème à la détermination de l'intersection LCI. La Fig. 5 montre des cas possibles: (a) un vrai événement, (b) un photon de coïncidence qui subit une diffusion dans les couches métalliques autour du FOV, et (c) un photon de 1157 keV qui se disperse dans le fantôme. D'autres cas peuvent également être liés à la diffusion dans le fantôme pour un, deux ou trois photons en même temps, etc. Toutes ces situations peuvent affecter la détermination correcte de la LCI, et l'incertitude sur le calcul des coordonnées doit être inclus dans la largeur de la gaussienne sur la LOR lors de la reconstruction d'image.

Le principal problème de l'imagerie 3- γ est l'utilisation des informations portées par le troisième gamma pour améliorer la reconstruction de l'image, en déterminant un cône Compton et le point de croisement entre cet objet et la LOR. La précision sur les coordonnées LCI dépend de plusieurs facteurs,

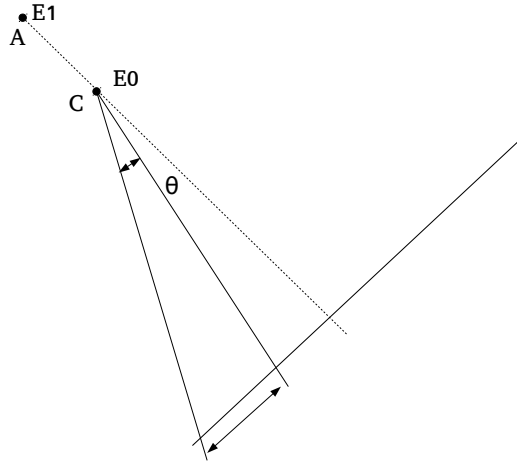


FIGURE 4: Influence de l'erreur lie a l'angle Compton sur la LOR.

parmi lesquels l'énergie et la résolution spatiale des interactions du troisième gamma, la distance entre les deux premières détections et la distance LOR-vertex du cone.

Comme déjà discuté dans la section sur les prérequis de l'imagerie 3- γ , le LCI peut être affecté par plusieurs effets: photon subissant une diffusion Compton dans le fantôme, parcours du positon, énergie du détecteur et résolution spatiale, distance entre les interactions, angle entre le cône et LOR, etc. Ainsi, nous devons introduire un paramètre de reconstruction appelé l'écart type de pseudo-TOF (pseudo TOF standard deviation) qui caractérise l'incertitude sur le LCI intégrant tous les effets possibles.

Afin de mesurer l'impact de tous les effets de biais sur cette LCI, nous avons étudié la distance d entre la LCI calculée et la projection sur la LOR du troisième point d'émission gamma (Fig. 6) grâce à une simulation d'un fantôme aux propriétés similaires au NEMA.

La Fig. 7 montre la distribution résultante: la courbe obtenue est large et montre un maximum en 0. Le RMS de cette courbe 22 mm a été utilisé et, qui se traduit par 70 ps en unités temporelles TOF.

L'utilisation d'un écart-type fixe dans la reconstruction sous-estime l'incertitude pour une partie des événements. Ainsi, deux reconstructions d'images différentes ont été effectuées. Nous avons utilisé la valeur de résolution de 70 ps résultant de l'étude de distance NEMA et une résolution pseudo-TOF variante, qui a été calculée événement par événement comme l'équivalent en temps de la distance d . En incorporant la LCI dans un système TEP et en tenant compte de l'incertitude relative, nous nous attendons à une amélioration des images

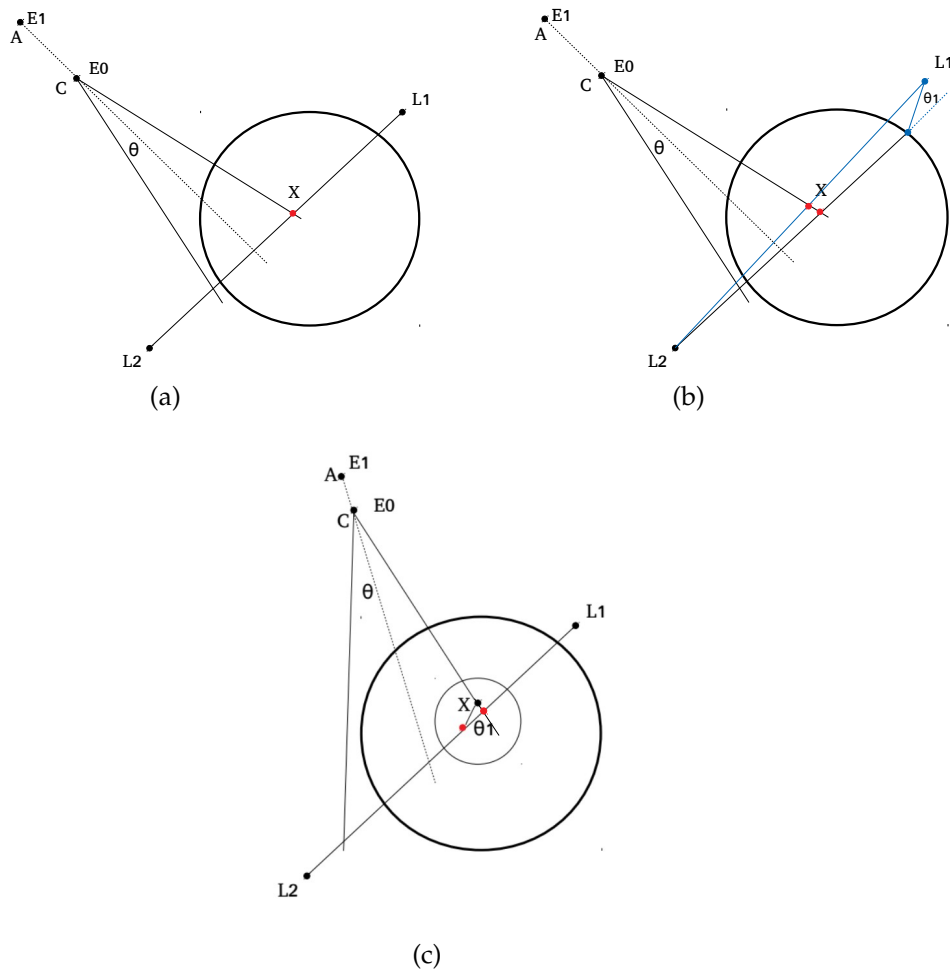


FIGURE 5: (a) Événement sans diffusion.
 (b) Événement où un des photons diffuse avant d'être détecté.
 (c) Événement où le troisième gamma diffuse dans le corps.

reconstruites. Cette idée est confortée par le fait que les scanners TOF ont déjà démontré des améliorations en terme de SNR et CNR par rapport aux systèmes TEP conventionnels.

Dans ce travail, nous explorons la méthode de reconstruction d'image pseudo-TOF et ses avantages et nous comparons la technique de reconstruction proposée à la reconstruction d'image 2- γ conventionnelle. Le premier fantôme simulé est un fantôme de type NEMA, en analogie avec les études de qualité d'image menées pour caractériser les détecteurs, et en général utilisé dans les comparaisons TOF versus non-TOF.

Le fantôme est constitué d'un cylindre d'eau homogène de 12 cm de long et d'un rayon de 3,5 cm, contenant cinq sphères. Les centres de toutes les sphères sont équidistants de l'axe central du cylindre et positionnés sur la tranche centrale du cylindre. Le rayon des sphères mesure 2, 4, 8, 10 et 12 mm,

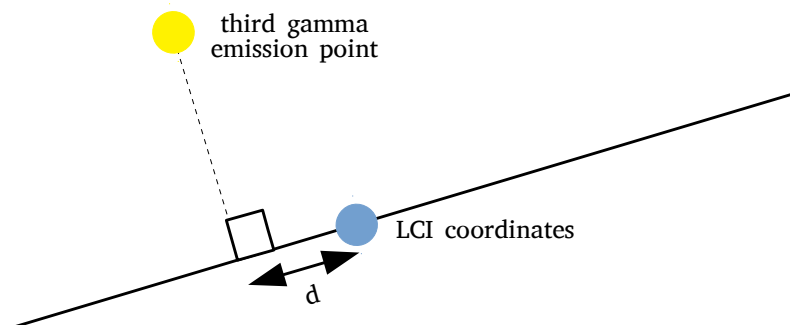


FIGURE 6: Étude sur d , la distance entre la projection du point d'émission du troisième gamma sur la LOR et les coordonnées LCI.

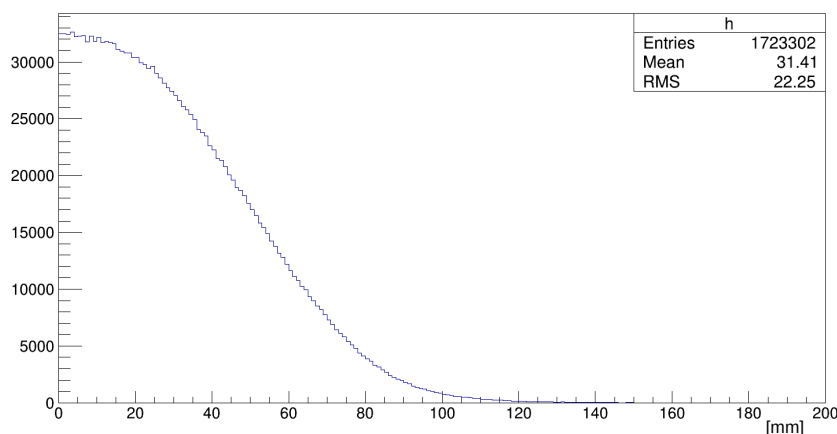


FIGURE 7: Incertitude sur la position du LCI.

voir Fig.8 et Table 1 pour plus de détails.

L'activité totale simulée dans le fantôme est de 20 kBq, avec un facteur 15 de rapport de contraste entre la sphère et l'arrière-plan. 30 doublons ont été simulés pour étudier la variance de l'image.

Pour compléter la caractérisation, en tant que deuxième fantôme, nous avons choisi de simuler un objet plus réaliste: une souris mâle de 28 g (fantôme Digimouse). Le petit animal présente une structure complète, composée du cerveau, des muscles, des yeux, des glandes, du cœur, des poumons, du foie, de l'estomac, de la rate, du pancréas, des reins, des testicules, de la vessie, du squelette et de la peau. Une tumeur sphérique de rayon de 2 mm a été ajoutée dans le cerveau en tant que ROI à analyser pour l'étude de qualité d'image. Le figure 9 montre une vue transaxiale de la tranche centrale de Digimouse et le tableau 2 la distribution simulée d'absorption de la souris.

Le radiopharmaceutique utilisé dans cette simulation est le $[^{44}\text{Sc}]\text{Sc-J591}$

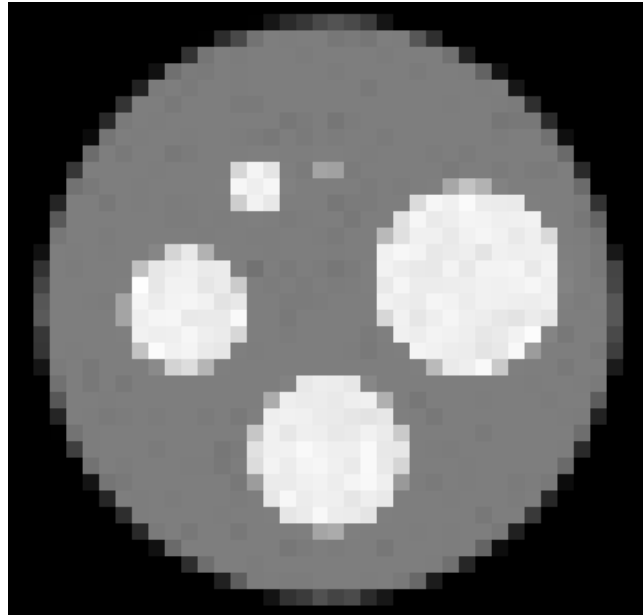


FIGURE 8: Coupe axiale du fantôme type NEMA.

Radius [mm]	Position (X,Y,Z) [mm]
2	(0.0, 17.5, 0.0)
4	(-8.8, 15.1, 0.0)
8	(-17.5, 0.0, 0.0)
10	(0.0, -17.5, 0.0)
12	(17.2, 3.7, 0.0)

TABLE 1: Dimensions et positions des cinq sphères dans le fantôme.

marqué au Sc-44, un anticorps recombinant monoclonal marqueur de l'antigène PSMA spécifique de la membrane prostatique l'absorption biologique est connue de Carter [2] et des études de Holland [3]. Un des avantages de l'utilisation du $[^{44}\text{Sc}]\text{Sc-J591}$ est que la molécule est également utilisée pour les études de parcours du positon puisqu'elle est facilement associée aussi au F-18.

L'activité totale simulée dans le fantôme était d'environ 22 kBq et le temps d'acquisition des données était de 20 minutes. En raison de la structure plus détaillée du fantôme Digimouse, un temps de calcul plus long a été nécessaire et une seule acquisition a été simulée.

Toutes les images que nous avons reconstruites dans ce travail sont obtenues grâce à l'algorithme de reconstruction LM-MLEM dans CASTOR v2.3, pour le pseudo-TOF et le non-TOF, que nous appelons respectivement 3- γ et 2- γ .

Comme pour tous les algorithmes d'optimisation itérative comme MLEM, la reconstruction dans CASTOR est basée sur un projecteur gérant à la fois la

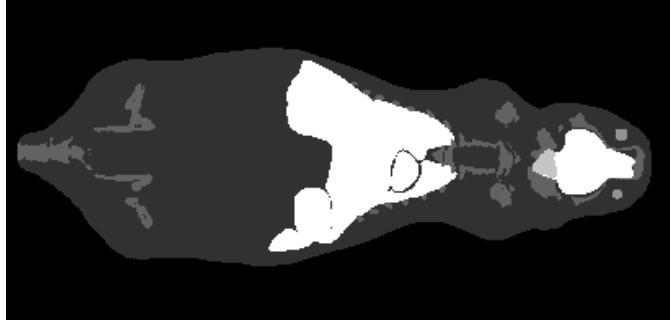


FIGURE 9: Coupe axiale du Digimouse avec les structures internes.

Organ	activity/voxel [Bq/0.5 mm ³]	Organ	activity/voxel [Bq/0.5 mm ³]
Skin	0.1	Testes	0.1
Spinebone	1.7	Stomach	0.1
Eye	0.1	Spleen	3.2
Brain	0.1	Pancreas	0.1
Muscle	0.1	Liver	1.5
Bladder	2.25	Kidney	0.7
Lung	0.1	Tumor (brain)	2.25

TABLE 2: Biodistribution du [⁴⁴Sc]Sc-J591 dans le corp du Digimouse.

projection arrière et avant et il y a un optimiseur et un convolveur, au cas où tout type de convolution serait nécessaire (par exemple pour la correction du parcours du positon).

Dans CASTOR, le calcul des éléments de la matrice système suit le projecteur Siddon et la méthode dite *ray-tracer*, pour laquelle la probabilité dépend de la partie de LOR traversant chaque voxel. L'optimiseur standard utilisé pour les événements à deux gamma est de Shepp et Vardi; tandis que pour l'algorithme LM-MLEM/TOF nous nous référons à Filipovic.

L'algorithme LM-MLEM pseudo-TOF peut être exprimé comme suit:

$$\lambda_j^{(k+1)} = \frac{\lambda_j^{(k)}}{\sum_{i,b} p_{i,j,b}} \sum_i \frac{p_{i,j,b}}{\sum_{j'} p_{i,j',b} \lambda_{j'}^{(k)}}. \quad (1)$$

où i fait référence au bin de la LOR et b au bin pseudo-temporel correspondant à l'événement considéré; $\lambda_j^{(k)}$ est la valeur de l'image dans le voxel j pour l'estimation k -th. On désigne comme pseudo-time-bin le bin du temps correspondant à l'équivalent en ps de la position LCI.

Nous montrons des résultats liés au fantôme de type NEMA obtenu par reconstruction de 3- γ et 2- γ MLEM. Pour la reconstruction pseudo-TOF, nous avons utilisé deux approches pseudo-TOF différentes: dans une reconstruction nous avons utilisé un écart-type gaussien fixe de 70 ps, qui est la valeur correspondant à l'incertitude moyenne sur le calcul LCI. Dans la seconde approche, la résolution était basée sur les événements, donc variable, calculée pour chaque événement comme l'équivalent en temps de la différence entre le LCI et la projection du point d'annihilation sur la LOR, comme le montre la Fig. 7.

La raison de montrer les résultats avec la résolution pseudo-temporelle moyenne et avec la résolution variable est d'étudier les bénéfices potentiels de l'approche proposée dans des scénarios favorables et moins favorables de précision du cône reconstruit.

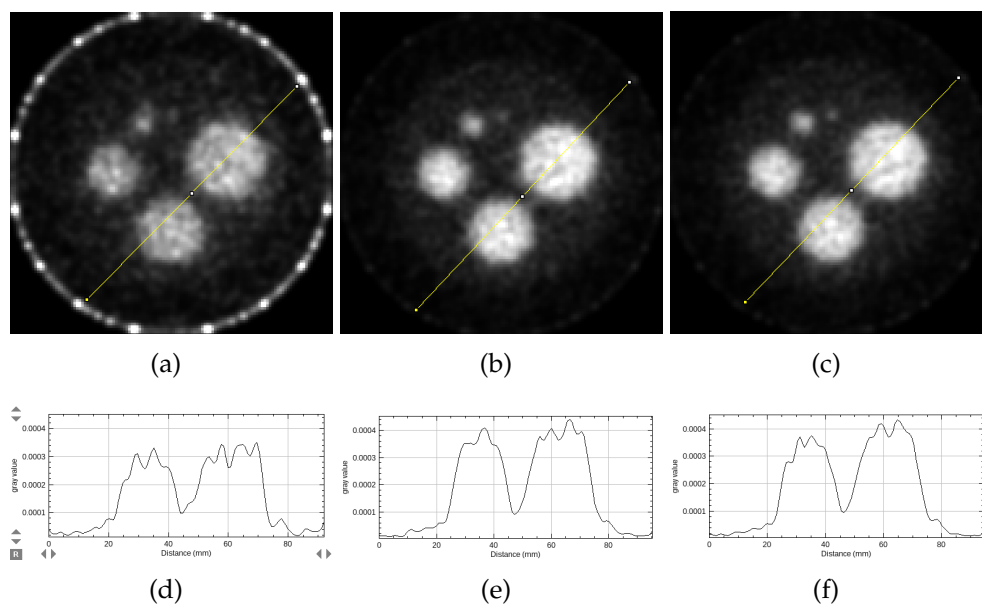


FIGURE 10: Coupe axiale du fantôme type NEMA après avoir appliqué un filtre gaussien ($\sigma = 1$ mm). Images reconstruite utilisant (a) reconstruction TEP classique, et la technique proposée dans ce travail (3- γ) avec (b) 70-ps et (c) un écart type variable événement par événement. Les images sont les résultats à la 30th itération. (d), (e) et (f) montrent les profils sur la ligne jaune.

La première différence entre l'étude de type NEMA et celle de Digimouse est que, dans le second cas, les images n'ont été obtenues que par reconstruction classique 2- γ et reconstruction pseudo-TOF avec plusieurs valeurs de résolution (70 ps, 100 ps, 150 ps et 200 ps). De plus, dans ce cas, les événements avec et sans point LCI ont tous deux été utilisés pour la reconstruction

d'image, en raison de la faible quantité d'événements 3- γ dans l'acquisition.

Les images reconstruites sont montrées sur la Fig. 11: on voit la tranche centrale du Dimouse sur le 30th itération pour 2- γ et pour tous les valeurs de résolution pseudo-TOF. De gauche à droite: reconstruction 2- γ , pseudo-TOF avec une résolution de 200 ps, 150 ps, 100 ps et 70 ps. Nous avons également calculé le profil le long de la ROI dans le cerveau du Digimouse, qui peut être vu sur la Fig. 12 pour toutes les différentes reconstructions.

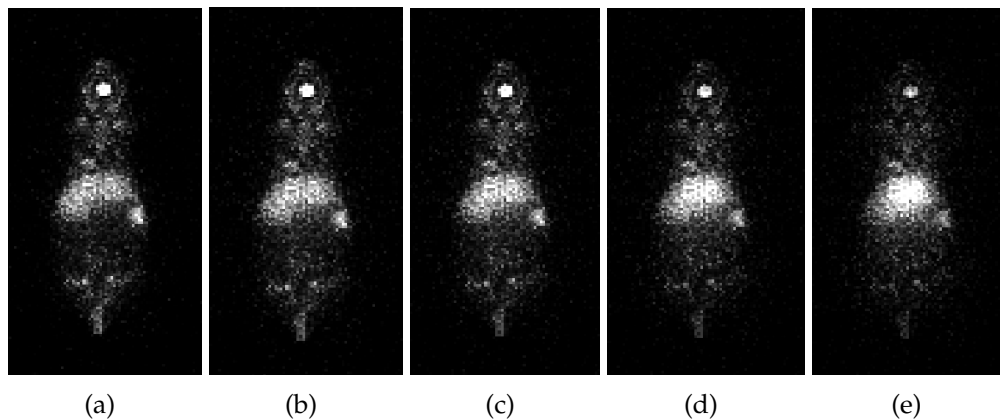


FIGURE 11: Images reconstruites du Digimouse: reconstruction 2- γ , reconstruction pseudo-TOF avec un écart type de 200 ps, 150 ps, 100 ps, et 70 ps.

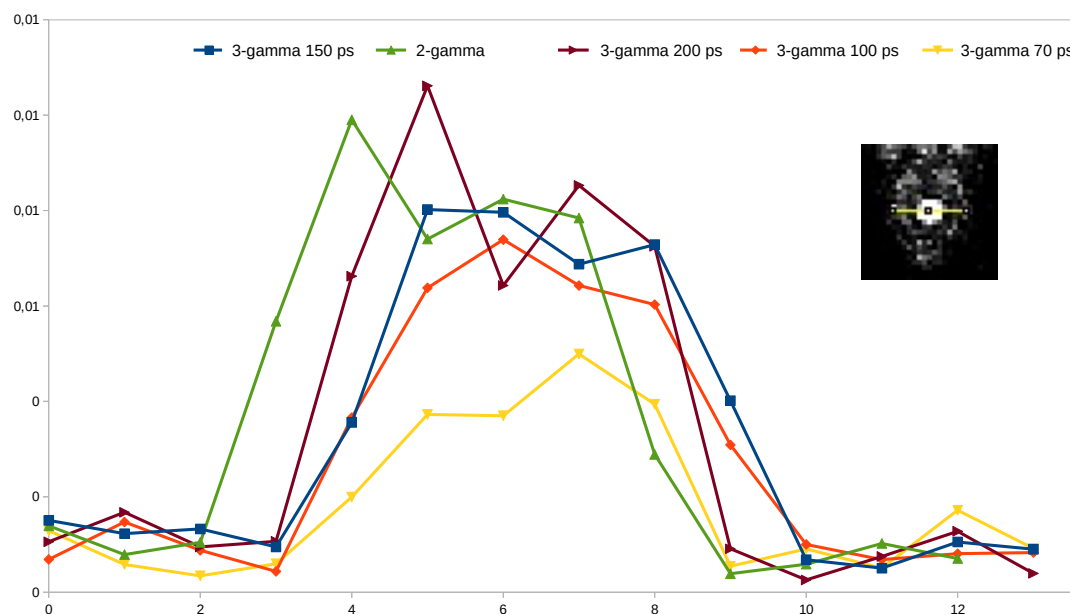


FIGURE 12: Profil sur la ligne qui croise la ROI dans le cerveau du Digimouse.

Pour le projet XEMIS2, l'intérêt de la correction du parcours du positrons concerne l'utilisation du Sc-44 comme radio-isotope a trois gammas, dont

le parcours de positrons n'est pas négligeable. Nous discutons des deux approches implémentées dans CASTOR pour corriger l'effet: d'abord par une approche a noyau invariant et ensuite par un a noyau variant basé sur le matériau. La carte des matériaux a été obtenue à partir du fichier du fantôme GATE.

Le fantôme choisi pour cette étude est composé d'un cylindre de 12 cm de long avec un rayon de 3,5 cm positionné au centre du FOV, dans lequel nous trouvons cinq sphères, voir Fig. 13 et Table 3. Les matériaux choisis sont l'eau, le poumon et l'os, pour explorer trois milieux de densités très différentes ($1,00 \text{ g/cm}^3$ eau, $0,26 \text{ g/cm}^3$ poumon et $1,42 \text{ g/cm}^3$ os).

Les données sont simulées dans GATE v6 en utilisant le modèle Penelope pour les interactions. L'activité totale simulée est de 20 kBq pour un temps d'acquisition des données de 20 minutes, avec un facteur 15 de contraste entre les points chauds et le fond.

Sphere nb	Position [mm]	Radius [mm]	Material	Density [g/cm^3]
1	(0.0, 17.5, 0.0)	2	water	1.00
2	(-8.8, 15.1, 0.0)	4	water	1.00
3	(-17.5, 0.0, 0.0)	8	water	1.00
4	(0.0, -17.5, 0.0)	10	lung	0.26
5	(17.2, 3.7, 0.0)	12	bone	1.42

TABLE 3: Description des sphères a l'intérieur du fantôme.

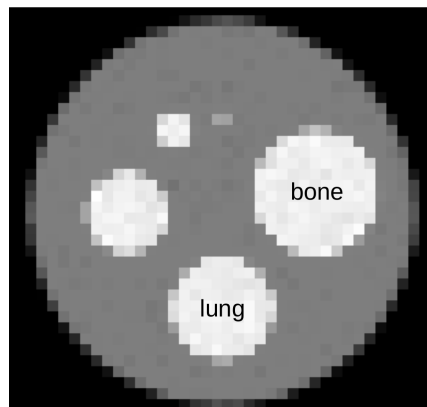


FIGURE 13: Coupe axiale du fantôme pour l'étude sur la correction de range du positon.

La reconstruction a été effectuée dans CASTOR en utilisant un algorithme LM-MLEM dans lequel nous avons implémenté la correction de le parcours du positon par convolution. Nous montrons les résultats obtenus avec la

reconstruction conventionnelle 2- γ et 3- γ pour pouvoir comparer les deux approches, avec et sans correction du range de positons. En particulier, pour un noyau stationnaire, la convolution est déjà implémentée dans le logiciel, avec des choix multiples au moment de l'appliquer: sur l'image à projeter en avant, sur les termes de correction de la rétroprojection, sur l'image reconstruite, ou sur l'image estimée.

Dans nos techniques de correction implémentées avec un noyau variant, nous avons choisi d'appliquer une convolution isotrope sur l'image à projeter en avant à chaque itération. L'algorithme développé accepte 4 noyaux différents, pour les 4 matériaux du fantôme, et pour chacun d'eux, on peut spécifier le nombre de sigmas gaussiens à utiliser et le FWHM (axial et transaxial).

Les valeurs des FWHM de noyaux ont été calculées à partir d'une simulation de 20 minutes de trois sources ponctuelles, une de chaque matériau, avec 1000 Bq d'activité initiale dans chacune d'elles. Afin d'associer le bon noyau à chaque voxel, l'algorithme de convolution prend en entrée une label image avec des nombres de 0 à 3, chacun d'eux correspondant à un noyau différent à utiliser lors de la convolution. Dans notre cas, la label image a été directement obtenue à partir du fantôme GATE et basée sur les matériaux simulés.

Nous avons reconstruit des images via une reconstruction classique TEP et via une reconstruction pseudo-TOF, en utilisant une résolution de 70 ps. Dans les deux algorithmes, nous avons ajouté la correction du parcours de positrons par convolution de noyau variant et invariant.

Pour le cas a noyau invariant, nous avons effectuée une convolution avec un FWHM de 2,0 mm. Pour le cas a noyau variant, la sphère de 10 mm de rayon et la sphère de 12 mm de rayon ont été associées aux valeurs correspondantes calculées par l'étude précédent et le reste de l'image a été convolué avec une FWHM égal à 1,9 mm, considérant que nous sommes en présence d'eau et d'air.

Outre à l'amélioration du contraste due à l'utilisation de 3- γ au lieu de la reconstruction TEP classique, le contraste général des cinq sphères est amélioré dans les images corrigées, en particulier pour pseudo-TOF dans Fig. 14 (d) et (f), respectivement la convolution a noyau variant et invariante. L'amélioration est correctement quantifiée sur la Fig. 15, où nous montrons le profil le long des lignes jaunes pour les six reconstructions. Entre les profils des reconstructions 2- γ et ceux liés au 3- γ , nous avons un écart de 20% sur

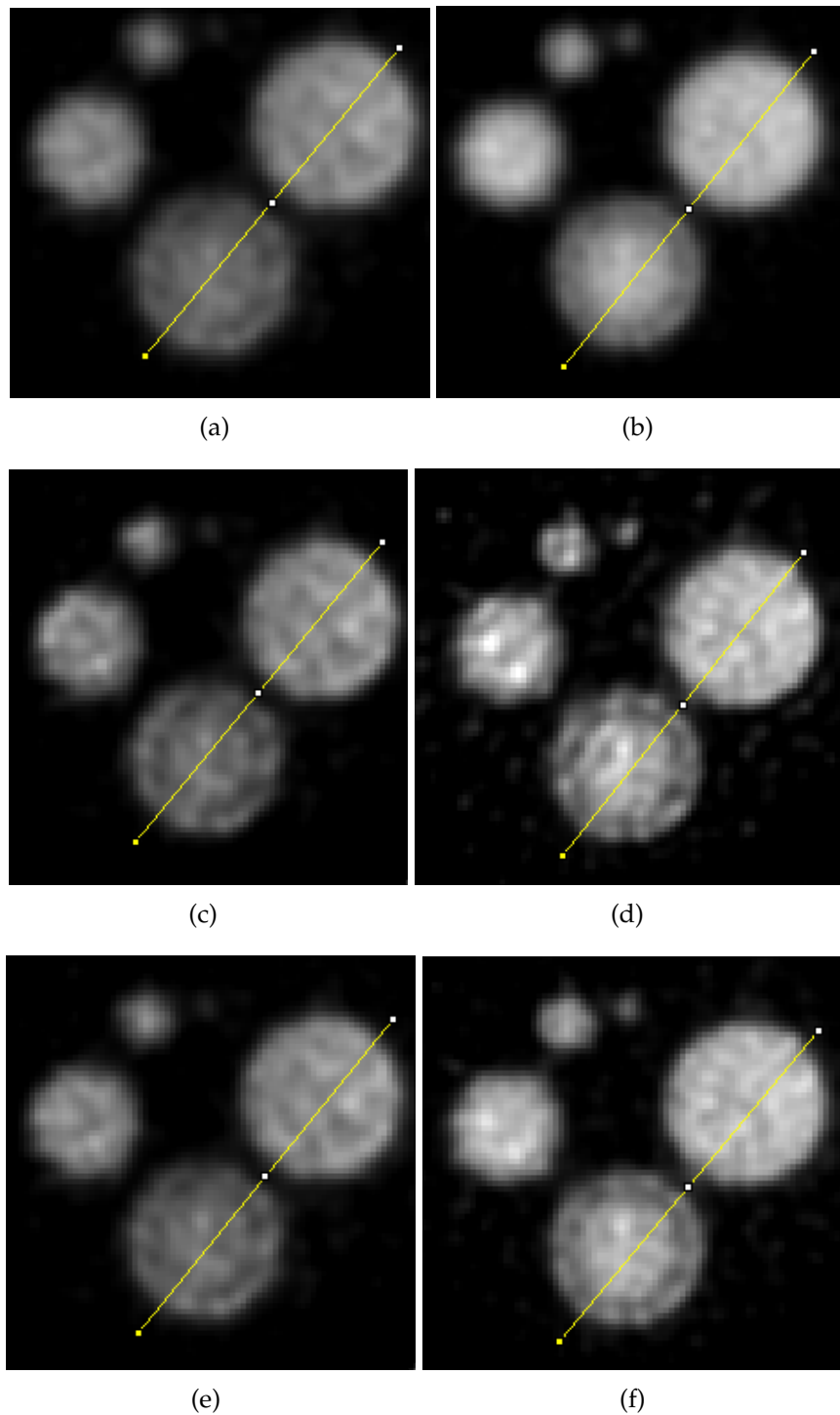


FIGURE 14: Coupe transversale du fantome. Images reconstruites avec differentes techniques: (a) TEP classique et (b) 3- γ , pas corrige; (c) 2- γ et (d) 3- γ convolues avec des noyaux variantes, (e) 2- γ et (f) 3- γ convolues avec un noyau stationnaire.

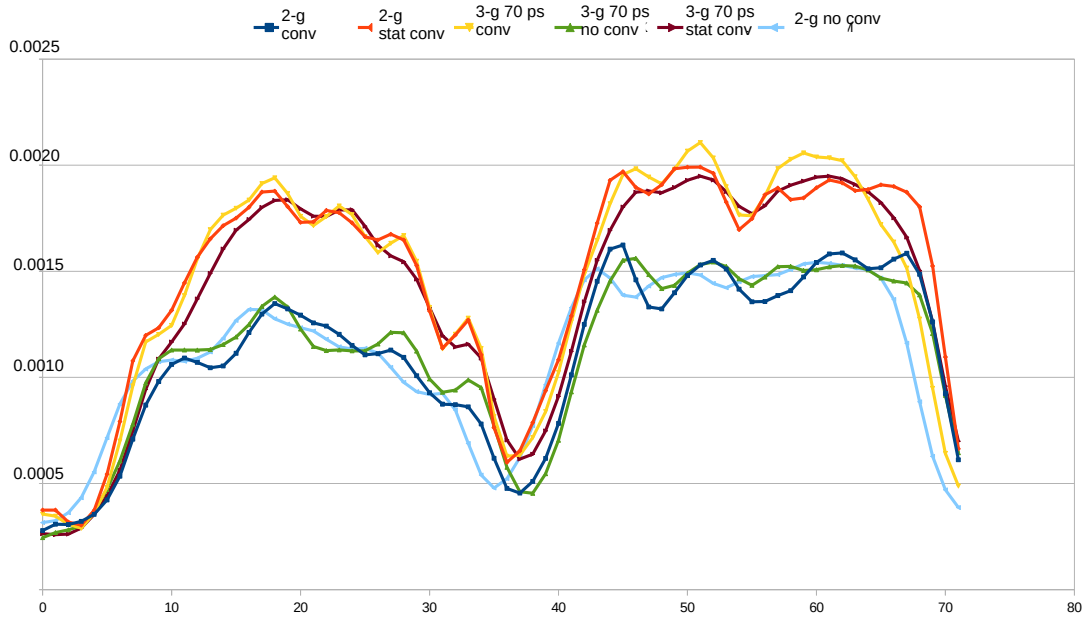


FIGURE 15: Profile sur la ligne jaune.

l'échelle de gris, alors qu'il n'y a pas de différence remarquable entre les images corrigées et non corrigées pour les mêmes technique de reconstruction d'image.

Les travaux présentés dans cette thèse ont porté sur le développement d'une nouvelle technique de reconstruction pour l'imagerie 3-gammas, qui a été évaluée sur la géométrie du système d'imagerie XEMIS2. L'étude XEMIS2 est la partie préclinique du projet plus général XEMIS, qui a déjà développé un premier prototype, le XEMIS1. La caractérisation de la caméra Compton XEMIS1 a donné la démonstration expérimentale de la faisabilité de l'imagerie trois gammas, on retrouve les études précédentes dans Gallego-Manzano [4], Oger [5] et Grignon [6].

Dans ce travail, nous utilisons les interactions du troisième-gamma dans le LXe pour déterminer un cône Compton, dont le point d'intersection avec le LOR, obtenu à partir des photons de coïncidence, permet de restreindre la localisation des LOR section impliquée dans l'événement combiné *annihilation + émission*. L'événement est ensuite reconstruit à l'aide d'un pseudo-TOF/MLEM algorithme où l'intersection ligne-cône est prise comme centre d'un PDF gaussien utilisé dans la reconstruction, de la même manière que dans TOF-PET, d'où la dénomination de la méthode proposée comme pseudo-TOF. Un avantage principal associé à l'approche proposée est de permettre l'intégration de l'information du troisième gamma dans des cadres de reconstruction existants avec une capacité TOF, tels que CASTOR.

Nous avons montré une étude basée sur la simulation d'une acquisition de données de 20 minutes avec 20 kBq de radioactivité initiale dans le détecteur XEMIS2. Nous avons simulé un fantôme de type NEMA et Digimouse et montré une amélioration de la qualité d'image pour des objets de différentes densités et dimensions. Nous avons présenté le calcul des coordonnées LCI, sur lequel nous basons la méthode de reconstruction d'image 3- γ . Nous avons discuté des caractéristiques obligatoires du détecteur en termes de résolution spatiale, énergétique et angulaire pour réduire l'incertitude sur le point LCI.

Le calcul des coordonnées LCI est une étape cruciale vers l'application de l'approche proposée dans un contexte clinique réel. Pour cela, il faut être capable de déterminer avec suffisamment de précision la localisation de trois clusters d'interaction dans LXe: les deux clusters correspondant aux photons d'annihilation et celui correspondant au troisième gamma.

Les principaux défis liés à la détection de trois événements gamma dans des données réelles concernent le clustering des groupes d'interactions, ainsi que la détermination de l'angle de Compton et des deux premiers points d'interactions pour le troisième gamma utilisé pour déterminer le cône.

Introduction

Clinical nuclear medicine can be considered to have started as early as 1927 when Blumgart and Weiss [7] analyzed the normal and abnormal circulation of blood in patients using the radioisotope Bi^{214} . The first medical detectors were mainly borrowed from experimental and nuclear physics, made of scintillators coupled to photomultipliers (PMTs) through a light guide to read the signal. In the 1970s computed tomography (CT) scanning systems were invented in conjunction with tomographic reconstruction. In the same years magnetic resonance imaging (MRI) was developed, and later on positron emission tomography (PET) and single photon emission tomography (SPECT) imaging systems [8].

Nowadays, nuclear medicine allows for the study of *in vivo* biological and metabolic processes in the body using mainly two functional molecular imaging modalities: SPECT and PET imaging. Both imaging modalities are based on the use of radiopharmaceuticals (or radiotracer), whose biodistribution in the body can be evaluated using external detection and tomographic reconstruction. The radiotracer is composed of a substance that follows a physiological process labeled with a radioactive isotope that emits radiation detectable from outside the body. For SPECT diagnostics the radiopharmaceutical is a single photon emitter, detected through a gamma camera rotating around the patient, while in PET studies positron emitters are employed and the detection occurs in a ring-shaped detector surrounding the body.

While nuclear imaging allows for improved screening, diagnosis and follow-up of several diseases, it also introduces some risks related to radiation exposure [9]. Nowadays the two main factors that guide research and development in nuclear imaging are arguably the reduction of the administered dose and of the acquisition time, for both safety and practical purposes. These two factors have a critical influence on image quality as the signal to noise ratio (SNR) is mostly dependent on the number of photon counts in the detectors [10, 11, 12]. To maintain sufficient image quality standards required in modern medicine while decreasing the total activity, image processing and

software-based methods have been implemented [13, 14], together with the use of new imaging systems [15, 16, 17]

New systems, known as time of flight (TOF)-PET, were first conceived in the 1970s. Their goal is to measure the time difference between the two coincidence photons' arrival in opposite detectors to estimate the position along the line of response (LOR) where the annihilation took place. The localization uncertainty is determined by the time resolution of the detector, which can be characterized by the full width half maximum (FWHM) of the distribution centered in $x = c \cdot \Delta t$, where c is the speed of light and Δt the time difference. Using an ideal detector with infinitely accurate time resolution, one could exactly locate the annihilation position and therefore have direct access to the radiotracer biodistribution. However, due to the limitations of current instrumentation techniques, tomographic techniques are still required.

Algorithms used to reconstruct tomographic images can be classified into two main groups: analytical and iterative methods. In the first case, we deal with an inversion problem between a function and its line integral. In the second case we model all the possible aspects of data acquisition and all the physical interactions that can occur and we look for the image that best fits the data in an iterative fashion. The data on which we base our reconstruction are acquired detecting 511-keV coincidence photons in PET and single photons in SPECT. In both cases, the limited amount of events and the particle stochastic behavior result in noisy outputs. Historically, the rationale for changing from analytical to iterative image reconstruction was related to better noise-modeling of the latest iterative algorithms. Shepp and Vardi [18] were the first to propose an maximum likelihood expectation maximization (MLEM) method that showed significant improvement over the previous analytical filtered backprojection (FBP). Today the most used image reconstruction algorithm is based on their first model and its variations (list mode (LM)-MLEM, ordered subset expectation maximization (OSEM)).

In this thesis we present three-gamma ($3\text{-}\gamma$) imaging, where the acquisition system relies on a β^+ and γ emitter. The reasoning behind $3\text{-}\gamma$ imaging is that the third gamma detection information may help to provide better localization of the annihilation point, thus enabling higher image quality of reduced dose delivered to the patient. Detectors taking advantage of a third gamma emission have been proposed in a number of studies [19, 20, 21, 22], [23, 24]. Among these efforts, in this work we present the xenon medical imaging

system 2 (XEMIS2) camera, a preclinical 3- γ imaging scanner developed in Nantes, France. Two main characteristics of XEMIS2 make it suitable for 3- γ imaging: the use of liquid xenon (LXe) as scintillation medium, that offers a continuous geometry, and the use of Scandium-44 (Sc-44), a $\beta^+ - \gamma$ emitter, which enables the 3- γ detection.

The aim of this work is to present a new image reconstruction method based on 3- γ detection, which could allow better image quality and thus a reduction of the administered dose. The principle on which 3- γ image reconstruction is based is the intersection between a LOR and a Compton cone belonging to the same event. From the two coincidence photons we obtain a LOR, while from the third gamma, emitted as a prompt gamma, we determine a cone. The intersection between the LOR and the cone provides the LOR/cone intersection (LCI) coordinates that locate the most probable annihilation position on the LOR, as for the time difference in TOF, whence the pseudo-TOF denomination of the proposed reconstruction method. In this case, we proposed to carry on a study on the distribution sigma, which depends not only on the scanner resolution but on multiple factors (positron range, energy resolution, scattering, etc).

This work is composed of five main chapters in addition to general introduction and conclusion. In Chapter 1 we introduce nuclear imaging, starting with the physics behind nuclear medicine: positron decay, positron-electron annihilation and other positron interactions with matter, positron range, photon attenuation and interactions. The second part of the chapter is about PET imaging, we illustrate how the coincidence photons are detected, we present the challenges concerning scattering and random coincidences, and also the sensitivity and the depth of interaction (DOI) problem in PET. In Chapter 2 we introduce Image Reconstruction in a historical way: first, discussing data acquisition and then talking about analytical image reconstruction algorithms and model-based ones. At the end of the chapter we present the system matrix and all the effects that can be included in the modelization, as the detector geometry, the attenuation, the normalization, the scattering, and the positron range. In Chapter 3 we present the proposed 3- γ reconstruction method. We begin addressing our attention to the XEMIS2 project, we discuss the detector and its geometry, the used radioisotope, the data acquisition, and detection process. Then we expose the proposed image reconstruction technique, based

on 3- γ detection, including the LCI computation, and all the needed requirements as a matter of spatial and energy resolution and, even more important, as angular resolution. The second part of the chapter deals with the Geant4 Application for Emission Tomography (GATE) Monte Carlo simulation used to obtain data. We show the simulated phantoms and talk about customizable and advanced software for tomographic reconstruction (CASToR), the reconstruction software, in which we implemented the 3- γ reconstruction algorithm. In Chapter 4 we show the results obtained from the simulation, and the image analysis that was carried on. First, we present the figures of merit used in the analysis, and then the results: the reconstructed image using 3- γ and conventional PET method and some metrics and profile plots. In Chapter 5 we discuss the positron range correction issue related to the use of Sc-44. We talk about the state-of-the-art techniques to correct the effect and we show what has been done in our case using variant and invariant kernel convolution, implemented directly in CASToR reconstruction software. At the end of this work, in the conclusion 5.6, we discuss all that has already been done for 3- γ image reconstruction and possible future developments among which is the use of Neural Networks to correctly compute the LCI point.

Notation: vectors will be denoted by bold italic letters (e.g. \mathbf{v}), matrices will be written in upper-case bold italic letters (e.g. \mathbf{A}), with a_{ij} being the entry at row i , column j .

Chapter 1

General principles of nuclear imaging

Summary

In this chapter, we introduce the main subject of this work and we gather all the necessary information to fully understand the 3- γ image reconstruction method, starting with the introduction to PET imaging. We first present the physics of PET, the radioactive β^+ decay and the interaction of particles with matter, in particular positron and photon's interaction at low energies. We then introduce the basics of PET imaging, as a matter of detection, coincidence discrimination, and all the challenges encountered with detector sensitivity and DOI. At the end of the chapter we mention TOF-PET introducing briefly the theory and the basic notions that will be helpful in the following of this work.

Contents

1.1 Introduction	24
1.2 Physical principles	24
1.2.1 Radioactive decay	24
1.2.2 Charged particle's energy loss	26
1.2.3 Positron range	27
1.2.4 Photon interactions with matter	28
1.2.5 Photon attenuation	32
1.3 PET imaging	33
1.3.1 Detection	34

1.3.2	Coincidences	36
1.3.3	Sensitivity and Depth Of Interaction	37
1.3.4	Time of Flight PET	38

1.1 Introduction

Nuclear imaging is based on the use of radioactive compounds, composed of a molecule labeled with a radioisotope, that follow physiologic or pathological processes linked to a variety of diseases. There exist more than 100 different types of diagnostic exams for nuclear medicine, that can detect early stages of oncological or neurological diseases, when cures are more effective. Unlike other medical imaging procedures, which map the anatomy of the body with almost no information about the metabolism, nuclear imaging, and in particular PET imaging, is a valuable mean for providing disease-related quantitative and qualitative information.

1.2 Physical principles

In this section, we discuss some of the basic principles of nuclear physics, especially the ones in which we are most interested, as radioactive decay and photon and positron's interactions with matter.

1.2.1 Radioactive decay

There exist six different modes of radioactive decay [25], but the only one interesting in PET imaging is positron decay, also called β^+ decay. More generally, in PET, radiotracers are labeled with positron emitters (see Table 1.2) that are unstable elements decaying through β^+ emission. Positron decay consists of the conversion of a proton into a neutron with the emission of a positron and a neutrino, according to the following expression:



where the * indicates that the proton is not a free particle but belongs to a nucleus.

And furthermore through this equation involving the parent and daughter nuclide:



A minimum transition energy requirement is expected for β^+ decay, since the nucleus reduces its atomic number by one and after losing a positron, the daughter-atom loses an electron to reach its ground state. The mass of both electron and positron being respectively particle and anti-particle, is 511 keV, from which the total minimum of 1.022-MeV energy is required [26].

As the positron travels in the surrounding tissue, it loses its kinetic energy in Coulomb interactions with the atomic electrons. As the rest mass approaches the electron mass, the trajectory deviation may be accentuated, giving an intricate and twisted path to the particle. When the positron reaches thermal energy (few keV), it interacts with an electron by annihilation or forming a *positronium* atom with a lifetime of about 0.12 ns [27]. Two forms are possible in its ground state: ortho-positronium (parallel particles' spins) or para-positronium (anti-parallel particles' spins), the latter decays in self-annihilation producing two 511-keV photons as for positron-electron annihilation, while the former annihilates producing three gammas. The back-to-back emission of free annihilation is required for the momentum conservation in the electron-positron pair. Since the photons emission takes place in a frame of reference that moves with a different velocity than the one of the detection system, the photons can be emitted in a slightly different direction from the ideal 180° by a few tenths of degree ($\sigma \approx 0,5^\circ$) [28].

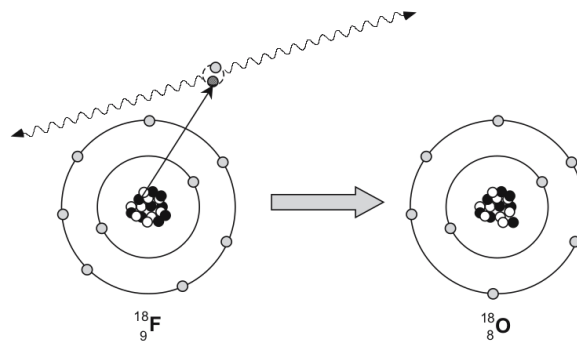


FIGURE 1.1: Positron emission and annihilation scheme for F-18 [29].

Mathematics of radioactive decay

Nuclear radioactive decay obeys the following equation:

$$\frac{dN}{dt} = -\lambda N(t). \quad (1.3)$$

in which dN is the number of nuclei decaying in a very short amount of time dt , λ is the decay constant, and $N(t)$ the number of nuclei at time t . The decay constant does not depend on external factors, but only on the effective decay of the nuclei and it is not tabulated. Instead, we refer to the half-life, defined as the amount of time it takes to reduce the original activity by a factor two:

$$T_{1/2} = \frac{\ln(2)}{\lambda}. \quad (1.4)$$

1.2.2 Charged particle's energy loss

A charged particle of mass M_1 and charge Z_1 penetrating a material of atomic number Z_2 and atomic mass M_2 , slows down losing energy to the medium's atoms. It interacts with the matter via electromagnetic force with the electrons and protons and via strong nuclear force with the nuclei. The particle's stopping process involves complex interactions, although we can measure the particle's average energy loss per unit pass length, called *stopping power*, $\frac{dE}{dx}$ [30]. The computation of this quantity requires a complete knowledge about the particle energy loss mechanisms and it changes drastically from particle to particle. In particular between ions and electrons/positrons, due to the difference in mass.

In this work, we are mostly interested in the energy loss of the positron, which is mainly caused by two mechanisms: Coulomb interaction with orbital electrons of the nuclei or *collision stopping power (CSP)* and Bremsstrahlung emission or *radiation stopping power (RSP)* [31]:

$$\left(\frac{dE}{dx}\right)_{\text{tot}} = \left(\frac{dE}{dx}\right)_{\text{c}} + \left(\frac{dE}{dx}\right)_{\text{r}}. \quad (1.5)$$

The first term is the CSP and the second term is the RSP. CSP was firstly studied by Bethe and Bloch [32] and later on by Bhabha [33], which formalized

it as follows:

$$\left(\frac{dE}{dx}\right)_c = \frac{KZ}{2A\beta^2} \left(\left(\frac{m_e c^2 \beta^2 \gamma^2 (m_e c^2 \frac{\gamma-1}{2})}{I^2} \right) + 2 \ln 2 - \frac{\beta^2}{12} \left(23 + \frac{14}{\gamma+1} + \frac{10}{(\gamma+1)^2} + \frac{4}{(\gamma+1)^3} \right) - \delta \right). \quad (1.6)$$

where m_e is the electron/positron mass, $\beta = \frac{v}{c}$, with v the particle velocity and c the speed of light; $\gamma = \frac{1}{\sqrt{1-\beta^2}}$ is the Lorentz factor. The variable I represent the mean excitation energy, Z the atomic number, A the atomic mass of the material, $K = \frac{4\pi e^4 N_0}{m_e c^2} = 0.307075$ is a coefficient, being N_0 the Avogadro number and e the electron charge, and δ is the density correction effect.

On the other hand, the RSP was studied by Lindhard and Ritchie [34, 35]. In the positron case, due to the small mass, the particle deviates from its trajectory when in the nucleus' electric field, with a radial acceleration causing the Bremsstrahlung emission. When the particle reaches the *critical energy*, that is when the radiative energy loss equals the collision energy loss, the Bremsstrahlung becomes dominant. The computation of the energy loss due to radiation emission is rather complex and we define it through a parameter, called *radiation length* X_0 , that corresponds to the distance over which the positron energy is reduced by $\frac{1}{e}$ due to radiative loss only [36]:

$$\left(\frac{dE}{dx}\right)_r = \frac{E}{X_0}. \quad (1.7)$$

1.2.3 Positron range

A positron is emitted during nuclear decay with an energy that spans from 0 to the maximum available energy, following an asymmetrical distribution centered around half of the E_{\max} . In Table 1.1 we see some reference values for the most common PET radionuclides. Due to its initial kinetic energy, the positron path can be not negligible for high energy positrons. The positron range depends also on the material in which it propagates since the interactions probability is calculated on the atomic number and atomic mass.

Positron range is one of the main sources of blur in PET imaging: for F-18, the most used PET radionuclide, we deal with 0.5-mm range correction in the human body, while for Sc-44, the radioisotope chosen for the image reconstruction method proposed in this work, the correction is around 2 mm [37].

We show in Fig. 1.2 a comparison between the energy spectra of the two isotopes. The energy distribution function used to obtain the histograms can be approximated following Levin and Hoffman's formula [38]:

$$N(E)dE = pF(Z - 1, E) \left(1 + \frac{E}{0.511}\right) (E_{\max} - E)^2 dE. \quad (1.8)$$

where Z is the atomic number of the nucleus that undergoes β^+ decay, E is to the kinetic energy of the positron in MeV, E_{\max} is the maximum kinetic energy in MeV, p is the momentum of the positron $p = \sqrt{\left(1 + \frac{E}{0.511}\right)^2 - 1}$ and $F(Z, E)$ is the Fermi function:

$$F(Z, E) = \frac{2\pi\eta}{1 - e^{-2\pi\eta}}. \quad (1.9)$$

in which $\eta = -\frac{Z\alpha}{p} \left(1 + \frac{E}{0.511}\right)$, $\alpha = \frac{1}{137}$ being the fine structure constant.

Due to the small correction, positron range for F-18 can be neglected for all those cases in which the scanner resolution is higher than the correction itself [39].

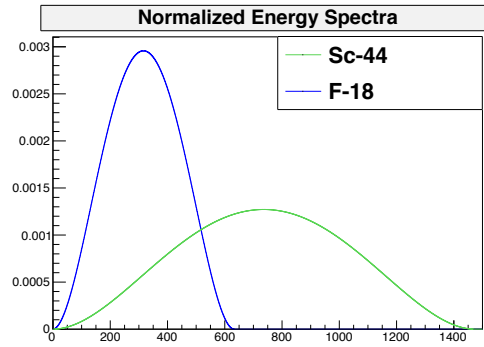
Isotope	Mean positron range [mm]	Isotope	Mean positron range [mm]
^{18}F	0.5	^{15}O	2.5
^{64}Cu	0.57	^{60}Cu	3.09
^{13}N	1.31	^{76}Br	3.09
^{61}Cu	1.32	^{62}Cu	4.39
^{44}Sc	2.4	^{66}Ga	6.13

TABLE 1.1: Mean positron range in water for isotopes of interest in PET [40, 41].

The blurring introduced in the reconstructed images by the positron range effect is due to the displacement of the LOR. In Fig. 1.3 we can see how the distance d influences the LOR positioning. This quantity is not directly proportional to the three-dimensional (3D) range of the positron, r . The distance d is computed as the projection of the positron range distribution on the LOR [42].

1.2.4 Photon interactions with matter

High-energy photons are secondary ionizing radiation, meaning that they interact with atoms, nuclei, and electrons without causing direct ionization.



(a)

FIGURE 1.2: Normalized energy spectra distributions for Sc-44 (green) and F-18 (blue).

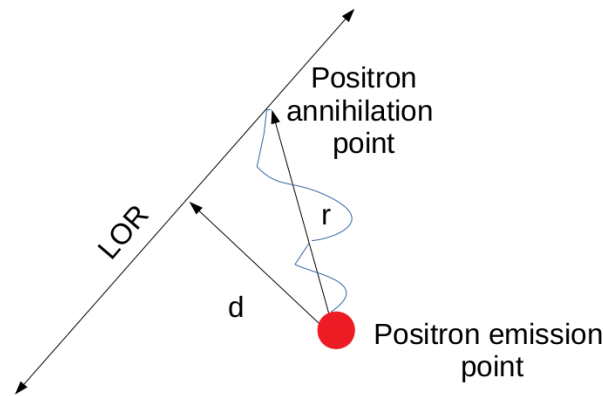


FIGURE 1.3: Scheme of positron decay: the range r is the distance from the annihilation point. The real effect is the LOR displacement, measured as the distance d between the annihilation point and the LOR.

The interaction can be seen as a collision, that results in the ejection of an electron, which can cause ionization. There are four significant photon-matter interactions in nuclear medicine: photoelectric effect, Compton scattering, pair production, and Rayleigh scattering.

The photoelectric effect consists of a collision between a photon and an atom. The incident photon is absorbed by the atom and all its energy is passed over to an orbital electron. If the transferred energy E_0 is higher than the binding energy E_b , this particle, also called *photoelectron*, can be ejected with an energy given by the following equation:

$$E_{pe} = E_0 - E_b. \quad (1.10)$$

this interaction can in turn create a vacancy in an orbital shell, which leads to

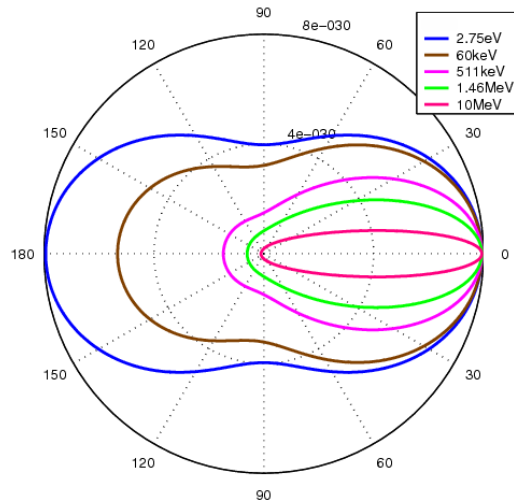


FIGURE 1.4: The Klein-Nishina distribution of Compton scattering angles over a various range of energies.

the emission of characteristic x-ray due to the downgrading of outer orbital electrons towards the vacancy.

When the collision occurs between a photon and an atomic external electron, we deal with Compton scattering. If the photon's deposited energy is higher than the electron's binding energy, then the electron is ejected as a recoil electron. In any case, the photon is only deflected, not absorbed, with an angle θ_C and an energy that is calculated as in the following equation:

$$E' = \frac{E_0}{1 + \left(\frac{E_0}{m_e c^2}\right) (1 - \cos\theta_C)}. \quad (1.11)$$

where E_0 is the incident photon's energy, m_e is the mass of the electron and c is the speed of light. Thus the Compton scattering angle can then be calculated as follows:

$$\cos\theta_C = 1 + m_e c^2 \left(\frac{1}{E_0} - \frac{1}{E'} \right). \quad (1.12)$$

The transferred energy range goes from 0 keV to a maximum value E_{\max} . The extreme cases occur when there is a back-scattering event, see Fig. 1.4. Compton scattering is not equally probable at all energies or for all scattering

angles, the interaction probability follows the Klein-Nishina's formula:

$$\frac{d\sigma}{d\Omega} = Zr_0^2 \left(\frac{1}{1 + (1 - \cos\theta_C)} \right)^2 \left(\frac{1 + \cos^2\theta_C}{2} \right) \left(1 + \frac{(1 - \cos\theta_C)^2}{(1 + \cos^2\theta_C)(1 + (1 - \cos\theta_C))} \right). \quad (1.13)$$

where $\frac{d\sigma}{d\Omega}$ is the differential cross-section, Z the atomic number of the material, r_0 the electron radius.

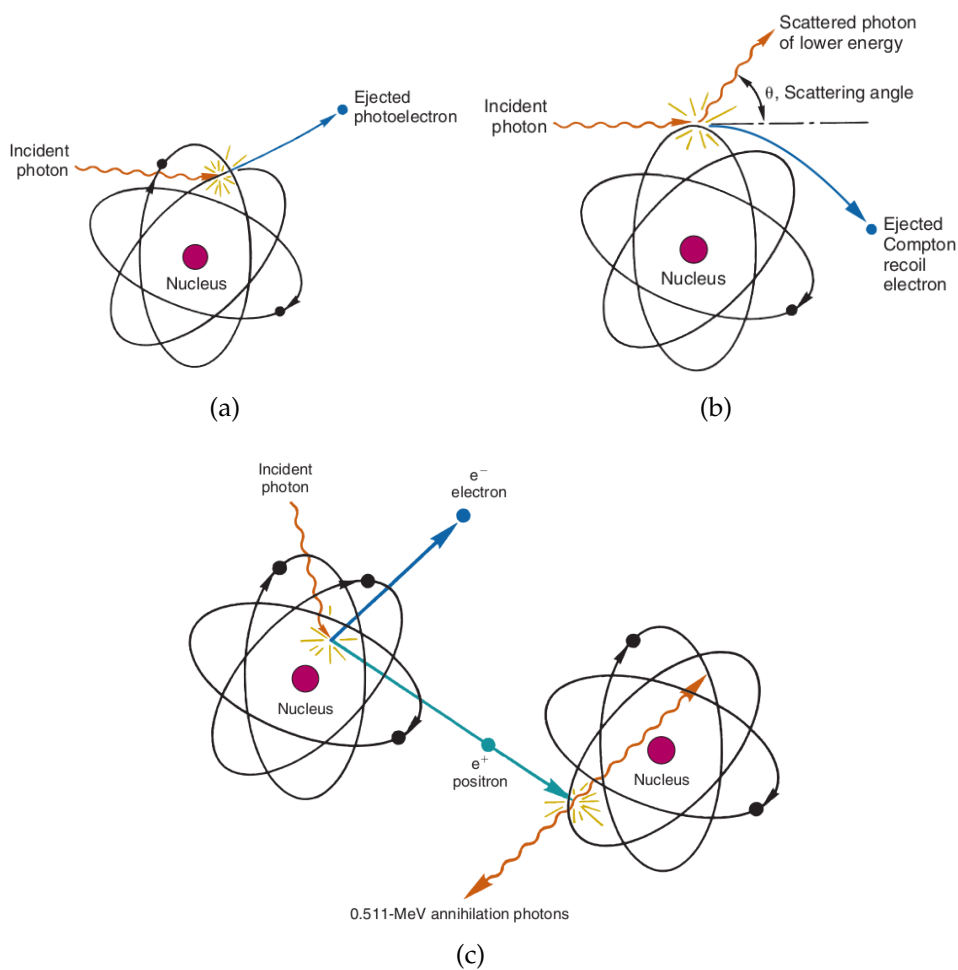


FIGURE 1.5: Photon interactions with matter: (a) photoelectric effect, (b) Compton scattering and (c) pair production [43].

For energies higher than 1.022 MeV we can deal with pair production. This consists of the interaction between a photon and a charged particle's electric field, in which the photon is converted into an electron-positron pair. The requirement of minimum energy is due to the sum of the electron and positron mass, which accounts for 1.022 MeV. The difference between the

incident photon's energy and the sum of the two masses is equally shared between the new particles pair as kinetic energy.

Another kind of scattering named coherent or Rayleigh scattering involves a photon and an atom: due to the great atomic mass almost no energy is absorbed in the collision as recoil energy, and the photon is scattered with very few energy loss.

These four main photon interactions do not occur at all energies and in all materials with the same probability. We can see in Fig. 1.6 how for lower energies in low Z materials the photoelectric effect is the most probable interaction, while for energies higher than 1.022 keV pair production is predominating. Compton scattering is most likely to happen for 511-keV photons in an organic body, however in case of small diffusion angles the two gammas can still be recorded as coincidence photons in PET. Scattered events represent between 40% and 60% of the total events in a scanner acquisition [44].

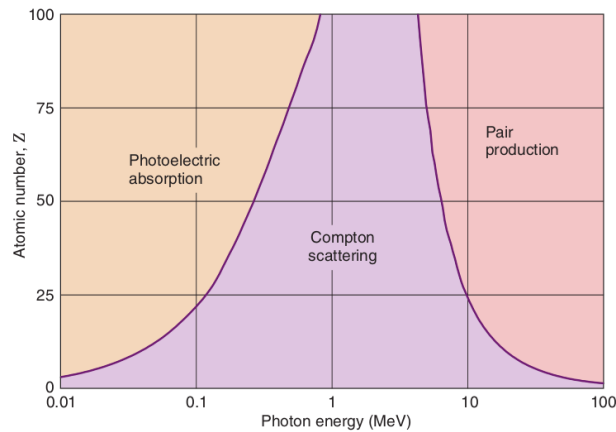


FIGURE 1.6: Main photon interactions versus photon energies for different atomic number [43].

1.2.5 Photon attenuation

When a photon beam passes through an object, some of the photons interact with the material and the beam intensity is attenuated. This effect depends on four factors: thickness, density, atomic number, and the photons energy. The beam intensity follows this equation widely known in literature [45, 46, 47]:

$$I_x = I_0 e^{-\mu(\rho, Z, E)x}. \quad (1.14)$$

Isotope	Function	Reference
Fluorine-18	glucose metabolism	[48]
Scandium-44	neuroendocrine system	[49]
Oxygen-15	blood flow	[50]
Nitrogen-13	myocardial blood flow	[51]
Carbon-11	neuron-transmettors	[52]

TABLE 1.2: Common radiotracers and some of their specific applications.

where I_0 is the initial intensity of the beam, μ is the linear attenuation coefficient depending on the density ρ , on the atomic number Z , and on the photons energy, and x is the thickness of the object. The linear coefficient can be seen as a measure of the probability of photon attenuation in a material unit length $[\mu]=\text{cm}^{-1}$.

1.3 PET imaging

PET imaging is used to obtain the uptake distribution of a radiopharmaceutical in the patient's body, mostly in oncological studies, before and after treatment and during radiotherapy. PET scans are also important diagnostic tools in neurology for degenerative disease, for example Alzheimer's. See Table 1.2 for some common radiotracers and their conventional applications.

Fig. 1.7 shows the schematic functioning of a PET exam: first a radiopharmaceutical labeled with a β^+ emitter is injected in the patient body. After a certain amount of time determined by the marker half life, the isotope decays emitting a positron. The particle travels in the body losing its energy until it annihilates with one of the surrounding electrons. Positron-electron annihilation results in two nearly co-linear photons, each carrying 511 keV of kinetic energy. Data acquisition starts when the patient is positioned in the scanner. The radiation reaching the detector is converted in electric pulses, which are collected in the acquisition system to be analyzed and reconstruct the image.

The detection is based on the knowledge of these two photons' characteristics: co-linearity and 511-keV of initial energy. Several factors can influence the correct event detection, among them we find scattering in the body and/or in the detector and positron range.

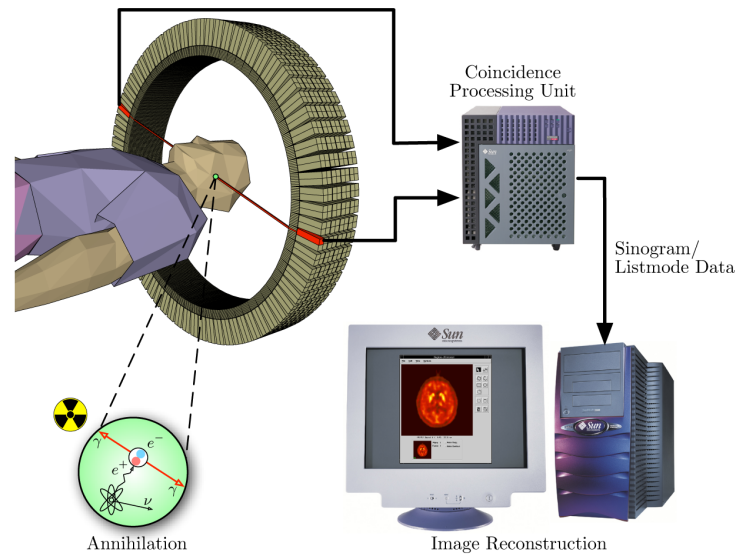


FIGURE 1.7: Complete process of a PET scan exam [53].

Properties	$\text{Bi}_4\text{Ge}_3\text{O}_{12}$ [29]	Lu_2SiO_5 [29]	Gd_2SiO_5 [29]	plastic [55]	LXe [4, 56]
Density [g/cm^3]	7.13	7.40	6.71	1.03	2.9 (at 168 K)
Atomic number	74.2	65.5	58.6	water-like	54
Decay constant [ns]	300	40	60	2.5	4.3

TABLE 1.3: Physical properties of some common detectors in PET.

1.3.1 Detection

Conventional PET cameras are composed of a first layer of detector mean (e.g. scintillators) and a second layer of photo-detectors (e.g. photomultiplier tubes). The detection material needs to convert the radiation signal into visible light and to fulfill some properties in order to be suitable for PET imaging: good stopping power for 511-keV photons, short signal decay time, high light output, and good energy resolution. Some of the most common PET scintillators are organic, such as bismuth germanate ($\text{Bi}_4\text{Ge}_3\text{O}_{12}$), lutetium oxyorthosilicate (Lu_2SiO_5), gadolinium oxyorthosilicate (Gd_2SiO_5), or plastic as well as liquid or gaseous (e.g. LXe, argon) [54]. Table 1.3 shows some conventional scintillators and their density, atomic number, and decay constant.

The scintillating material needs to be coupled to an electronic system equipped with a light detector to collect the radiation light yield. There are two principal ways: the one-to-one coupling technique (one crystal for one photo-detector) and the block detector one (multiple crystals coupled to the

same photo-detector through a light guide). The coupling system to adopt is chosen upon a study on the photodetector and on the scintillator to employ. If a light guide needs to be used, the properties of the transparent material ought to match the scintillator: similar refraction index, almost no reflection and so on.

The event detection and acquisition process occurs as follows: a photon scintillate in the detector producing light, that is converted into a pulse from the PMT, giving information about the position of the incident photon. Two pulses belonging to the same time window are recorded together as a coincidence. The line connecting the two detected events is called LOR and it joins two sides of the detector, crossing the field of view (FOV), where the patient is located.

Scintillation in LXe

The way photons are produced depends on the type of scintillator we are using; in LXe this can happen via atomic ionization or atomic excitation [57, 58]. The atomic excitation consists of the excitation of an atom in the xenon by a photoelectron, that combines with another xenon atom creating an excited dimer. After few picoseconds, the dimer de-excites and emits an ultraviolet photon. For the atomic ionization case, the photoelectron creates an electron-ion pair with one of the xenon atoms, that combines with another atom producing an ionized dimer. Eventually, a visible photon will be emitted in the same way as in the atomic excitation case [4].

Photodetectors

The conversion between radiation and visible light is performed by a photodetector, typically a PMT. Fig. 1.8 shows a scheme of the most common photodetector used in PET imaging. The functioning is the following: a 511-keV photon is converted into a visible photon inside the scintillator, and the light particle strikes the PMT surface and, due to photoelectric absorption, some photoelectrons are emitted. The electrons are directed, through a focusing electrode, to the first of a series of dynodes. On each dynode is applied a voltage higher than on the previous dynode, in order to accelerate the electrons and multiply them through secondary emissions. The signal is then collected at the end of the PMT on the last dynode, called anode.

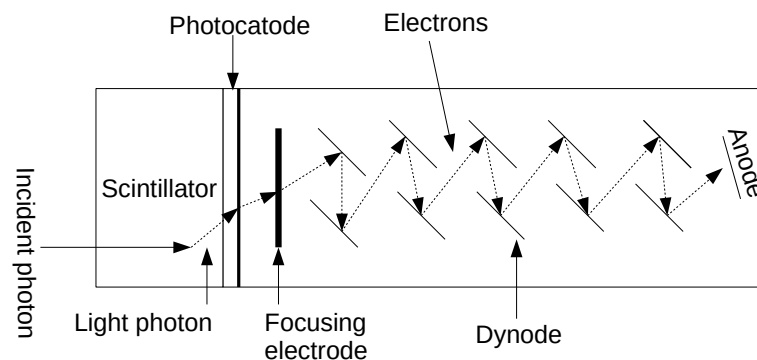


FIGURE 1.8: Schematic functioning of a PMT.

The total number of electrons that reach the end of the PMT for each photoelectron defines the *gain* of the PMT, which is normally around 10^5 - 10^8 [59]. The current pulse contains both time and energy information about the arrival of the photon on the PMT photocatode.

Other photodetectors based on semiconductors (i.e. Silicon PMTs) are also widely used in medical imaging due to their insensitivity to the magnetic field.

1.3.2 Coincidences

In PET imaging we are interested in the collection of coincidences, since we aim at detecting the two 511-keV photons produced by the same annihilation. Due to several factors (e.g. spatial and energy resolution of the detector, scattering in the phantom, positron range, etc.) the acquired coincidences do not always cross the real annihilation point.

In a classical PET acquisition we can find three types of events: true, random, and scatter coincidences. With true coincidence we denominate the ideal case in which two photons that do not undergo significant interactions before being acquired, track a correct LOR. In the other two cases, we have an effect of LOR mispositioning, that carries an error on the activity distribution. A scatter coincidence occurs when one or both photons are scattered before being detected and it is more likely to happen in large objects, see Fig. 1.9, example 1. We refer to a random event if the coincidence photons do not belong to the same annihilation event, see Fig. 1.9, example 2 and 3. Random events

can be due to a large time window or to multiple annihilations occurring in the same time window.

These events add bias to the reconstructed image if not accounted for properly: for the randoms it increases proportionally to the amount of activity A as $2\tau A^2$, where τ is the coincidence resolving time of the system. We can limit their acquisition by working with a narrow time window and with a good time resolution scintillator. Moreover, for scattered events we can work with an energy window (> 400 keV), rejecting events that lost already a conspicuous part of their energy, and use detectors with a high energy resolution.

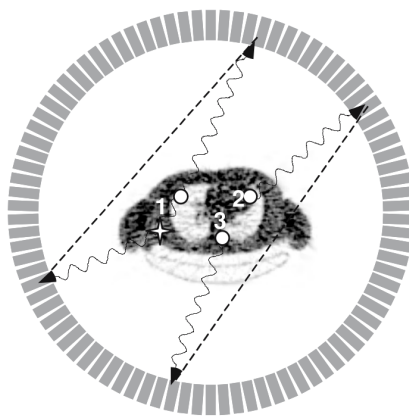


FIGURE 1.9: Event 1 represents a double scattered event, events 2 and 3 show a random coincidence. [29]

1.3.3 Sensitivity and Depth Of Interaction

The term sensitivity referred to a PET system indicates the ability to detect photons and it mainly depends on two characteristics: the detector stopping

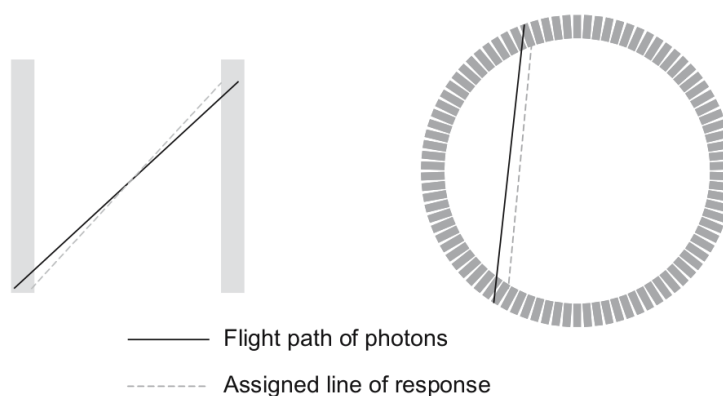


FIGURE 1.10: Parallax error due to the unknown event DOI [29].

power and the scanner geometry. High sensitivity is often related to a large solid-angle coverage in the scanner, as in the case of narrow and long axial FOV, and of a material with high atomic number.

The ability of efficiently contain and detect photons is useful not only to improve the sensitivity but also to account for another phenomenon, called the DOI effect. When a photon enters the detector, its interaction position is determined on the detector entrance surface and it is not the actual interaction point. If the detector is sufficiently deep for these coordinates to not match the actual interaction point, we have an effect of LOR mispositioning, that increases with the depth, as seen in Fig. 1.10. This effect is important especially for deep detectors and in the oblique coincidence case, for which every recorded event carries a systematic error that needs correction.

1.3.4 Time of Flight PET

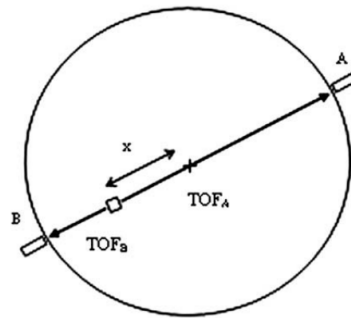


FIGURE 1.11: TOF-PET scan model: A and B represent the detectors and X the position of the annihilation respect to the scanner center. The time registered in A and B is proportional to the distance TOF_A and TOF_B [60].

The idea of using the arrival time of the two photons to locate the annihilation point developed in the 80s, when the first TOF-PET systems were built. Such systems were designed to improve the SNR of the reconstructed images and reduce the random rate acquisition.

In TOF-PET we impose a time window on the coincidence detection (few ns), in order to accept photons belonging to the same annihilation, and we record the time difference between the two. If we assume to have an ideal detector with a perfect time resolution, we can determine the location x of the event on the LOR as follows:

$$x = \frac{c\delta T}{2}. \quad (1.15)$$

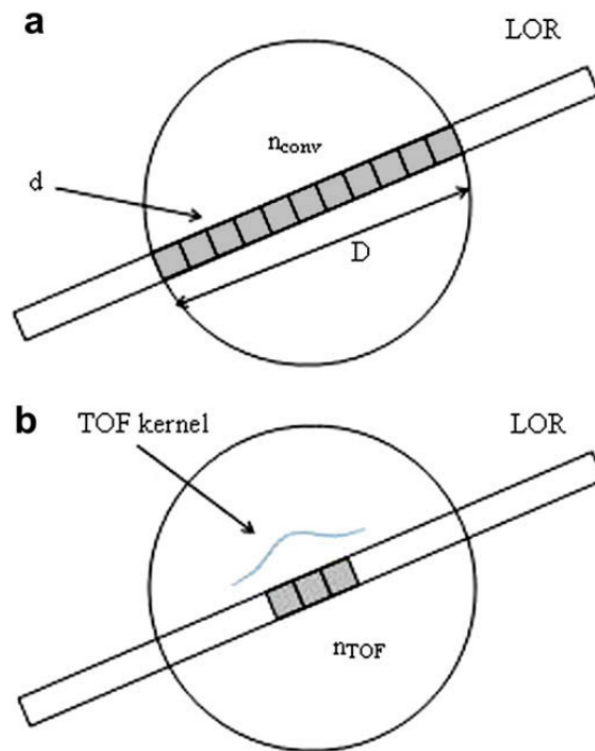


FIGURE 1.12: (a) classical PET reconstruction, (B) TOF probability, in which the time resolution δt limits the number of voxels contributing to the event [60].

where c is the speed of light and δT the arrival time difference between the photons, see Fig. 1.11.

In the ideal case, using only the LOR coordinates and the time difference, we can determine the annihilation point in a 3D volume, without passing through image reconstruction [61].

In reality we need to consider the actual time resolution of the detector, which gives us the uncertainty on the position computed through Eq. (1.15). We can see in Fig. 1.12 how the localization through TOF is considered the center of a Gaussian distribution, whose FWHM depends on the time resolution. For example, with a 600 ps timing resolution our uncertainty on the LOR would be around 9 cm.

The main difference compared to conventional PET is that in classic reconstruction the probability associated with the LOR voxels is the same for each of them, while in the TOF case we give a Gaussian-shaped distribution to the LOR.

Looking at the benefits carried by this technology, we could list noise reduction, especially for little objects [62], the earlier convergence of the

iteration method and at a clinical level, the reduction of the acquisition time due to the improvement in image quality. As for the SNR reduction compared to non-TOF-PET, the gain factor can be seen from the following equation from [62]:

$$\frac{\text{SNR}_{\text{TOF}}}{\text{SNR}_{\text{non-TOF}}} = \sqrt{\frac{D}{\Delta x}}. \quad (1.16)$$

where D is the size of the patient body and Δx the spatial equivalent to the TOF measurement. The gain factor depends on the size of the emitting object, thus we expect a higher value for heavier bodies. For a 20-cm-diameter object (human head) we have a gain around 2.1, with a scanner time resolution of 300 ps. No high improvements in terms of SNR is expected in TOF small animal systems, however for clinical scanners the SNR gain is exploited to reduce the acquisition time and the injected dose [63].

Chapter 2

Image Reconstruction

Summary

This chapter is an introduction to image reconstruction as historically developed, from analytical to iterative algorithms. We begin introducing the concept of sinogram and projection in data acquisition and we present the image reconstruction theory starting with analytical methods, in two-dimensional (2D) and in 3D. Afterward we pass over to iterative image reconstruction algorithms mentioning many of them (algebraic reconstruction technique (ART), simultaneous ART (SART), simultaneous iterative reconstruction technique (SIRT), multiplicative ART (MART)) and going in the specific of MLEM and OSEM. At last, we introduce the system modelization through the system matrix (SM), with a look into the correction factors for geometrical effects, attenuation and positron range.

Contents

2.1 Introduction	42
2.2 Data acquisition	43
2.2.1 Deadtime	44
2.3 Analytic Image Reconstruction	44
2.3.1 2D analytic image reconstruction	45
2.3.2 Back-projection	47
2.3.3 3D analytic image reconstruction	49
2.3.4 Back-projection	50
2.4 Model-based Image Reconstruction	51
2.4.1 Iterative algorithms	53

2.5 System modelization and corrections	58
2.6 System matrix	58
2.6.1 Detector geometry	59
2.6.2 Attenuation and normalization	59
2.6.3 Positron range	60
2.7 Scattering and random coincidences	60

2.1 Introduction

Tomographic image reconstruction aims to form images of the radiotracer distribution in the patient's body starting from raw PET data. In the data acquisition process we collect LORs through projections or coordinates pairs and the image reconstruction process can be seen as the estimation of the function $f(x): \mathbb{R}^n \rightarrow \mathbb{R}$, with $n = 2, 3$ for a 2D or a 3D image. $f(x)$ gives the value of the image in the point x and it corresponds to the activity distribution, following this equation:

$$E_{\text{det.photons/second}} = \int \int_{\text{VOR}} s(x)f(x)dx. \quad (2.1)$$

where the integral is on the volume of response (VOR), the parallelepiped that joins the pair of detector in which the coincidence occurred, and $s(x)$ is the scanner sensitivity.

If we consider the ideal case without attenuation, random or scattered coincidences, and detector geometry effect, we can assume that the total number of events detected in this volume is proportional to the amount of activity in the same.

In image reconstruction, there are two types of algorithms to obtain images: analytical and model-based or iterative. Analytical techniques are based on back-projection, an inversion of the data, collected as projections. Statistical or iterative image reconstruction uses complex computational models, which are based on a statistical pattern of the acquisition, including all prior information about the radiotracer and the biodistribution.

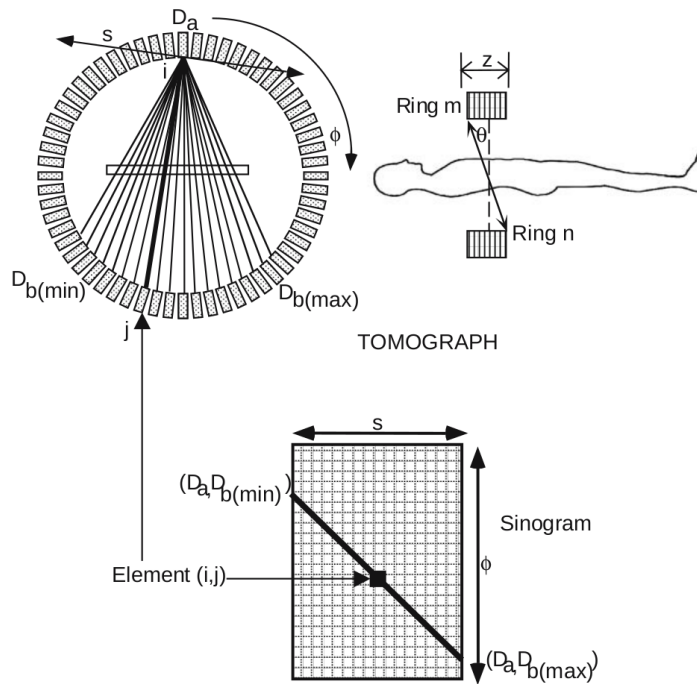


FIGURE 2.1: From projections to sinograms. [29]

2.2 Data acquisition

In PET imaging, data acquisition consists of collecting the information on the coincidence photons, looking for the detection of colinear 511-keV gammas in the time and energy acceptance windows.

In order to collect a high number of events and to maximize detector sensitivity, a PET system is typically composed of multiple ring-shaped detectors with a wide-volume coverage around the patient, positioned in the center. All events are recorded, including scattered and random coincidences, and raw data are stored in sinograms [64, 65].

In the data acquisition process detectors produce coincidence pairs with opposed detectors (axially and transaxially), which form a LOR identified by the rotational angle ϕ and the radial displacement s , see Fig. 2.1. Every LOR is collected in a sinogram, a bi-dimensional array in which each voxel corresponds to a single LOR and the voxel value is incremented every time a coincidence matches the same LOR. Events along the same row in the sinogram represent events associated with parallel LORs. If the acquisition occurs in LM the events are collected separately, one by one.

During the reconstruction process, we need to consider a correction factor for LORs' spacing, since they tend to be closer together as we approach the

edge of the ring; this effect is not considered during the acquisition.

In TOF-PET the difference in time between the coincidence photons arrival is also measured and stored. For a LM acquisition the δt -value is stored event by event, while in sinogram mode the sinogram is divided into several TOF-bin, each of them corresponding to a time difference.

2.2.1 Deadtime

All detectors present a limit due to the data treatment speed. When a PET system starts the event acquisition, there is a time interval in which other events cannot be detected, due to the system saturation while treating the first impulse. This amount of time is defined as the *deadtime* of the system. It is mostly due to the time the electronics take to register the first signal, but it can also depend on the scintillation time of the detector's material. This time gap can be seen as a blind time for the detector, during which we are unable to treat new interactions, and it is characteristic for each scanner.

In most high count rate situations another effect can affect measurements, known as *pile-up*. This happens when two signals arrive too close to each other and are summed up as one signal only, leading to energy resolution degradation and a count rate loss [66].

2.3 Analytic Image Reconstruction

Analytical approaches are based on the hypothesis that for every registered event we have a measure of the line integral associated that describes the radioactive distribution on the line. The first to solve this problem was Radon, in 1917 [67]. He proposed what we call the *Radon transform*, illustrated in Fig. 2.2:

$$Rf(s, \phi) = \int_{L_{s,\phi}} f(x, y) dx dy = \int_{-\infty}^{\infty} f(s \cos \phi - l \sin \phi, s \sin \phi + l \cos \phi) dl. \quad (2.2)$$

in which $L_{s,\phi}$ is the unit sphere, s and ϕ are the radial displacement and the angle that determine the LOR and $f(x, y)$ is the function to be determined. Actually, the integral is constrained by the FOV size and it occurs only between $-R_{\text{FOV}}$ and R_{FOV} .

In TOF-PET systems the same equation becomes:

$$R_{\text{TOF}}f(s, \phi, t) = \int_{-\infty}^{\infty} f(-s \sin \phi + l \cos \phi, s \cos \phi + l \sin \phi) h(t - l) dl. \quad (2.3)$$

where t is the time difference and $h(t)$ is the Gaussian kernel used to modulate the probability on the LOR.

FIGURE 2.2: Projection of an image and its Radon transform [68].

Analytical image reconstruction is considered to give direct results and linearity, which allows to better control noise correlation during the reconstruction process; and for its speed, mandatory in large 3D data sets [69].

2.3.1 2D analytic image reconstruction

Some properties of the Radon transform need to be stressed out: first, the operator R is *linear*

$$R[f + \lambda h] = Rf + \lambda Rh, \quad (2.4)$$

It is also continuous and *invariant for rotations* [29]:

$$Rf(-s, \phi + \pi) = Rf(s, \phi). \quad (2.5)$$

This is valid for scanners that collect all the LORs crossing the object, corrections to raw data need to be applied in case of incomplete scanner ring, to cover for the missing part of data, for example through interpolation.

The main objective of analytical reconstruction is to reconstruct an image f , given a sinogram g , for which:

$$g(s, \phi) = Rf(s, \phi). \quad (2.6)$$

meaning that we need to find R^{-1} the inverse operator of R .

Let us introduce the *central slice theorem* [70, 71], which ties the 2D Fourier transform $F_2\{(x, y)\}$ of the function $f(x, y)$ to the 1D Fourier transform $F_1\{(x, y)\}$ of the Radon transform $p(s, \phi) = Rf(s, \phi)$, an illustration of the theorem is shown in Fig. 2.3.

For all $(s, \phi) \in Z$:

$$g_\phi(s) = Rf(s, \phi), \quad (2.7)$$

we can write then:

$$\hat{g}_\phi(\sigma) = \hat{f}(\sigma\omega(\phi)). \quad (2.8)$$

where $s = \mathbf{r} \cdot \omega(\phi)$ with $\mathbf{r} \in \mathbb{R}^2$ and $\omega(\phi) = (\cos \phi, \sin \phi)$.

For a fixed angle ϕ we can write:

$$\hat{g}_\phi(\sigma) = \int_{\mathbb{R}} e^{-2i\pi\sigma s} g_\phi(s) ds = \quad (2.9)$$

$$= \int_{\mathbb{R}} e^{-2i\pi\sigma s} \int_{\mathbb{R}} f(s\omega^\perp(\phi) + t\omega(\phi)) dt ds. \quad (2.10)$$

Let \mathbf{r} be equal to $s\omega^\perp(\phi) + t\omega(\phi)$, $d\mathbf{r} = dt ds$ and $\mathbf{r} \cdot \omega(\phi) = s$:

$$\hat{g}_\phi(\sigma) = \int_{\mathbb{R}} e^{-2i\pi\sigma \mathbf{r} \cdot \omega(\phi)} f(\mathbf{r}) d\mathbf{r} = \hat{f}(\sigma\omega(\phi)). \quad (2.11)$$

We can now find the values of $f(x, y)$ relative to the image through an inverse Fourier transform, this algorithm is also called *direct Fourier reconstruction*:

$$f(\mathbf{r}) = \frac{1}{2} \int_0^{2\pi} \int_{-\infty}^{\infty} |\sigma| \hat{g}_\phi(\sigma) e^{2i\pi\sigma \mathbf{r} \cdot \omega(\phi)} d\sigma d\phi. \quad (2.12)$$

where $|\sigma|$ is a ramp filter. Ramp filtering can be seen as a convolution in the spatial domain or as a multiplication in the Fourier domain.

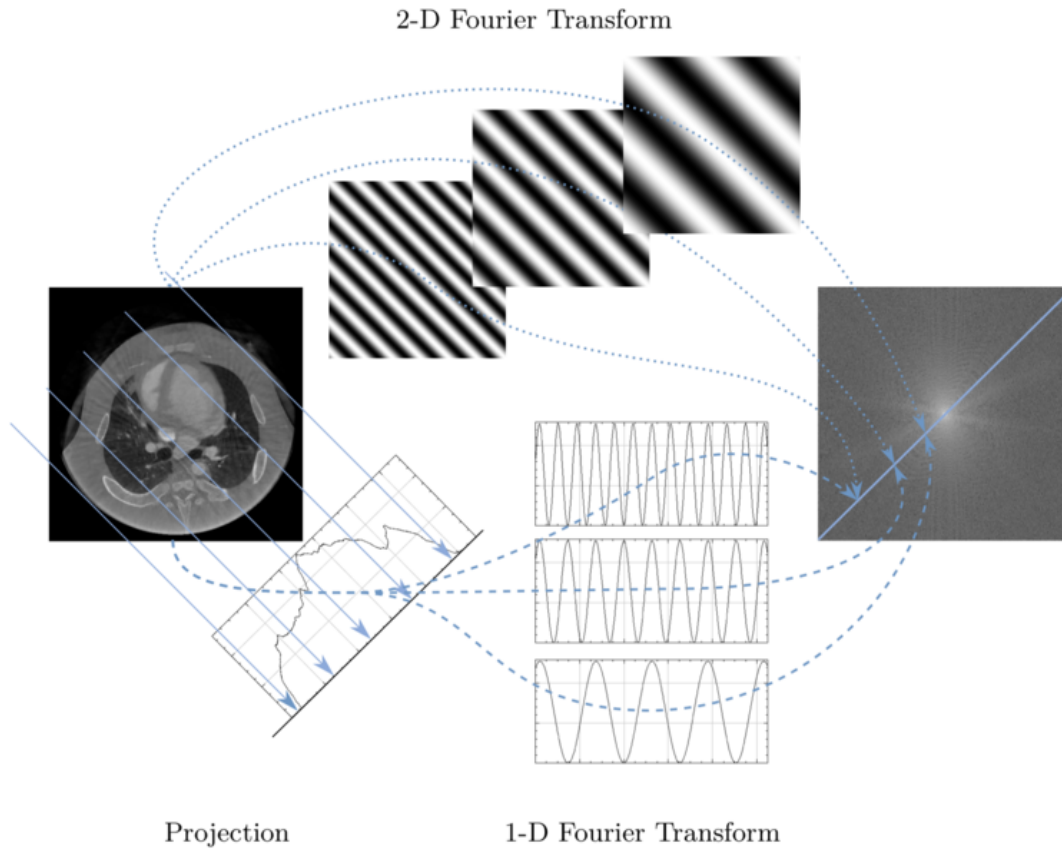


FIGURE 2.3: Central section theorem in 2D [72].

2.3.2 Back-projection

Two of the main operators in image reconstruction are back-projection and its adjoint, forward projection. They can be seen as the Radon transform (forward projector) and its adjoint, the back-projection operator R^* , defined as:

$$R^* p(s, \phi) = \int_0^{2\pi} p(x \cos \phi + y \sin \phi, \phi) d\phi. \quad (2.13)$$

and for a fixed angle ϕ is also valid:

$$b^1(x, y; \phi) = p(x \cos \phi + y \sin \phi, \phi). \quad (2.14)$$

where $b^1(x, y; \phi)$ is the 2D function formed through the back-projection of the single projection indexed by ϕ .

In reality, we do not observe directly $g = Rf$, but a noisy version of it:

$$g_\epsilon = Rf + \epsilon. \quad (2.15)$$

Noise is amplified by the back-projection operation, in fact if we take the norm:

$$\|R^*[g + \epsilon] - R^*g\|_X = \|R^*\epsilon\|_X. \quad (2.16)$$

where X is the image space, $R^*g = f$ and $\|R^*\epsilon\|_X$ does not tend to zero when $\epsilon \rightarrow 0$. A small perturbation on g can disrupt the reconstruction of f . A solution to this problem is to apply a ramp filter $|\sigma|$, the Jacobien of the transformation, which amplifies high frequencies corresponding to the image details, since high spatial resolution requires high frequency information. The ramp filter in 2D is obtained through apodization and discretization, using the fact that we can sample $|\sigma|$ resulting in a *discrete ramp-filter* [73].

This method is called *back-projection filtering* or *FBP* [74], depending on when the filter is applied. The ramp filter could not be sufficient due to its behavior that ensures high spatial resolution at the expense of noise, especially since it carries the

FBP is the most traditional image reconstruction approach. It is based on an idealized model that does not consider noise, scatter, attenuation, and other real data important features. In fact, it assumes that the number of detected events in a specific direction can give an approximation of the radiotracer distribution along the same direction, that is one of the projections introduced earlier. The only way to consider noise in FBP is smoothing the projection before image reconstruction.

$$f(x, y) = \int_0^\pi R^F f(s, \phi) d\phi. \quad (2.17)$$

where $R^F f(s, \phi) = F_1^{-1}\{|\sigma|F_1\{p_\phi(s)\}\}$ is the filtered projection, $|\sigma|$ being the ramp filter. The FBP method works as follows: first, the data are collected through a projection for a specific angle and a sinogram is created; then the algorithm exploits the back-projection operation to smear each projection back to the region along with the acquired direction (or angle) of acquisition. Adding the back-projections for all the angles, we will obtain a blurred approximation of the original object. Sharpening the projections is also possible, using a Fourier filter [75]; although analytical methods like FBP are mostly used to produce fast and practical solutions that highlight issues about data acquisition. Techniques which are used to implement real statistical estimations are of the iterative kind and they include the corrections already in the reconstruction process [76].

2.3.3 3D analytic image reconstruction

One of the main 3D reconstruction's challenges is the time-consuming computation. Due to this problem, the first reconstructed 3D volumes were ensembles of independent 2D reconstructions [77]. Other methods were also used to avoid long computation time as for example transforming 3D projections into 2D ones through *rebinning*, *single-slice rebinning* [78], *multi-slice rebinning* [79], *direct Fourier* [80] and *Fourier rebinning* [81].

Image reconstruction algorithms using directly 3D sinograms are called *fully 3D* and the methods seen for 2D can be extended to this category. In order to generalize them, we need to introduce a representation for the fully-3D data, the Radon transform operator in 3D can be written as follows, see Fig 2.4:

$$Rf(t, \hat{\mathbf{o}}) = p(t, \phi, \theta) = \int \int \int_{\mathbb{R}^3} f(\mathbf{x}) \delta(\mathbf{x} \cdot \hat{\mathbf{o}}(\phi, \theta) - t) d\mathbf{x}. \quad (2.18)$$

where $\delta(x)$ is the Dirac function and the vector $\hat{\mathbf{o}}(\phi, \theta)$ locates the plane related to $t \in \mathbb{R}$, signed distance between the origin and the perpendicular plane to $\hat{\mathbf{o}}(\phi, \theta) \in S^3$, where S^3 is a 3D unit sphere.

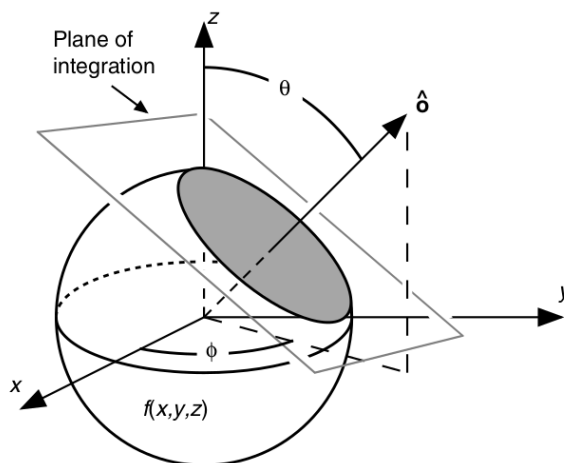


FIGURE 2.4: Integral of a 2D plane used for the Radon transform of a 3D object [75].

Before approaching the analytic algorithms for 3D data, we need to introduce the 3D generalized central slice theorem, that states the equivalency between the 2D Fourier transform of a projection of arbitrary direction $\hat{\mathbf{z}}(\phi, \theta)$ and the central section of the 3D Fourier transform of the object at the same angle. This implies that the image can be reconstructed from a set of non-truncated projections, if the set has an intersection with every equatorial circle

on the sphere S^2 . What is known as Orlov's condition assesses that the image can be reconstructed from the set of non-truncated projections if there is no great circle on the unit sphere that does not intersect the set of non-truncated 2D parallel projections. We can imagine that the acquisition is repeated for a large range of z and once we get the stack of images from different planes we can form a 3D image. This is a way of considering 3D imaging, although the fully 3D imaging includes the acquisition on all the planes perpendicular to the scanner axis, called direct planes, and on all the oblique planes that cross the direct planes as well, in Fig. 2.5 some examples of different 3D reconstructions.

FIGURE 2.5: From left to right: reconstructions from fully 3D PET data on the left, 2D rebinned non-TOF, 3D rebinned non-TOF and fully 3D PET-TOF [82].

2.3.4 Back-projection

For the 3D back-projection operation, it is often more efficient to back-project keeping a fixed direction (fixed angles ϕ and θ) and placing back the values of the projection into a 3D array along the corresponding LORs.

$$b^1(x, y, z; \phi, \theta) = p(\mathbf{r} \cdot \hat{\mathbf{o}}(\phi, \theta), \phi, \theta). \quad (2.19)$$

where $\mathbf{r} = (x, y, z)$. The complete back-projection can be obtained integrating in $d\phi$ and $d\theta$.

To better understand the parallel with the 2D case, we can derive the FBP equation to be used in reconstruction, for which the back-projection operator

can be written as:

$$R^*g(\mathbf{r}) = \int_{S^2} g(\mathbf{r} \cdot \hat{\mathbf{o}}, \phi) d\hat{\mathbf{o}}. \quad (2.20)$$

Filtering in 3D becomes more complex: we can see the 2D filter as the cross-section of the 3D one. For symmetry the filter will be independent of the projection angle ϕ , but dependent on θ and on the maximum acceptance angle [83].

If we write $g_{\hat{\mathbf{o}}}(t) = Rf(t, \hat{\mathbf{o}})$, we obtain:

$$f(\mathbf{r}) = \frac{1}{2} \int_{S^2} \int_{-\infty}^{\infty} |\sigma|^2 \hat{g}_{\hat{\mathbf{o}}}(\sigma) e^{2i\pi\sigma\mathbf{r} \cdot \hat{\mathbf{o}}} d\sigma d\hat{\mathbf{o}}. \quad (2.21)$$

Reconstruction with analytic techniques remains more efficient for very large 3D data sets, especially when multiple data sets are acquired in whole-body or dynamic studies, due to the amount of required time. However the speed is not the only FBP strength: analytic algorithms are linear and thereby allow easier control of the spatial resolution and noise correlations in the reconstruction.

2.4 Model-based Image Reconstruction

Tomographic image reconstruction can be seen as the operation of inversion of the Radon transform. This simplistic approach can be solved through FBP, without considering random detection, scattering in the tissues and the acquired data's noise properties. Unlike analytic approaches, statistical methods incorporate all known information in a discrete framework: through \mathbf{A} the SM, detailed in section 2.6, we are able to discretize the problem and consider attenuation, noise, scattering, detector response, and *a priori* information about the images.

For analytic methods we required some common steps to reconstruct (i.e. filtering and back-projection), for iterative methods, we need five elements:

- *Basis function*: the whole image is discretized and composed of basis functions, for example, voxels. This way the image can be represented as a vector of basis function coefficients (i.e. the voxel's uptake), and we deal with a discretized problem in the data and image domain.
- *System model*: a model including the scanner geometry effects and the physical effects on data acquisition.
- *Noise model*: this model concerns the data deviation from their expected

values based on a Poisson model.

- *Objective function*: the objective function measures the fit between the observed data \mathbf{p} and the modeled data $\bar{\mathbf{p}}$, that need to be optimized.
- *Numerical optimizer*: this is the mathematical algorithm that maximizes (or minimizes) the objective function.

All iterative methods are based on a first forward modeling step followed by a correction step. The activity is discretized voxel by voxel, every element a_{ij} of the SM corresponds to the probability of a positron emitted in the voxel j to be detected by the crystals' couple i , connected by a LOR.

$$\mathbf{p} = \mathbf{A}\mathbf{f} + \mathbf{n} = \bar{\mathbf{p}}(\mathbf{f}) + \mathbf{n}. \quad (2.22)$$

where \mathbf{p} is the measured projection, \mathbf{f} the radioactive distribution, and \mathbf{n} represents the projections' noise, that can be seen as a shifted Poisson variable, since $\mathbf{p} \sim \text{Poisson}(p; f)$.

As for maximizing (or minimizing) the discrepancy between measured and expected data $\bar{\mathbf{p}}$, we can take as objective function the *least-square (LS)* function [84]:

$$O_{\text{LS}} = \sum_{i=1}^I (p_i - \bar{p}_i(\mathbf{f}))^2. \quad (2.23)$$

where the sum is on the projection bins' values and p_i represents the measured data, while $\bar{p}_i(f)$ is the expected LOR data. In case we have some knowledge about the projection data, we can weight each element in the sum differently and obtain the *weighted-least squares (WLS)* function, in which the weights can be estimated directly from the projections of the current image estimate.

LOR projection data are typically based on Poisson statistics, due to the positron emission following the same probability, thus we can introduce the Poisson distributed objective function from Shepp and Vardi [18] known as the *maximum-likelihood (ML) function*:

$$O_{\text{ML}} = L(\mathbf{f}) = \prod_{i=1}^I Pr(p_i | \bar{p}_i(\mathbf{f})) = \prod_{i=1}^I \frac{(\bar{p}_i(\mathbf{f}))^{p_i} e^{-\bar{p}_i(\mathbf{f})}}{p_i!}. \quad (2.24)$$

where $Pr(p_i | \bar{p}_i(\mathbf{f}))$ is the Poisson distribution and it gives the probability of obtaining a measured value equal to p_i in the LOR i while $\bar{p}_i(\mathbf{f})$ is the expectation. The multiplication is due to the assumption that all the LOR counts are mutually independent and the probability of obtaining the vector \mathbf{p} is the product of the Poisson probabilities $L(\mathbf{f})$, also called likelihood [85].

Starting from Eq. (2.24), many algorithms have been proposed to maximize the logarithm of the likelihood:

$$l(\mathbf{f}) = \ln L(\mathbf{f}) = \sum_{i=1}^I (p_i \ln \bar{p}_i(\mathbf{f}) - \bar{p}_i(\mathbf{f}) - \ln p_i!). \quad (2.25)$$

where $\ln p_i!$ is a constant and it can be omitted. Since the log-likelihood $l(\mathbf{f})$ depends on \mathbf{p} , which are unknown measurements, we cannot directly calculate the ML estimate for \mathbf{f} , although there are algorithms to maximize the expected value of $l(\mathbf{f})$:

$$\hat{\mathbf{f}}^{(k+1)} = \underset{\mathbf{f}}{\operatorname{argmax}} \mathbb{E} \left[l(\mathbf{f}) | \mathbf{p}, \hat{\mathbf{f}}^{(k)} \right]. \quad (2.26)$$

ML estimators have interesting properties that make them useful in many situations. First of all they are *asymptotically unbiased*, their bias is reduced with the growth of the observations. Second, they are *asymptotically efficient* as they yield the minimum variance for large numbers. Although these properties make them not particularly susceptible to noise, their variance is still high and the images are often filtered to introduce spatial smoothing.

2.4.1 Iterative algorithms

The process of iterative reconstruction begins with an estimated $\mathbf{f}^{(k)}$ of the values in the image. The current image estimate is then projected, giving a set of values that would be expected if this was the true image. The predicted projections are then compared to the measured ones to elaborate a set of error values in the projection space. These are back-projected to obtain image-space error values that are used to update the image estimate $\mathbf{f}^{(k+1)}$. And this whole process is reproduced for each iteration.

The main difference with analytical back-projection-based algorithms is that there is no feedback about the image estimate in the direct reconstruction.

Another way to estimate \mathbf{f}^k is to find the image that satisfies all the constraints imposed by the measured data and the prior knowledge. *ART* [86] is one of the methods using this process: the difference between the measured value and the expected value is calculated for each LOR and through the transpose SM the correction is applied in the image space. Neglecting the

noise parameter from Eq. (2.22) we have:

$$\mathbf{f}^{(k)} = \mathbf{f}^{(k-1)} - \frac{\mathbf{a}_i \mathbf{f}^{(k-1)} - p_i}{\|\mathbf{a}_i\|^2} \mathbf{a}_i \quad (2.27)$$

where \mathbf{a}_i is the SM line associated to the i -th LOR. This algorithm corresponds to what is known as the *Kaczmarz method* [87], which allows the iterative solution of a system consisting of N equations in N unknown variables.

Taking Eq. (2.22) we can easily see how it represents a system of I equations of hyperplanes in the J dimensional space. The algorithm projects the current image vector $\mathbf{f}^{(k)}$ orthogonal on the hyperplanes and updates the image accordingly, as done in ART. Several algorithms originated from ART, i.e. *SART*, *SIRT* [88], *MART*, all neglecting the noise factor, thus not very efficient in PET imaging.

The most famous iterative algorithm for PET and SPECT is *MLEM*. It was studied by Shepp and Vardi [18], Dempster [89], Lange and Carson [90] and others. The basic problem consists in the estimation of an image vector \mathbf{f} from the counts measurements stored in a vector \mathbf{g} . f_i is the number of events taking place in the i -th voxel, and g_j is the number of events occurred in the j -th LOR connecting two detector elements.

Let \mathbf{A} be the SM, for which each element a_{ij} gives the probability of an event detected in the i -th LOR to have occurred in LOR bin j . The relation between the average number of events detected on a LOR and the matrix is then:

$$\mathbb{E}[\mathbf{p}] = \mathbf{A}\mathbf{f}. \quad (2.28)$$

where \mathbf{f} is the image we want to reconstruct inverting this equation.

Let \mathbf{p} be the incomplete observed data, incomplete because we only know that an event occurred on a LOR, we do not know exactly from where it originates. \mathbf{P} is the matrix having as elements the number of events detected on the i -th LOR that originated from the j -th bin. Being able to observe \mathbf{P} directly we could solve our problem as:

$$\hat{f}_j = \sum_i p_{ij}. \quad (2.29)$$

Since the likelihood depends on the elements p_{ij} , which refer to unknown measurements, we cannot directly calculate the ML estimate and obtain \mathbf{f} , thus we are going to maximize its expected value. From Eq. (2.26) we can

rewrite the expected value inserting the log-likelihood as:

$$\mathbb{E} \left[\sum_i \sum_j -f_i a_{ij} + p_{ij} \ln f_j a_{ij} \mid \mathbf{p}, \hat{\mathbf{f}}^{(k)} \right], \quad (2.30)$$

due to linearity we can rewrite:

$$\sum_i \sum_j \left(-f_i a_{ij} + \mathbb{E} \left[p_{ij} \mid \mathbf{p}, \hat{\mathbf{f}}^{(k)} \right] \ln f_j a_{ij} \right). \quad (2.31)$$

For the probability theory we know that for independent Poisson random variables, as p_{ij} and \mathbf{p} , the conditional probability distribution given the sum of its values, its a binomial distribution with parameters $\left(\sum_j p_{ij}, \frac{\mathbb{E}[p_{ij}]}{\sum_j \mathbb{E}[p_{ij}]} \right)$ [91].

With $\mathbb{E}[p_{ij}] = f_j a_{ij}$ we obtain:

$$\mathbb{E} \left[p_{ij} \mid \mathbf{p}, \hat{\mathbf{f}}^{(k)} \right] = p_i \frac{\hat{f}_j^{(k)} a_{ij}}{\sum_n \hat{f}_n^{(k)} a_{in}}. \quad (2.32)$$

Once the expectation value is developed, we can proceed with the maximization step:

$$\frac{\partial}{\partial f_l} \mathbb{E} \left[l(\mathbf{f}) \mid \mathbf{p}, \hat{\mathbf{f}}^{(k)} \right] = 0, \quad (2.33)$$

$$\sum_i -a_{il} + \sum_i \mathbb{E} \left[p_{il} \mid \mathbf{p}, \hat{\mathbf{f}}^{(k)} \right] \frac{1}{f_l} = 0, \quad (2.34)$$

$$f_l = \frac{\sum_i \mathbb{E} \left[p_{il} \mid \mathbf{p}, \hat{\mathbf{f}}^{(k)} \right]}{\sum_i a_{il}}, \quad (2.35)$$

$$f_l = \frac{\hat{f}_l^{(k)}}{\sum_i a_{il}} \sum_i \frac{a_{il} p_i}{\sum_n \hat{f}_n^{(k)} a_{in}}, \quad (2.36)$$

where f_l is the l -th component of our estimation. The MLEM equation is the following:

$$f_l^{k+1} = \frac{\hat{f}_l^{(k)}}{\sum_i a_{il}} \sum_i \frac{a_{il} p_i}{\sum_n \hat{f}_n^{(k)} a_{in}}. \quad (2.37)$$

In Fig. 2.6 we show the convergence properties of MLEM algorithm in different situations.

One of the characteristics of MLEM is the slow convergence: we need around 30-50 iterations to reach convergence, with a forward projection and a back-projection in each of them, meaning that it is twice as slow as FBP.

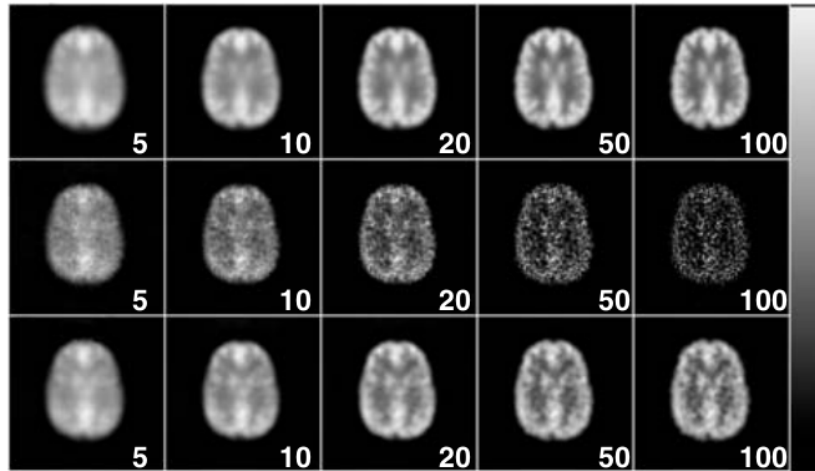


FIGURE 2.6: Convergence properties of MLEM algorithm from simulated SPECT brain data. First row noise-free images, second row noisy, third row noisy filtered reconstruction [92].

However, in general, MLEM performs better than any analytic method, due to the possibility of including nonuniform constraints.

Other algorithms can be obtained from similar logic, especially envisioning improvements of the MLEM algorithm, as for example to accelerate convergence and reduce the iteration number. An algorithm following this logic is the *OSEM*, in which the projections are divided in ordered subsets to reach convergence earlier [93, 94]:

$$f_l^{(k,m+1)} = \frac{f_l^{(k,m)}}{\sum_{i \in S} a_{il}} \sum_{i \in S} a_{il} \frac{p_i}{\sum_{l'} a_{il'} f_{k,m}^{(k)}}. \quad (2.38)$$

where m is the subset index, and S is the group of subsets [95, 96, 97]. To reach the one-iteration step all the subsets need to be treated, if only one subset is used, we go back to the MLEM algorithm. This modification of the MLEM algorithm leads to a more efficient update, due to the computation being a factor m smaller [98]. The main problem with OSEM is that we face an iterations limit corresponding to the number of subsets, thus convergence to an ML estimated is lost.

In all these algorithms the projections p_i are considered as the sum of the detected events in a bin, without considering the data format (sinogram or histogram). A variation of the MLEM algorithm was proposed in 1998 by Parra and Barrett [99] and later by others [100, 101, 102], in order to consider

LM data with no prior conversion:

$$f_l^{(k+1)} = \frac{f_l^{(k)}}{\sum_i a_{il}} \sum_{i \in \text{ML}} \frac{a_{il}}{\sum_{l'} a_{il'} f_{l'}^{(k)}}. \quad (2.39)$$

this algorithm is known as *list-mode expectation maximization (LMEM)* and ML represents the events index.

In Fig. 2.7 we can see some images obtained through OSEM reconstruction for different subsets number at different iterations. It seems that the OSEM algorithm has all the properties of the MLEM algorithm but requires fewer iterations to achieve a stable result, nevertheless, it adds the difficulty of choosing the right number of subsets.

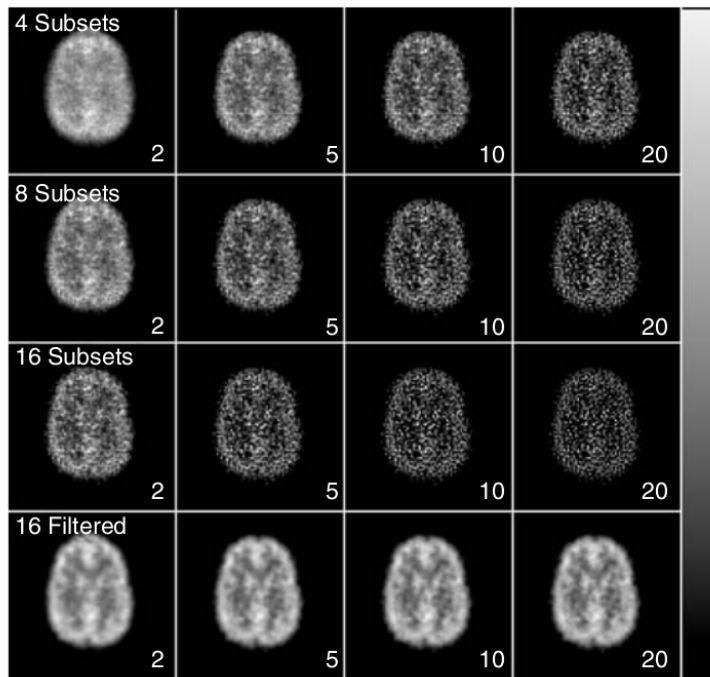


FIGURE 2.7: The images show the iterated image estimates of OSEM for SPECT brain data. For every image, we indicate the iteration number while the subsets number is reported on the left of each row [92].

All the methods shown in this section are *ray-driven*, although there exist some *voxel-driven* techniques. Instead of updating multiple voxel values based on some LOR values, they try to minimize (or maximize) the objective function on a single voxel basis [103, 104]. The minimum (or maximum) is found for a single value in the image and all the other values are constant. The procedure needs to be repeated for each voxel in order to end the iteration.

2.5 System modelization and corrections

To achieve a quantitative reconstruction in which we obtain the real radio-pharmaceutical's uptake in each voxel, we should model all the effects happening during data acquisition: the positron range, the scattering and the attenuation, etc. Evidences from multiple studies [105, 106, 107, 108, 109, 110] show that all these non-linear corrections can make a difference in the reconstructed image quality.

2.6 System matrix

Iterative algorithms model the system through a SM , which is applied to the forward and back-projection operators and its elements can include the corrections for the bias-carrying effects. Due to the matrix size (e.g. 10^{14} for a Philips PET system) and to the computation time required to calculate all the elements, the SM is not entirely stored and often computed on the fly. There exist several models to make the system matrix computation easier, one of which is known as the *factored system model* [111, 112], which considers the system matrix as a multiplication of matrices.

$\mathbf{A} \in \mathbb{R}^{M \times N}$ is the SM in which the element a_{ij} defines the probability of detecting an emission from voxel j , $j = 1, \dots, N$ in the detector i with $i = 1, \dots, M$, and we can express it as:

$$\mathbf{A} = \mathbf{A}_{\text{sens}} \mathbf{A}_{\text{blur}} \mathbf{A}_{\text{att}} \mathbf{A}_{\text{geom}} \mathbf{A}_{\text{positron}}. \quad (2.40)$$

where $\mathbf{A}_{\text{att}} \in \mathbb{R}^{M \times M}$ is a diagonal matrix containing the attenuation factors, expressed in cm^{-1} ; $\mathbf{A}_{\text{sens}} \in \mathbb{R}^{M \times M}$ is the normalization matrix, a diagonal matrix measured through the acquisition of a homogeneous cylinder; $\mathbf{A}_{\text{positron}} \in \mathbb{R}^{N \times N}$ is the matrix considering the positron range correction; $\mathbf{A}_{\text{geom}} \in \mathbb{R}^{M \times N}$ considers the geometrical sensitivity of the detector and it represents the probability that a photon pair produced in voxel j reaches the detector i in absence of other effects (attenuation and non-collinearity). \mathbf{A}_{blur} is the sinogram blurring matrix that considers non-collinearity, scattering in the detector, and DOI effect. In this section we present some of the over-mentioned effects and the correction approaches that can be adopted during the image reconstruction process.

2.6.1 Detector geometry

The SM detector geometry correction factor is mainly related to the parallax error, which can be worsened by the scattering in the detector [113], and it needs to be accounted for.

In the factored system model the correction is carried by the \mathbf{A}_{geom} matrix, which can be determined in advance through empirical [114, 115], analytical [116] or Monte Carlo based studies [69]; or on the fly to avoid large memory storage [117, 118]. The \mathbf{A}_{geom} matrix controls the projection operation between the image and the projection space: the forward projection is the multiplication of the image vector and the \mathbf{A}_{geom} matrix, while the back-projection is the multiplication of the projection vector and the $\mathbf{A}_{\text{geom}}^T$ (transposed matrix).

This operation can be carried on through two different strategies: the *LOR-driven* or the *voxel-driven* approach. The difference consists in associating the \mathbf{A}_{geom} 's coefficient to a LOR or to a voxel. In LM is normally preferred the LOR-driven method since each event is associated with a LOR, for the *voxel-driven* approach all the events have to be read in order to determine which LORs cross the considered voxel, with an increase of the needed computation time.

2.6.2 Attenuation and normalization

Before reaching the detector each photon is attenuated, first in the patient body and then in every detector layer crossed. The attenuation effect needs to be considered for each LOR separately due to the different trajectories. A CT scan of the imaged object is often used to estimate the attenuation coefficients [119]. Dual systems PET-MRI have also been developed, with the great advantage over PET-CT that the patient does not receive an additional radiation dose for the attenuation study [120, 121]. The main disadvantage of using MRI images is that the conversion from gray scale to attenuation coefficients is not a straightforward operation as different materials can be seen under the same color.

In the reconstruction process, images are normalized through the sensitivity coefficients that vary for each scanner and each acquisition. Usually the normalization values are obtained before reconstruction and stored in a sensitivity map, sized as the image. A proper calculation of the sensitivity coefficients takes in consideration the attenuation in the body and it is based

on a hour-long acquisition (real or simulated) of a homogeneous phantom covering entirely the FOV volume.

2.6.3 Positron range

Positron range correction is mandatory only for those acquisitions in which we employ a radiopharmaceutical emitting an energetic positron for which the range is relevant. In most PET imaging acquisitions, the employed radioisotope is F-18 which carries a submillimetrical correction, visible only if the detector resolution is higher, thus the A_{positron} matrix is often equal to the identity matrix I .

There are different ways to deal with the positron range effect, some methods to reduce it through the use of magnetic fields were developed in the past [122]. More recent approaches operate a correction on the projection or on the image. We can blur sinograms to simulate the average positron range [123], with the disadvantage that this method is valid only in sinogram mode. As an alternative, we can convolve (or deconvolve) the image during or after reconstruction. Different kinds of convolution can be applied: on the estimated image at each iteration, or directly on the reconstructed image. The convolution kernel needs to be studied in advance, especially for dishomogeneous objects: it strictly depends on the imaged object density, thus on the materials.

Another valid method is a Monte Carlo-based correction through the simulation of the positron propagation in the object. This method allows to reach a good correction factor, however, the use of GPUs is required [124].

2.7 Scattering and random coincidences

In clinical PET acquisition between 30 and 60% of the events undergo scattering before detection, consequently, the image quality is affected by a consistent amount of noise. A first approach to the correction of this phenomenon is the random coincidences estimation and subtraction. Hoffman in 1981 [106] showed that the random coincidences number increases as the square of the activity: the injected dose needs to be tuned in order to avoid a high number of scattered events and to have a reasonable amount of counts.

Other methods include the use of one or multiple energy windows [125] and the *single scatter simulation* by Watson [126]. This approach is based on

the estimation of the coincidences that scattered only once, calculated through the Klein-Nishina's formula (1.13). We can write the estimated number of coincidences detected by the AB pair that scattered only once, S^{AB} , as:

$$S^{AB} = \int_{V_s} dV_s \left(\frac{\sigma_{AS}\sigma_{BS}}{4\pi R_{AS}^2 R_{BS}^2} \right) \frac{\mu}{\sigma_c} \frac{d\sigma_c}{d\Omega} [I^A + I^B], \quad (2.41)$$

where V_s represents the scattering volume, s the scattering position, $\sigma_{AS,BS}$ the geometrical cross-sections of the two detectors and $\frac{d\sigma_c}{d\Omega}$ the total cross section from the Klein-Nishina's formula.

$$I^{A,B} = \epsilon_{AS}\epsilon'_{BS} e^{-(\int_S^A \mu ds + \int_S^B \mu' ds)} \int_S^{A,B} f ds. \quad (2.42)$$

where $\epsilon_{AS,BS}$ is the detector efficiency for 511-keV photons and $R_{AS,BS}$ are respectively the distances from the detectors A and B to the scattering point S ; at last, μ is the attenuation coefficient for 511-keV photons and f the emission density.

This method known as *single scatter simulation* (SSS) is widely used in PET for the estimation of the scatter contribution. When using SSS the modeled correction can be scaled to match the data through tail-fitting techniques [127], although they result in artifacts in the reconstructed images when the tail is too noisy or small. The SSS method is fast and it reaches good results for homogeneous phantoms, nevertheless it does not consider multiple scattered events, and corrections based on Monte Carlo simulations have shown better results [128]. Through a simulation of the photon propagation we can obtain the estimation of the scattered events and random coincidences distribution. The main advantage of the Monte Carlo method is that all the events can be simulated in a realistic way, going from no scattering to multiple scattering; the main disadvantage is related to the elevated computational cost in terms of time, that can be partly avoided via GPUs [129].

Chapter 3

3- γ Image Reconstruction

Summary

In this chapter, we get into the details regarding the geometry and the functioning of the XEMIS2 and we present the proposed 3- γ image reconstruction algorithm. We expose the calculation of the LCI coordinates, using Compton kinematics and LOR/Compton cone intersection. We then present the 3- γ or pseudo-TOF algorithm, whose name is due to the similarity between the proposed technique and TOF image reconstruction. We also present the Monte Carlo GATE simulation used for data acquisition, and the simulated phantoms. At the end of the chapter, we deal with the details of the image reconstruction software, CASToR. We explain the theory behind the 3- γ image reconstruction algorithm, defining the SM elements and presenting the implementation of the reconstruction algorithm into the CASToR framework.

Contents

3.1 Introduction	64
3.2 The XEMIS2 project	65
3.2.1 Scanner geometry	65
3.2.2 Radio-isotope	66
3.2.3 Detection	67
3.3 Proposed 3-γ image reconstruction technique	69
3.3.1 LOR/cone intersection	69
3.3.2 Requirements for 3- γ imaging	72
3.3.3 Pseudo-TOF image reconstruction	76

3.4 Simulation	79
3.4.1 Phantoms	80
3.5 Image reconstruction software	82
3.5.1 Pseudo-TOF system matrix	82
3.5.2 Pseudo-TOF algorithm in CASToR	83
3.5.3 XEMIS2 geometry in CASToR	84

3.1 Introduction

In recent times the use of imaging procedures has been growing as they develop and cover new and different diagnostics (oncological, neurological, etc.), and concerns about administered dose have been raised, especially regarding pediatric patients [9]. A typical amount of total activity for a PET study can span between 25 and 290 MBq [130] for clinical scanners and between 4 and 40 MBq for small animal systems [131]. In any case, we deal with around 10 mSv of administered dose for a total data acquisition time between 1 and 20 minutes. A dose reduction can cause image quality to degrade [10, 11], thus post-acquisition image processing and software-based methods may be used [13, 14] to recover SNR and contrast to noise ratio (CNR) in the images. New imaging devices have also been studied [15], in order to tackle this same problem, especially detectors and systems taking advantage of three-gamma detection [20, 21, 23, 24].

The notion of triple coincidence was first introduced by Liang in 1987 [132] and resumed in 2001 by Kurfess [133] for a solid-detector study. The J-PET [22, 19] project is based on the use of the three 511-keV photons originated from the ortho-positronium annihilation to reconstruct the time and position of the annihilation point on an event-by-event basis, using a TOF framework and reaching an average time resolution of around 40 ps.

In 2006 the team of Thers [6, 134] proposed a monolithic LXe detector used as a Compton camera. A first research project called xenon medical imaging system (XEMIS) was launched to study the feasibility of the novel LXe technology to detect and reconstruct a three-gamma signal generated from Sc-44, a positron and prompt gamma emitter. A small-dimension single-phase LXe time-projection chamber (TPC) known as xenon medical imaging system 1 (XEMIS1) was developed and tested [135] as a prototype. Promising results

from this preliminary study brought the project to the actual preclinical state with the XEMIS2 detector, a small animal LXe detector for 3- γ data acquisition, whose goal is to exploit the intersection of the LOR with the third-gamma Compton cone to narrow the annihilation position on the LOR. In recent years, other research teams started exploring the subject of 3- γ *direct reconstruction*, in which through the LCI we can obtain directly the annihilation position, with no need for tomographic reconstruction [136].

In this chapter we explore the proposed image reconstruction technique, we begin describing the LXe small animal imaging system, XEMIS2, suitable for 3- γ detection; we discuss the logic behind 3- γ image reconstruction, and we show the implementation and the challenges of the new technique.

3.2 The XEMIS2 project

The XEMIS2 project concerns a new small animal imaging system, whose technology has been developing at the Subatech laboratory in Nantes, France [137]. The camera uses LXe as detection mean and Sc-44, produced on-site by the ARRONAX cyclotron [138, 139, 140], as 3- γ (β^+ and γ) emitter. The goal is to produce good quality images with less administered dose, using the third-gamma information to narrow the annihilation position on the LOR.

3.2.1 Scanner geometry

The XEMIS2 is a whole-body camera for small animals that presents a particular geometry: an axially long FOV in a monolithic detector, in order to maximize the scanner sensitivity. In the XEMIS2 system we do not deal with crystals or block detectors, all the volume surrounding the small animal is filled with the detection medium, LXe. The scanner is a cylinder composed of two TPC filled with LXe; they are placed back to back and separated by a shared cathode. The active zone of detection goes from the inner 7-cm-radius cylinder to the outer 19-cm-radius cylinder and it is 24 cm long, 12 cm for each TPC, see Fig. 3.1.

All around the detector cylinder, there are 380 PMTs used to detect the scintillation light generated during photon-LXe interaction. A homogeneous electric field is applied between the cathode and the anodes, in order to drift the ionization charges and measure them on the anodes.

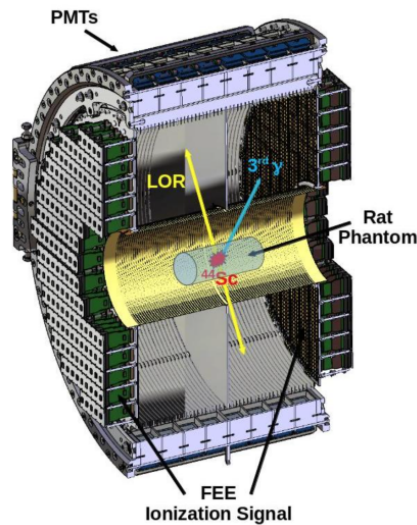


FIGURE 3.1: Transversal view of the scanner to show where the small animal is positioned, how the three gammas are emitted and where they are detected.

In Fig. 3.2 we see a schematic diagram of the active zone, showing only a quarter of the scanner, the rest being symmetrical. The animal is positioned in the 7-cm radius cylinder filled with air and to prevent him from experiencing hypothermia, all around the first Aluminum pipe there are 7.5 mm of vacuum and a supplementary 1.5-mm-thick cylinder of stainless steel.

In Fig. 3.3 we show the experimental setup of the XEMIS2 at the Subatech laboratory, including the cryogenic system to keep the xenon in the liquid state and to cyclically purify it [4].

3.2.2 Radio-isotope

The positron-and- γ emitter chosen for the XEMIS2 project is Sc-44. This radio-isotope is a good candidate for our study due to its 4-hour lifetime, ideal for medical applications. The most probable interaction is through β -decay, branching ratio (BR)=94.27% [141], with the emission of a positron and a neutrino it becomes Calcium*-44 (Ca^*-44). The emitted positron travels in the body and annihilates with an electron in the surroundings, while the Ca^*-44 de-excites emitting an 1157-keV photon with an isotropically distributed probability in space, see Fig. 3.4. Thus, the radiation that we can detect is composed of the two back-to-back photons generated in the annihilation, and the third gamma emitted during the de-excitation process. Due to the energy difference between the coincidence photons (511 keV) and the third

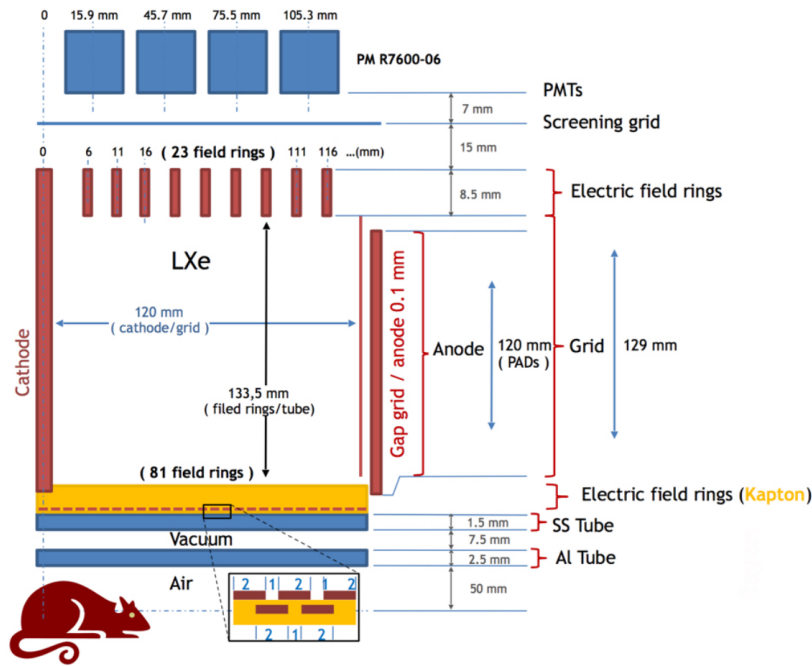


FIGURE 3.2: Scheme of the XEMIS2: layer and dimensions for one quarter of the scanner, the rest being similar through symmetry.

gamma (1157 keV), we are able to discriminate between the interactions in the acquisition process, and we can also exclude three-gamma cases deriving from the ortho-positronium state during positron decay.

An important characteristic of Sc-44 as positron emitter is the positron range. The particle is emitted in a range of energies that goes from 0 to 1474 keV, which leads to a mean positron range of 2.4 mm [37], versus the 0.5 mm of the most common PET radioisotope, F-18.

3.2.3 Detection

The main characteristic that makes LXe a suitable detection material for 3- γ detection is the excellent scintillation property, with 68 photons/keV and 2.2 ns of fast scintillation decay time. Due to its liquid state, the density is 3.100 g/mL and characterizes the material also as a high stopping power medium.

The photon detection process occurs as follows: due to the photon-LXe interaction in the active area, scintillation light is produced [142] and detected in the PMTs. This signal is used to trigger the event acquisition, giving the interaction's time and position on the z -axis [143, 144, 145]. All the other information regarding the event, as x - y position and released energy, are



FIGURE 3.3: XEMIS2 experimental setup at the Subatech laboratory: on the left the cryostat and on the right the camera.

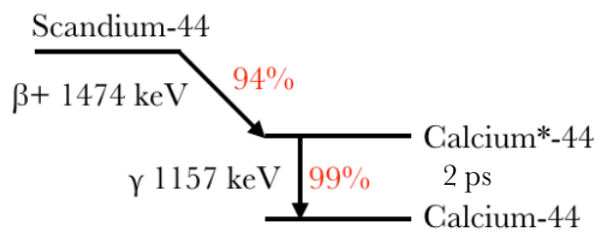


FIGURE 3.4: Decay scheme of Sc-44 [1].

gathered through the ionization signal's analysis. The ionization process produces electron-ion pairs and, to avoid recombination between pairs, an electric field is applied to drift the charges towards the segmented anodes. The signal is recorded on the anodes and it provides the $x - y$ position and the arrival time. The z position is computed through a trivial operation: $z = v_{\text{drift}} \cdot (t_{\text{arrival}} - t_{\text{trigger}})$, for which we need to know the drift velocity and the time difference between the trigger and the arrival time. The amplitude of the signal is proportional to the amount of produced charge, thus we can obtain the deposited energy from the signal recorded on the anodes.

Preliminary studies regarding the spatial and energy resolution have been carried on for the previous prototype XEMIS1 [135]. A whole calibration study of the Compton camera was performed with a Sodium-22 (Na-22) source in order to characterize the properties of the prototype. From the DOI profile of the photoelectric 511-keV events in the detector, we obtained the longitudinal resolution as the result of the Gaussian fit on the peak, with a sigma of $100 \mu\text{m}$.

A study on the ionization signal in LXe was also carried on to obtain the energy resolution value, which is expected to be around 5 % for 511-keV photons in an electric field of 1 kV/cm. While the angular resolution evaluation obtained a value of 4° for an electric field of 0.75 kV/cm.

3.3 Proposed 3- γ image reconstruction technique

The principle of 3- γ image reconstruction is based on the use of the two coincidence photons to determine the LOR and on the detection of the third-gamma interactions to obtain a Compton cone to use for a better localization of the annihilation position on the line. The third photon is most likely to undergo Compton scattering in LXe due to the higher initial energy (1.157 MeV). The aim is to identify a Compton cone to delineate the direction from where the photon was emitted. In order to do so, information about the position and the energy of the first two interactions in LXe are needed. Once the cone is built, we intersect it with the LOR obtaining the LCI coordinates. This point can be used as the center of a Gaussian probability distribution function (PDF) that gives a non-constant probability of annihilation along the LOR in image reconstruction.

3.3.1 LOR/cone intersection

For an 1157-keV photon the probability of scattering in LXe is 79% in 12 cm of detection mean [1]. Due to this high probability, we can obtain a Compton cone for most of the recorded events. The Compton cone axis corresponds to the line connecting the first two detection points, **A** and **C** in Fig. 3.6, and through the Klein-Nishina's Compton scattering formula in Eq. (1.13), knowing the energy before the interaction E_0 and the deposited energy E_1 , we can compute the cone aperture angle θ_C as:

$$\cos \theta_C = 1 - mc^2 \frac{E_1}{E_0(E_0 - E_1)}. \quad (3.1)$$

To identify the LCI point(s), results of the intersection of the LOR and the Compton cone, we compute the system in Eq. (3.2) considering an infinite line and cone as in Fig. 3.5 [146]:

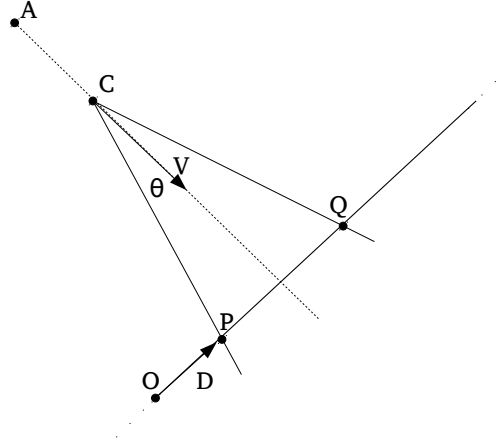


FIGURE 3.5: Vectorial diagram of the cone/LOR intersection: C and A are respectively the first and second third-gamma interaction point, $\theta = \theta_C$ is the scattering angle, the vector D represents the LOR direction and the points P and Q the two intersections between the cone and the infinite line.

$$\begin{cases} \mathbf{P} = \mathbf{O} + t\mathbf{D} \\ \frac{\mathbf{P}-\mathbf{C}}{\|\mathbf{P}-\mathbf{C}\|} \cdot \mathbf{V} = \cos \theta_C. \end{cases} \quad (3.2)$$

in which C and A are respectively the third-gamma first and second interaction point; D is the LOR vector, V is the cone normal vector and P and Q are the two LCI points. We can rewrite the system as:

$$\begin{cases} \mathbf{P} = \mathbf{O} + t\mathbf{D} \\ \frac{(\mathbf{P}-\mathbf{C} \cdot \mathbf{V})^2}{(\mathbf{P}-\mathbf{C}) \cdot (\mathbf{P}-\mathbf{C})} = \cos^2 \theta_C, \end{cases} \quad (3.3)$$

$$\begin{cases} \mathbf{P} = \mathbf{O} + t\mathbf{D} \\ (\mathbf{P} - \mathbf{C} \cdot \mathbf{V})^2 - (\mathbf{P} - \mathbf{C}) \cdot (\mathbf{P} - \mathbf{C}) \cos^2 \theta_C = 0, \end{cases} \quad (3.4)$$

Replacing $\mathbf{P} = \mathbf{O} + t\mathbf{D}$ we get a quadratic function:

$$t^2((\mathbf{D} \cdot \mathbf{V})^2 - \cos^2 \theta_C) + 2t((\mathbf{D} \cdot \mathbf{V})(\mathbf{C}\mathbf{O} \cdot \mathbf{V}) - \mathbf{D} \cdot \mathbf{C}\mathbf{O} \cos^2 \theta_C) + (\mathbf{C}\mathbf{O} \cdot \mathbf{V})^2 - \mathbf{C}\mathbf{O} \cdot \mathbf{C}\mathbf{O} \cos^2 \theta_C = 0, \quad (3.5)$$

We can easily solve it, if we write it in the form $at^2 + bt + c = 0$:

$$\begin{cases} a = (\mathbf{D} \cdot \mathbf{V})^2 - \cos^2 \theta_C \\ b = 2((\mathbf{D} \cdot \mathbf{V})(\mathbf{CO} \cdot \mathbf{V}) - \mathbf{D} \cdot \mathbf{CO} \cos^2 \theta_C) \\ c = (\mathbf{CO} \cdot \mathbf{V})^2 \\ -\mathbf{CO} \cdot \mathbf{CO} \cos^2 \theta_C. \end{cases} \quad (3.6)$$

To solve the system in Eq. (3.6) we must look at the determinant first:

$$\Delta = b^2 - 4ac \quad (3.7)$$

in order to discriminate if there are solutions and how many of them:

- if $\Delta < 0$, there is no intersection;
- if $\Delta > 0$ there is a unique intersection point;
- if $\Delta = 0$ there are two points of intersection.

The computation is carried on for infinite cone and line, thus we add the requirement that only solutions within the FOV are accepted. We also decided to discard all the events presenting a double intersection (2%), as well as events with no common point between LOR and cone (4%). These two types of event mostly occur due to Compton scattering before reaching the detector. As shown in Section 3.2.1, there are several metallic layers between the FOV and the LXe volume, that increase the probability of scattering before detection, which needs to be summed up with the already existing probability of scattering in the patient's body. This can lead to LCI miscalculation, either due to an error in the LOR or in the cone computation. In Fig. 3.6 we see how a small error on the Compton angle can derive in a much bigger uncertainty on the LOR.

In our case, where we deal with three photons, events with no scattering are rare and even small-angle deviations can be an issue in the intersection determination. In Fig. 3.7 we show only a part of the possible cases: (a) a true event, (b) a coincidence photon that undergoes scattering in the metallic layers around the FOV, and (c) a 1157-keV photon that scatters in the phantom. Other cases can be related to the scattering in the phantom for one, two or three photons at the same time, etc. All these situations can affect the LCI correct determination, and the uncertainty on the coordinates computation needs to be included in the width of the Gaussian PDF applied on the LOR during image reconstruction.

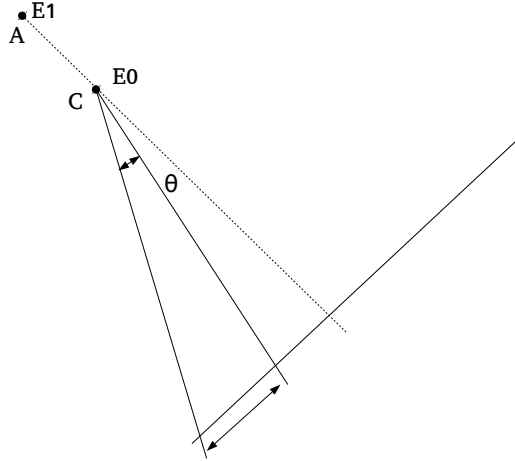


FIGURE 3.6: Scheme of the influence of the scattering angle's error on the LOR.

3.3.2 Requirements for 3- γ imaging

The main deal in 3- γ imaging is the use of the information carried by the third gamma to improve the image reconstruction. In order to do so, we need to determine a Compton cone and the crossing point between this object and the coincidence LOR. The precision on the LCI coordinates depends on several factors, among which the energy and spatial resolution of the third-gamma interactions, the distance between the first two detections and the distance LOR-cone vertex. In the next paragraphs we explore some of the factors that influence the LCI calculation and especially the angular resolution, which has the most influence on the cone.

Energy resolution

In Eq. (3.1) we wrote the Compton angle formula, using two variables corresponding to the transferred energy in the scattering E_1 , and the incident photon energy E_0 . We can also write the formula as:

$$\cos \theta_C = 1 + m_e c^2 \left(\frac{1}{E_0} - \frac{1}{E_1} \right) = 1 + m_e c^2 \left(\frac{1}{E_0 - E_e} \right). \quad (3.8)$$

where E_e is the energy transferred to the ejected electron.

Any error in the energy measurement can deeply affect the Compton angle value, if we consider E_0 as a known variable and we apply error propagation

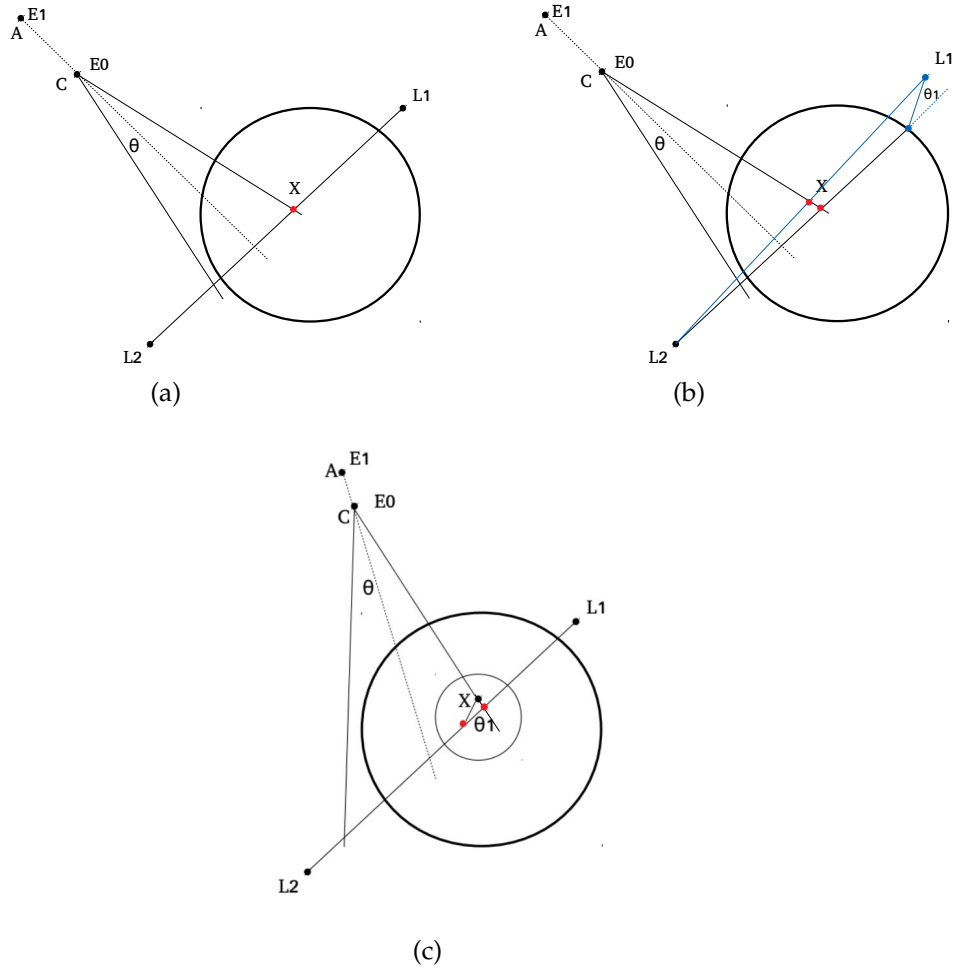


FIGURE 3.7: (a) Event with no scattering.
 (b) Event in which one coincidence photon scatters with a small angle before reaching the LXe, causing a change in the LCI coordinates.
 (c) Event with an 1157-keV gamma scatter in the phantom: depending on the angle width the cone can or not intersect the LOR, anyways the LCI determination is highly affected.

on the previous equation, we obtain:

$$\sigma_E^2 = \left(\frac{\partial \theta}{\partial E_e} \sigma_{E_e} \right)^2. \quad (3.9)$$

where σ_E^2 is the detector energy resolution, and through the error propagation formula applied on Eq. (3.8), we obtain:

$$\frac{\partial \theta}{\partial E_e} = \frac{1}{\sin \theta} \frac{m_e c^2}{(E_0 - E_e)^2}. \quad (3.10)$$

The detector energy resolution σ_E^2 depends on three factors:

$$\sigma_E^2 = \sigma_{\text{LXe}}^2 + \sigma_{\text{el}}^2 + \sigma_{\text{other}}^2. \quad (3.11)$$

σ_{LXe}^2 is the LXe intrinsic energy resolution due to the statistical fluctuations in the number of electron-ion pairs produced during the ionization process. The second factor σ_{el}^2 is related to the readout electronics noise, which is as low as $100 e^-$ for the XEMIS2's experimental setup [5]. The last term σ_{other}^2 comes from all the other contributions to the energy resolution degradation as inefficiency of the materials and so on.

Spatial resolution

To determine the importance of the spatial resolution in the cone angular resolution, we have to remember that the cone axis is defined by the line connecting the first and the second third-gamma interaction.

If the source is positioned in the origin and \mathbf{r}_1 and \mathbf{r}_2 are the vectors that identify the two third-gamma interactions (Fig. 3.8), we can write:

$$\cos \theta_C = \frac{(\mathbf{r}_2 - \mathbf{r}_1) \cdot (\mathbf{r}_1)}{\|\mathbf{r}_2 - \mathbf{r}_1\| \cdot \|\mathbf{r}_1\|}. \quad (3.12)$$

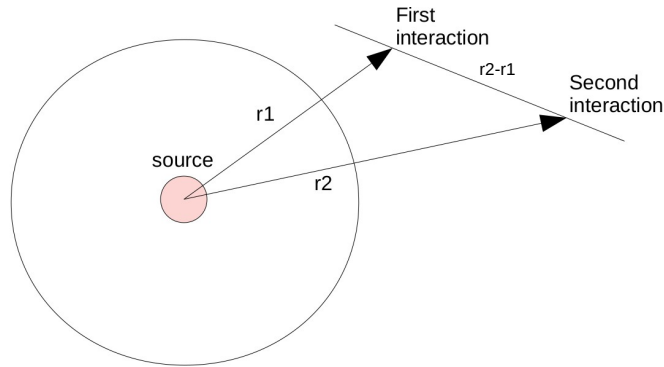


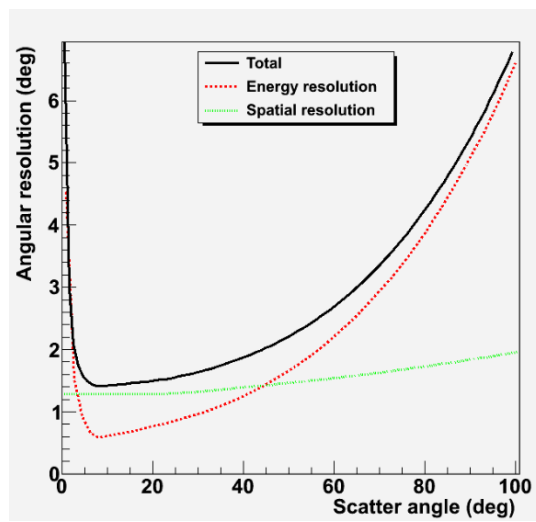
FIGURE 3.8: Scheme of the vectors involved in the spatial resolution calculation.

Thus the spatial resolution is proportional to the distance between the two interaction points. Applying the error propagation theory we obtain:

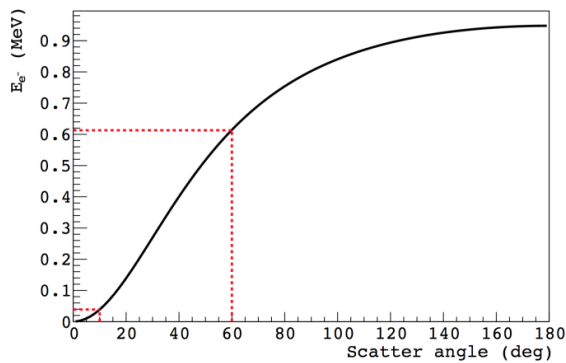
$$\sigma_s^2 = \sigma_{(x_1, y_1, z_1)}^2 + \sigma_{(x_2, y_2, z_2)}^2. \quad (3.13)$$

where $\sigma_{(x_1, y_1, z_1)}^2$ and $\sigma_{(x_2, y_2, z_2)}^2$ represent respectively the spatial resolution of the first and second interaction of the third gamma. These quantities depend on the PMTs' light collection efficiency and on the pixelated anode's dimensions. For every charge cloud reaching the anode, the detection position is recorded in the center of the pixel taken as the centroid of the distribution. The pixel size, $3.125 \times 3.125 \text{ mm}^2$ in XEMIS2, is determinant in the error on the spatial resolution both for the Compton cone and for the LOR coordinates.

Angular resolution



(a)



(b)

FIGURE 3.9: (a) Angular resolution as a function of the scatter angle, in red the energy resolution, in green the spatial resolution, in black the total resolution. (b) The recoil energy of the electron coming from Compton scattering as a function of the scatter angle. The red lines determine the energy interval in which we have an acceptable angular resolution [4].

We presented the energy and spatial resolution and now we show the angular resolution of the detector, which can be seen as a combination of the two.

In Fig. 3.9 we display the angular resolution for a LXe Compton camera [5, 4]. In (a) we show it as a function of the scatter angle: we can notice that the trend is mostly dominated by the energy resolution contribution, while the spatial resolution one is almost constant. In Fig. 3.9 (b) we have on the y -axis the energy transferred to the electron in a Compton interaction, and on the x -axis the scatter angle going from zero to 180° . The maximum transferred energy occurs when the photon is back-scattered, and the angular resolution degrades for high scatter angles. Not all scatter angles are appropriate for a valid Compton cone determination: only for angles between 10 and 60° (between 40 and 610 keV of deposited energy) we obtain an acceptable angle resolution.

3.3.3 Pseudo-TOF image reconstruction

The proposed 3- γ image reconstruction technique is based on the use of the isotropically emitted third photon to obtain clearer information about the annihilation localization on the LOR. This is achieved through the intersection of the LOR and the third-gamma Compton cone, which helps to determine the direction from where the third gamma is coming, and to delineate a LCI point. Once we compute and obtain the LCI coordinates, we can use this information in a similar way to the time difference in TOF-PET, to modify the way the PDF is distributed on the LOR.

In conventional PET image reconstruction, the probability distribution is constant along the LOR, while in TOF-PET it depends on the detector and event's characteristics and it is applied as a Gaussian distribution on the coincidence line. The center of the PDF is the length-equivalent of the time difference between the arrival of the two coincidence photons, computed following $s = c \cdot \Delta t$, and the FWHM is related to the time resolution of the detector.

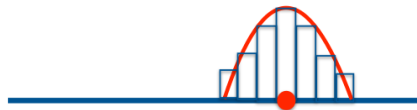
In 3- γ image reconstruction we proceed in a similar way as for TOF-PET reconstruction, hence we refer to the proposed technique as *pseudo-TOF*. Although, in this case, the Gaussian PDF used for the annihilation probability is centered on the LCI coordinates and the standard deviation depends on the uncertainty of the LCI calculation (see Fig. 3.10).

Classical PET reconstruction



(a)

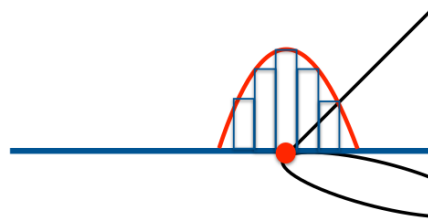
TOF-PET reconstruction



$$t_l = \frac{\Delta t * c}{2}$$

(b)

Pseudo-TOF approach



(c)

FIGURE 3.10: Probability on the LOR for different image reconstruction techniques: (a) classical PET with a uniform probability, (b) TOF-PET with a Gaussian distribution in which the FWHM is due to the time resolution and (c) pseudo-TOF with a Gaussian distribution centered on the LCI coordinates.

As already discussed in the section about 3- γ imaging requirements 3.3.2, the LCI can be affected by several effects: photon undergoing Compton scattering in the phantom, positron range [147], detector energy and spatial resolution [148], distance between the interactions, angle between cone and LOR, etc. Thus, we ought to introduce a reconstruction parameter called pseudo-TOF standard deviation that characterizes the LCI uncertainty and represents the PDF standard deviation, including all the possible effects.

In order to measure the impact of all the bias-carrying effects on the LCI, we studied the distance d between the computed LCI and the projection on the LOR of the third-gamma emission point (Fig. 3.11) through a similar-NEMA phantom simulation.

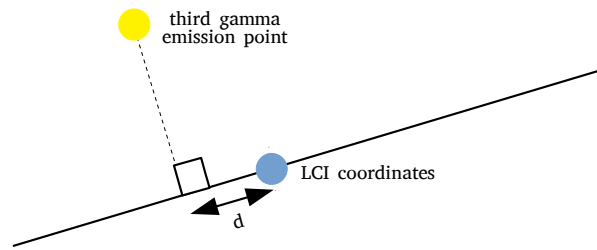


FIGURE 3.11: LCI coordinates' uncertainty scheme: d is the distance between the projection of the third-gamma emission point on the LOR and the LCI coordinates computed through the geometrical intersection.

Fig. 3.12 shows the resulting distribution: the obtained curve is wide and shows a maximum on 0, thus we decided to use as reference value the root mean square (RMS), 22 mm, that translates to 70 ps in TOF units.

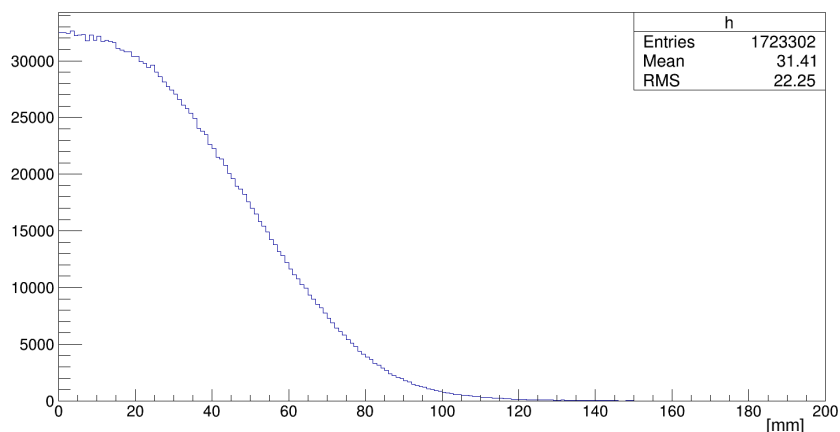


FIGURE 3.12: Study on the LCI coordinates' uncertainty on a NEMA-like phantom: in the histograms the distance between the computed LCI coordinates and the projection of the third-gamma emission point on the LOR.

The use of a fixed pseudo-TOF standard deviation in the reconstruction underestimates the uncertainty for a part of the events, thus two different image reconstructions were carried. We used the 70-ps resolution value resulting from the NEMA-distance study and a variant pseudo-TOF resolution, which was calculated event by event as the time-equivalent of the distance d in ps. By incorporating the LCI into a PET system and accounting for the relative uncertainty, we expect improvement in the reconstructed images, especially since TOF scanners have already demonstrated SNR and CNR enhancement over conventional PET systems [149, 150, 151].

3.4 Simulation

The XEMIS2 system was simulated using GATE [152], which is an open-source software for Monte Carlo simulations of personalized medical systems and it is mostly used to test new designs and geometries, to optimize and experiment new methods and new data acquisition techniques.

In GATE the detector geometry is defined as a multi-layer cylinder: the active zone measures 240 mm of length and respectively 70 and 190 mm of inner and outer radius. The cylinder is filled with LXe and the FOV with air. The active volume is enclosed in a double-layer cylindrical armor of stainless steel and aluminum. The only discontinuity in the detector active zone is due to the central copper cathode that divides the two TPCs. In Fig. 3.13 an overview of the detector geometry taken from the GATE visualization tool.

Particles and matter were simulated using GEometry ANd Tracking (Geant4), particle generation based on CLHEP libraries [153], while photon interaction follows the Penelope model in GATE [154].

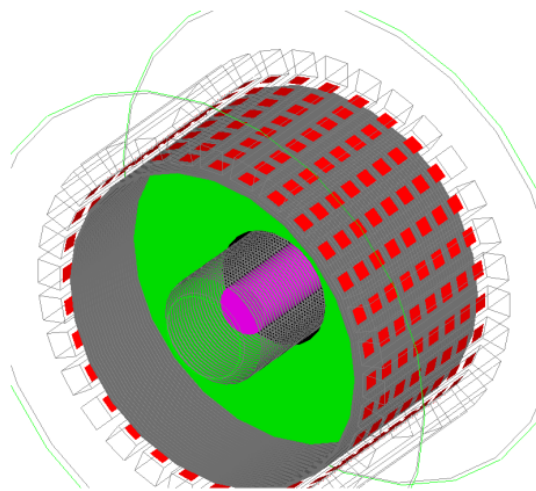


FIGURE 3.13: Overview of the XEMIS2 simulated as a multi-layer cylinder in GATE. We can see the phantom in pink, the LXe in green and the PMTs around the active volume in red.

For every simulated event we obtain a chain of interactions to follow in order to acquire the required information about $3\text{-}\gamma$. The radioisotope Sc-44 decays into $\text{Ca}^*\text{-44}$ with a positron emission. The positron travels in the body until it annihilates with an electron in the surroundings, and two colinear 511-keV gammas are produced. Almost at the same time $\text{Ca}^*\text{-44}$ emits an energetic gamma (1.157 MeV) to reach the Calcium-44 (Ca-44)'s ground state. The

Radius [mm]	Position (X,Y,Z) [mm]
2	(0.0, 17.5, 0.0)
4	(-8.8, 15.1, 0.0)
8	(-17.5, 0.0, 0.0)
10	(0.0, -17.5, 0.0)
12	(17.2, 3.7, 0.0)

TABLE 3.1: Dimensions and coordinates of the five hot spheres in the phantom, the origin being the center of the scanner.

third gamma is emitted isotropically and independently of the coincidence photons' direction. Although more particles and interactions are involved in the event, we decided to consider only the detections directly related to the 3- γ . Scattering is allowed in the phantom and in the detector. For each interaction we record position and deposited energy.

Data acquisition time is 20 minutes and the initial total activity 20 kBq. The events are acquired in LM to associate an event-based pseudo-TOF standard deviation.

3.4.1 Phantoms

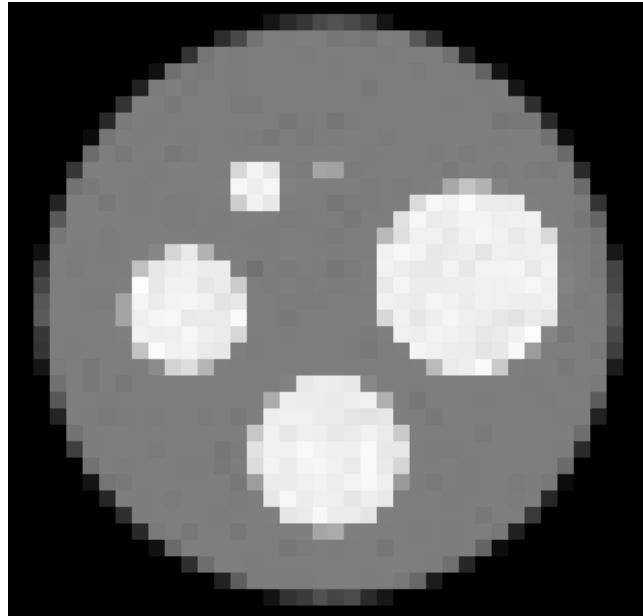


FIGURE 3.14: Axial view of the central slice of the NEMA-like phantom showing the five hot spheres of 2, 4, 8, 10, and 12-mm radius.

In this work we explore the pseudo-TOF image reconstruction method and its benefits and we compare the proposed reconstruction technique to

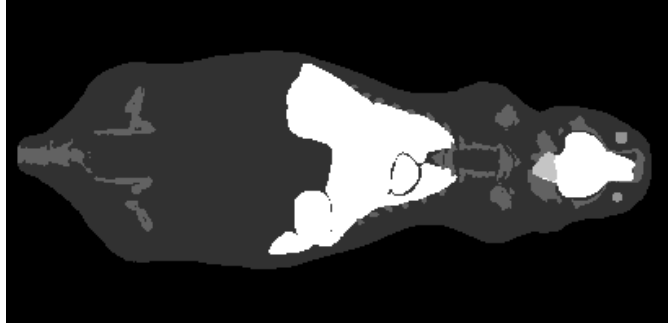


FIGURE 3.15: Axial view of the central slice of the Digimouse phantom showing some of the internal structures.

Organ	activity/voxel [Bq/0.5 mm ³]	Organ	activity/voxel [Bq/0.5 mm ³]
Skin	0.1	Testes	0.1
Spinebone	1.7	Stomach	0.1
Eye	0.1	Spleen	3.2
Brain	0.1	Pancreas	0.1
Muscle	0.1	Liver	1.5
Bladder	2.25	Kidney	0.7
Lung	0.1	Tumor (brain)	2.25

TABLE 3.2: Radiopharmaceutical uptake distribution for the mouse phantom with $0.8 \times 0.8 \times 0.8$ -mm³ voxels: [⁴⁴Sc]Sc-J591 uptake values in the Digimouse computed from the data in Holland, 2010 [3].

conventional two-gamma (2- γ) image reconstruction. Considering this, the first simulated phantom is a NEMA-like phantom, in analogy to the image-quality studies carried out to characterize detectors, and in general in TOF versus non-TOF comparisons [155].

The phantom consists of a 12-cm-long homogeneous water cylinder of 3.5 cm radius, containing five spheres. All spheres' centers are equidistant from the cylinder central axis and positioned on the central slice of the cylinder. The radius of the spheres measure 2, 4, 8, 10, and 12 mm, see Fig. 3.14 and Table 3.1 for further details.

The total simulated activity in the phantom is 20 kBq, with a factor 15 of contrast ratio between the sphere and the background. 30 duplicates were simulated to study the image variance.

To complete the XEMIS2 characterization, as second phantom we chose to simulate a more realistic object: a 28-g male mouse known as the Digimouse [156, 157]. The small animal presents a complete structure, composed of brain, muscles, eyes, glands, heart, lungs, liver, stomach, spleen, pancreas,

kidneys, testes, bladder, skeleton, and skin. A 2-mm radius spherical tumor was added in the brain as the region of interest (ROI) to analyze in the image quality study. In Fig. 3.15 a transaxial view of the Digimouse central slice and in Table 3.2 the simulated uptake distribution of the mouse.

The radiopharmaceutical employed in this simulation is [^{44}Sc]Sc-J591, labeled with Sc-44, and it is an anti-prostate-specific membrane antigen monoclonal antibody, whose biological uptake is known from Carter [2] and Holland [3]'s studies. One of the advantages of using [^{44}Sc]Sc-J591 is that the molecule is also used for positron range studies since it is easily associated also to F-18.

The total activity simulated in the phantom was around 22 kBq and data acquisition time was 20 minutes. Due to the more detailed GATE-voxelized structure of the Digimouse phantom, longer computation time was needed and only one acquisition was simulated.

3.5 Image reconstruction software

3.5.1 Pseudo-TOF system matrix

Before getting into the details on the software implementation of 3- γ image reconstruction, let us introduce the SM for pseudo-TOF. SM elements are often computed event-by-event, despite it being computationally intensive due to the matrix size. They depend on the physics and on the system, and they are characteristics of each detector and each data acquisition, thus they need to be computed for each event.

In TOF-PET the SM gives the probability $p_{i,j,b}$ that the annihilation of a positron emitted in the j -th voxel is detected in the i -th LOR's bin and in the time bin b , with $i \in [1, \dots, M]$ (M number of possible LORs), $j \in [1, \dots, J]$ (J number of voxels), and $b \in [1, \dots, B]$ (B number of possible time bins on the LOR). In the TOF case, the SM elements make use of a Gaussian function to weight the LOR length component, whose FWHM depends on the time resolution.

In the pseudo-TOF context, we deal with position and distance instead of time resolution, thus b cannot be considered the number of possible time bins. We translate it in the number of possible pseudo-time bins, each of them representing a different LCI position on the LOR i . Consequently, the coefficient $p_{i,j,b}$ becomes the probability that an annihilation that occurred in

the j -th voxel was detected on the i -th LOR and that the third gamma was emitted from the pseudo-time bin b on the LOR. In absence of scattering and attenuation, this probability depends on the detector sensitivity, on the spatial and energy resolution, and on the Sc-44 positron range. To calculate the SM elements in pseudo-TOF, we can follow the same TOF method and use the pseudo-TOF resolution instead.

3.5.2 Pseudo-TOF algorithm in CASToR

All the images we reconstructed in this work are obtained through the LM-MLEM reconstruction algorithm in CASToR v2.3 [158], both for pseudo-TOF and non-TOF events, which we refer to as 3- γ and 2- γ respectively.

As for all the iterative optimization algorithms as MLEM, the reconstruction in CASToR is based on a projector handling both back and forward projection and there is an optimizer and a convolver, in case any kind of convolution is required (e.g. for positron range correction).

For each iteration, there are several steps to follow: first, the software calls the projector to compute one row of the SM. Then the optimizer, composed of both the objective function and the iterative optimization, performs the data update in several operations. It starts applying a forward projection on the image estimate, then it adds all the provided estimation of the background, and in the end it computes the correction term in the data space, in order to back-project them and obtain a correction image for the considered SM row.

In CASToR the computation of the system matrix elements follows the Siddon projector [159, 160] and the so called *ray-tracer method*, for which the probability depends on the portion of LOR crossing each voxel. The standard optimizer used for two-gamma events is from Shepp and Vardi [18]; while for the LM-MLEM TOF algorithm we refer to Filipovic [161].

The pseudo-TOF LM-MLEM algorithm can be expressed as:

$$\lambda_j^{(k+1)} = \frac{\lambda_j^{(k)}}{\sum_{i,b} p_{i,j,b}} \sum_i \frac{p_{i,j,b}}{\sum_{j'} p_{i,j',b} \lambda_{j'}^{(k)}}. \quad (3.14)$$

where i refers to the LOR bin and b to the pseudo-time bin corresponding to the considered event; $\lambda_j^{(k)}$ is the image value in the voxel j for the k -th estimation. We denote as pseudo-time bin the time bin corresponding to the LCI-position equivalent in ps.

3.5.3 XEMIS2 geometry in CASToR

The first information required by CASToR to start the image reconstruction process is the detector geometry. Normally, through the use of a tool provided with the package, we are able to directly transfer the GATE geometry into a CASToR geometry file. The software needs the number of modules, sectors and crystal elements to rebuild the coincidences and identify them with its own notation (CASToR-ID), in order to recognize the events in its system of reference.

This functioning cannot be applied in a monolithic detector case, due to the absence of detector elements. In this case, we need to produce a geometry file in which the detector is discretized in smaller elements, with dimensions comparable to the spatial resolution of the system to not lose information (Fig. 3.16).

In our case, we chose to discretize with 1-mm^3 virtual elements, which brought us to a total of more than 23 millions elements due to the large size of the XEMIS2 active volume, that was not acceptable in terms of computational time to process.

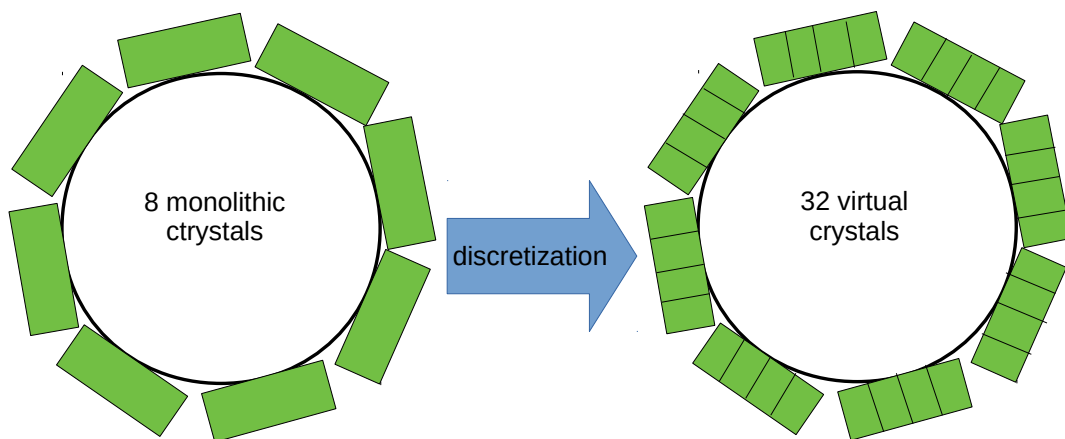


FIGURE 3.16: Virtual elements discretization of a monolithic detector: from 8 detector blocks to 32 virtual elements.

The solution to this matter was the discretization of only a thin layer of the active zone around the FOV, as shown in Fig. 3.17 (b). We considered a 0.5-mm-deep layer of elements all along the FOV cylinder for a total amount of 421920 virtual elements: 480 elements for each axial plane and 879 transaxial

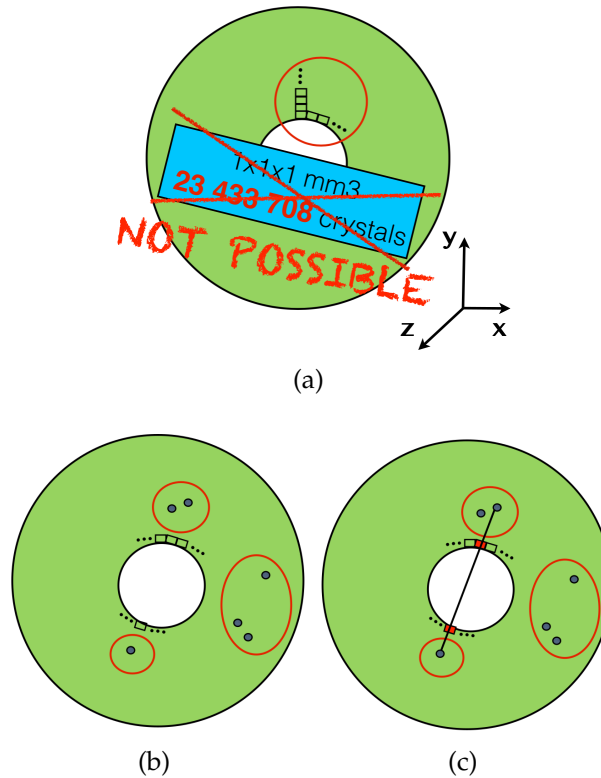


FIGURE 3.17: (a) Discretization of the XEMIS2 considering the total active volume, we obtain 234337008 virtual elements, a number too high to be treated by any software in a reasonable amount of time.

(b) Discretization of the XEMIS2 considering only the first layer around the FOV. In (c) we show how the events are registered: the LOR length considered in CASToR is the length between the two red elements, whose element ID is used during reconstruction to get the event LOR position.

elements. In this instance, the total virtual elements' number is perfectly reasonable.

To identify the couple of elements involved in the event, we added an intermediate step between data acquisition and image reconstruction, in which we transfer the coordinates of the detected interactions on coordinates that lay on the discretized part of the detector. We intersect the event LOR with the FOV cylinder and once the couple of virtual elements are pointed out by the intersection (red elements in Fig. 3.17 (c)), we pass their ID over to CASToR to store it and subsequently use it during reconstruction. Another information needed for each event is the LOR length and the LCI position to be translated in time-units (ps).

Sensitivity image

When reconstructing in CASToR, the sensitivity image can be given as an input image file before launching the reconstruction or, if the file is missing, it is computed by the software before starting the iterations. CASToR computes the sensitivity map running a loop over all possible LORs, considering all the couples of elements in the detector geometry. In this way the sensitivity image depends only on the geometrical characteristics of the detector, attenuation and normalization are not taken into account.

In our case, due to the fact that we modified the XEMIS2 geometry discretizing the detector, and we removed the concept of depth, we provided one of our own. We obtained it simulating a homogeneous water cylinder filled with Sc-44, as large as the FOV. The hours-long simulation brought us to collect millions of events. We then reconstructed the events through an MLEM sensitivity optimizer algorithm and used the first iteration output image as our sensitivity map.

In this case, since the cylinder was filled with water and scattering was allowed in the phantom, we can consider that the scattering and attenuation effects in water are included in the image.

Chapter 4

Results

Summary

In this chapter we present the results obtained in this work regarding image reconstruction with XEMIS2. First, we introduce the figures of merit employed in the image analysis and we then show the results for the two simulated phantoms. We compare 3- γ images to images obtained through conventional PET reconstruction for both phantoms in XEMIS2. We show the reconstructed images, ROIs's plot profiles, CNR, SNR and recovery coefficient (RC) trends, and we briefly discuss the obtained results.

Contents

4.1 Introduction	87
4.2 Figures of merit	88
4.2.1 NEMA-like phantom analysis	88
4.2.2 Digimouse phantom analysis	89
4.3 NEMA-like phantom results	90
4.4 Digimouse phantom results	91
4.5 Discussion	95

4.1 Introduction

In this chapter we discuss the results obtained for image reconstruction with the XEMIS2. We hold a comparison between 2- γ and 3- γ reconstructed images in order to assess the benefits of the pseudo-TOF technique over conventional PET reconstruction.

4.2 Figures of merit

The image quality metrics studied in this work mainly relate to signal and contrast measurements (SNR, CNR and RC). In the following we use label with *b* and *s* subscript to indicate variables related respectively to the *background* and to the *ROI*. Due to the low statistics-induced noise in the images, a Gaussian smoothing filter ($\sigma = 1$) was applied on all the reconstructed images before computing the metrics.

4.2.1 NEMA-like phantom analysis

In the NEMA phantom analysis parameters were computed throughout all the iterations for every noise replicate and the variance was calculated as follows:

$$\sigma_c^2 = \frac{1}{|R_c|} \sum_{j \in R_c} \left(\frac{1}{L} \sum_{\ell=1}^L (x_j^\ell - \mu_j^c)^2 \right), \quad (4.1)$$

where:

$$\mu_c = \frac{1}{30|R_c|} \sum_{\ell=1}^L x_c^\ell. \quad (4.2)$$

$c \in \{b, s\}$ is the label for the background cylinder and for the hot spot, and x_c^ℓ is the reconstructed activity from the ℓ^{th} simulation; a total of $L = 30$ repetitions were performed. The variance was used to study the trend of the image quality parameters with respect to the general noise.

The first studied parameter is the SNR, determined as the difference of activity between the sphere and the background, divided by the standard deviation in the cylinder σ_b :

$$\text{SNR} = \frac{\mu_s - \mu_b}{\sigma_b}, \quad (4.3)$$

where the variables were calculated following equations (4.1) and (4.2).

For the contrast analysis we computed CNR and RC: the first as the absolute difference between the mean value in the sphere and in the cylinder, divided by the sum of the two standard deviations:

$$\text{CNR} = \frac{|\mu_s - \mu_b|}{\sqrt{\sigma_b^2 + \sigma_s^2}}, \quad (4.4)$$

while the RC was defined as the fraction of the difference between the mean value in the sphere and in the cylinder for the reconstructed images over the same quantity related to the ground truth (GT) image:

$$\text{RC} = \frac{\mu_s - \mu_b}{\mu_s^{\text{GT}} - \mu_b^{\text{GT}}}. \quad (4.5)$$

To obtain a GT image for each repetition, we mapped back to an image all the annihilation positions from the GATE simulation.

4.2.2 Digimouse phantom analysis

For the Digimouse phantom simulation, we worked only on one data acquisition, thus the figures of merit differ from the previous analysis.

We consider the added sphere in the brain as the volume of interest (VOI), with μ_s and σ_s being respectively the mean value and the standard deviation in the hot spot. In this case the computation of the respective background variables is more complex due to the non-homogeneous background. We delineated 4 spheres positioned in the low-activity part of the phantom that we can consider uniform, as shown in Fig 4.1. We computed SNR and CNR as for the NEMA-like phantom, where the background variables are averaged on the 4 spherical volumes. The formulas become:

$$\text{SNR}_{\text{digimouse}} = \frac{\mu_s - \mu_b}{\sigma_b}, \quad (4.6)$$

$$\text{CNR}_{\text{digimouse}} = \frac{|\mu_s - \mu_b|}{\sqrt{\sigma_b^2 + \sigma_s^2}}. \quad (4.7)$$

where:

$$\mu_b = \frac{1}{M} \sum_{i=1}^M \mu_i, \quad (4.8)$$

and

$$\sigma_b = \frac{1}{M} \sum_{i=1}^M \sigma_i. \quad (4.9)$$

in which $M = 4$ are the four background spheres in the Digimouse.

For implementation reasons, the simulation of a GATE voxelized phantom did not allow direct information about the local interactions in the mouse, and

we did not reconstruct a GT image starting from the annihilation positions. As a consequence, no RC study was carried out in this case.

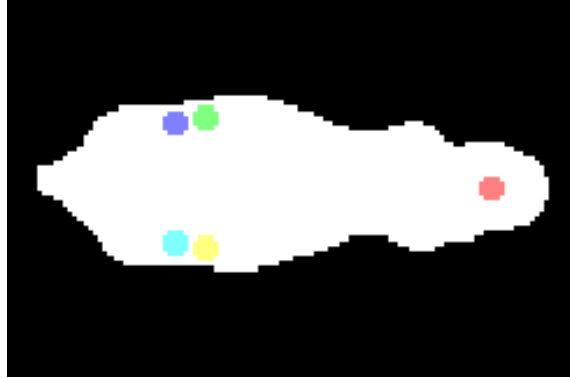


FIGURE 4.1: Transaxial section of the Digimouse phantom mask to show the VOI (red sphere) and the 4 background (green, purple, blue and yellow).

4.3 NEMA-like phantom results

In this section we show results related to the NEMA-like phantom obtained through $3\text{-}\gamma$ and $2\text{-}\gamma$ MLEM reconstruction. For the pseudo-TOF reconstruction, we used two different pseudo-TOF approaches: in one reconstruction we used a fixed Gaussian standard deviation of 70 ps, which is the value corresponding to the average uncertainty on the LCI calculation. In the second approach the resolution was event-based, hence variable, computed for each event as the time-equivalent of the difference between the LCI and the annihilation point projection on the LOR, as shown in Fig. 3.12.

The reason for showing results with the average pseudo-time resolution and with the variable resolution is to study the potential benefits of the proposed approach in favorable and less favorable scenarios of reconstructed cone accuracy.

Fig. 4.2 shows the axial view of the phantom central slice on the last iteration for the three reconstruction methods: (a) $2\text{-}\gamma$, (b) 70-ps pseudo-TOF and (c) pseudo-TOF variant resolution reconstruction, and the relative plot profiles along the yellow line in (d) and (e) vs (f).

Fig. 4.3 shows the same view of Fig. 4.2 after applying a Gaussian filter of scale $\sigma = 1$ to reduce noise induced by low statistics.

The metrics in Fig. 4.4 were calculated following the equations in section 4.2, normalizing the values inside the cylinder. We show the SNR, CNR

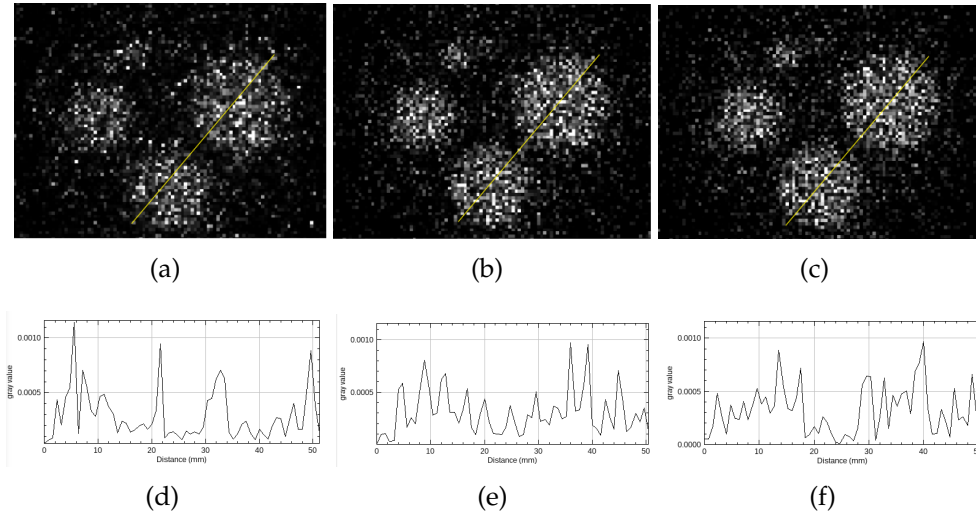


FIGURE 4.2: Transversal view of the central slice of the NEMA-like phantom at the 30th iteration and plot profiles along the yellow line crossing two spheres. We show results for (a, d) conventional 2- γ reconstruction, (b, e) proposed pseudo-TOF approach with a Gaussian standard deviation of 70 ps and (c, f) with an event-by-event variant pseudo-TOF resolution.

and RC for each of the five spheres. The SNR and CNR are expressed as a function of the iteration number, while the RC is presented as a function of the variance.

Tables 4.1 and 4.2 show several quantitative results on the SNR and CNR, in particular the percentage gain for pseudo-TOF with different resolutions and with 70-ps resolution over conventional 2- γ reconstruction. The values refer to the 30th iteration and were calculated from the following equations:

$$\%gain = 100 - \frac{SNR_{NOTOF} \times 100}{SNR_{TOF}}, \quad (4.10)$$

$$\%gain = 100 - \frac{CNR_{NOTOF} \times 100}{CNR_{TOF}}. \quad (4.11)$$

4.4 Digimouse phantom results

First difference between the NEMA-like and the Digimouse study is that in the second case images were obtained only through conventional 2- γ reconstruction and pseudo-TOF reconstruction with several resolution values (70 ps, 100 ps, 150 ps, and 200 ps). Moreover, in this case events with and

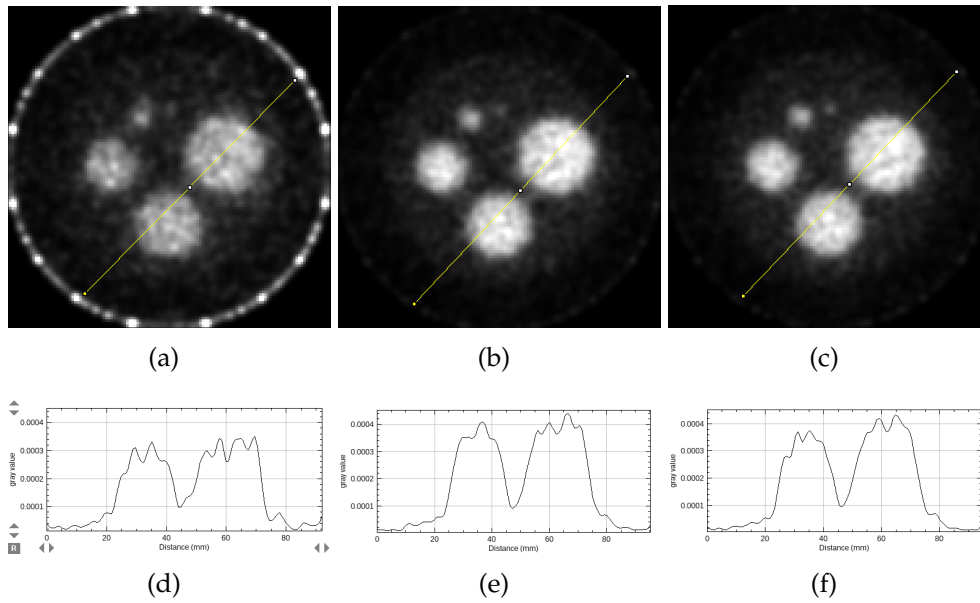


FIGURE 4.3: Axial view of the NEMA phantom after Gaussian filtering ($\sigma = 1$ mm) using (a) classical PET reconstruction and the proposed 3- γ technique with (b) 70-ps and (c) variant standard deviation. Images are the results of the 30th iteration. In (d), (e) and (f) the corresponding plot profiles along the yellow line. The high contrast ring around the FOV in the first image on the left is due to a CASToR misinterpretation of the activity value on the FOV edge and it does not affect image reconstruction.

Radius mm	SNR % gain 70 ps	SNR % gain variant resolution
2	40.9	43.5
4	33.7	32.9
8	30.1	28.4
10	29.2	28.0
12	28.7	27.6

TABLE 4.1: Percentage gain in SNR for pseudo-TOF over non-TOF for all spheres, computed on the last iteration.

Radius mm	CNR % gain 70 ps	CNR % gain variant resolution
2	43.1	46.0
4	34.1	33.3
8	30.1	28.4
10	29.3	28.0
12	28.8	27.6

TABLE 4.2: Percentage gain in CNR for pseudo-TOF over non-TOF for all spheres, computed on the last iteration.

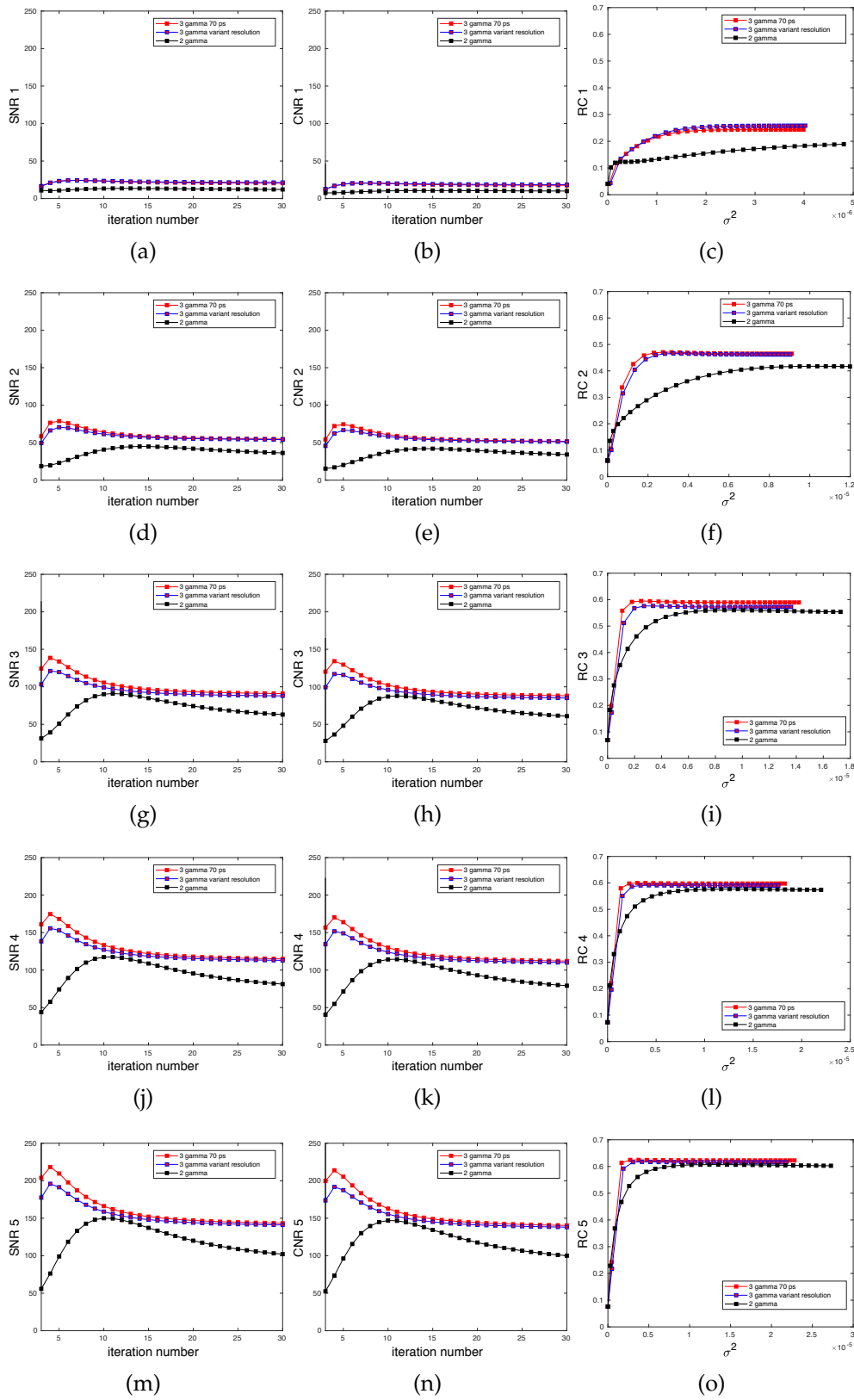


FIGURE 4.4: Sphere-by-sphere metrics results, from top to bottom the (1) 2-mm, (2) 4-mm, (3) 8-mm, (4) 10-mm, and (5) 12-mm radius sphere with the respective values of SNR, CNR and RC.

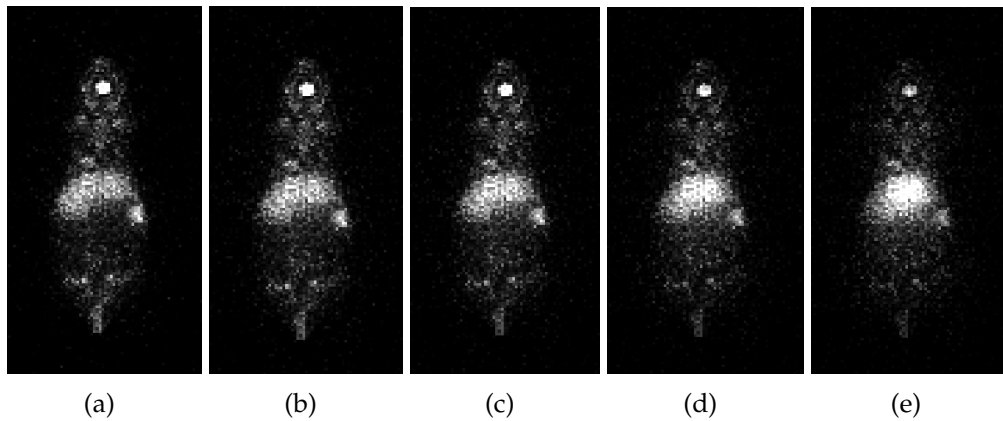


FIGURE 4.5: Reconstructed images of the Digimouse, from left to right: 2- γ reconstruction, pseudo-TOF with 200-ps, 150-ps, 100-ps, and 70-ps resolution.

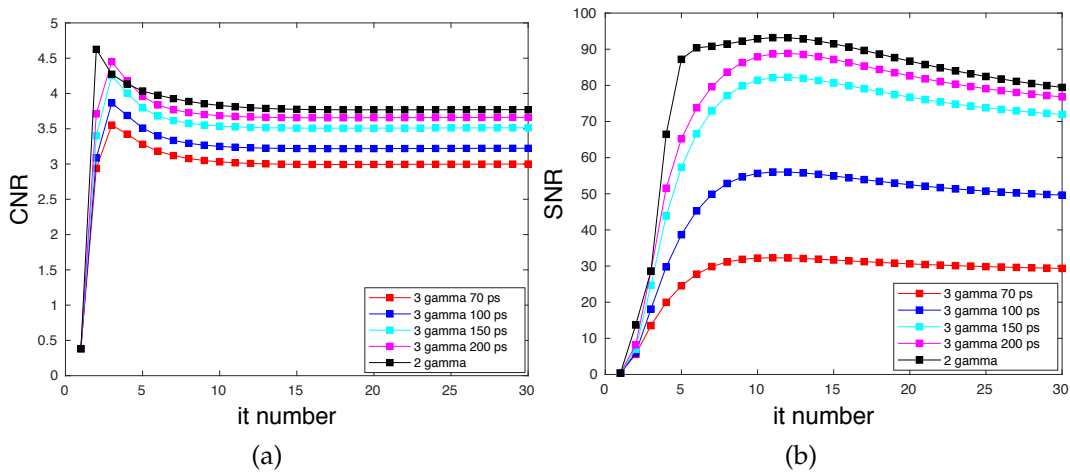


FIGURE 4.6: Metrics results of the Digimouse reconstruction

without LCI point were both used for image reconstruction, due to the low amount of 3- γ events in the acquisition.

The reconstructed images are shown in Fig. 4.5: we see the central slice of the Digimouse on the 30th and last iteration for 2- γ and for all the employed pseudo-TOF resolution values. From left to right: 2- γ reconstruction, pseudo-TOF with a resolution of 200 ps, 150 ps, 100 ps and 70 ps. The metrics plots are shown in Fig. 4.6 for SNR and CNR as a function of the iteration number. We also computed the profile along the ROI in the Digimouse's brain, which can be seen in Fig. 4.7 for all the different reconstructions.

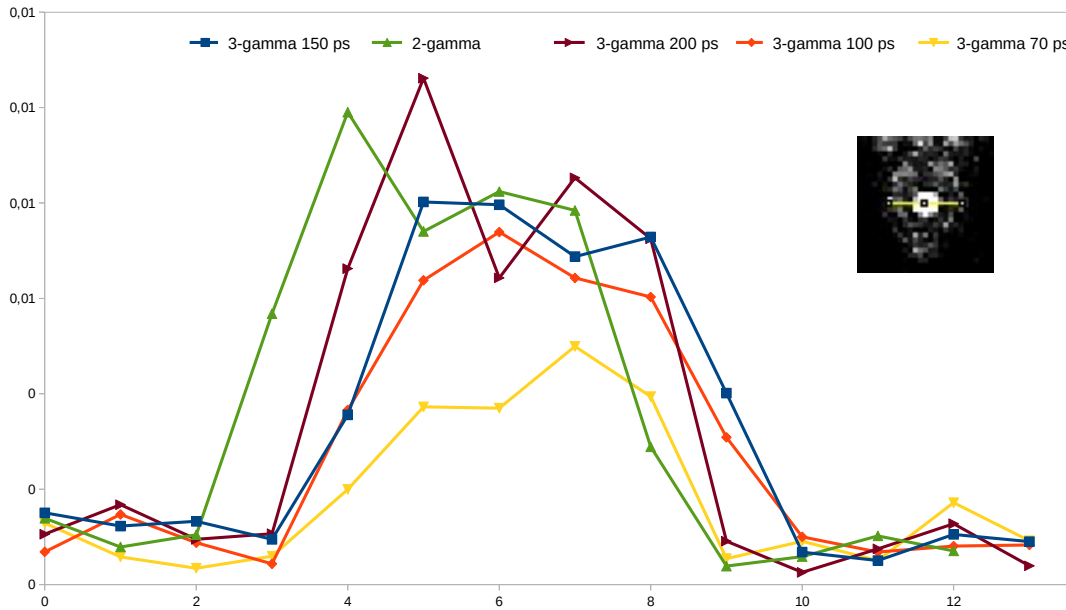


FIGURE 4.7: Line profile plot of the mouse's head's hot spot for all the different reconstructions on the last iteration.

4.5 Discussion

In the previous section 4.3 and 4.4 we presented the results for both phantoms using 3- γ and 2- γ image reconstruction algorithms, that we are going to discuss in this section.

We can observe the NEMA-like phantom images in Fig. 4.2, and we can notice that the smaller ROI is not easily distinguishable in the 2- γ reconstruction (a), and due to this visible flaw in the image, we do not consider the results regarding the first sphere to be particularly reliable. For all the other ROIs a contrast improvement is visible in the 3- γ cases, enhanced by the plot profiles (e) and (f) vs (d), where the lower values indicate less reconstructed activity in the hot spots. Looking at the reconstructed images after filtering (Fig. 4.3) we can appreciate even more the contrast enhancement in the 3- γ case (b) and (c), quantitatively visible in the profiles (e) and (f) versus (d) 2- γ .

One of the main amelioration brought by the XEMIS2 geometry can be noticed observing the axial view of the NEMA phantom. All five spheres appear perfectly round and in the exact position they are expected to be, with no distortion. Despite the depth of the detector (12 cm), no DOI correction was applied, since the XEMIS2 technology is able to detect the three-coordinate position of interaction, which is the main advantage of our monolithic detector.

Another quantitative analysis of the amelioration brought by the technique

proposed in this work, can be found in the metrics plots, Fig. 4.4. The improvement is visible in the SNR, CNR and RC higher values, and it is mostly due to the technique's ability to narrow the decay's position on the LOR and to focus on the right ROIs [162, 163]. While we know that for conventional PET reconstruction the decay's probability is uniform on the LOR. The higher CNR and SNR, together with the fast convergence, are the main advantages of the proposed pseudo-TOF algorithm. The acceleration in the convergence rate can be seen observing the SNR, CNR and RC peak in the plots in Fig. 4.4. For all five spheres, we reach the maximum value earlier in the 3- γ reconstruction case than in conventional image reconstruction.

In Tables 4.1 and 4.2 we present some values related to the SNR and CNR percentage gain of 3- γ over 2- γ , both for variant and for 70-ps pseudo-TOF resolution. The values related to the smallest sphere are surprisingly high, while in a TOF-like reconstruction we do not expect to gain in SNR or CNR for very little objects. It is most likely due to the fact that in the 2- γ case the sphere is confounded in the background, and again we do not consider these result well grounded. For the other spheres, we can notice how the proposed method shows an evident percentage gain, which spans between the 28% and 34% and that is dependent on the object's size. The best values refer to the 70-ps resolution reconstruction, supporting the choice of the RMS value in the distance distribution as pseudo-TOF resolution.

The results of the Digimouse phantom differ from those presented using the previous studied objects. The Digimouse phantom presents a complex internal geometry, made of small and detailed substructures, which are challenging to reconstruct in low count conditions. While the cylindrical NEMA phantom is simulated as a superposition of simple GATE objects, the small animal is defined voxel by voxel in GATE. Due to the Digimouse body and organs' dimensions, the voxel size was reduced to 0.8 mm^3 to avoid the reconstruction of artifacts in the images. Since the calculation of the pseudo-TOF resolution requires a geometrical intersection between the Compton cone and the LOR, the error on the LCI points is proportional to the distance between the cone center and the line. Any uncertainty on the cone determination, for example concerning the Compton angle miscalculation, is directly reported on the LCI coordinates as an error increasing with the distance between the LOR and the cone vertex. The Digimouse is a more complex phantom than the NEMA, with 16 different materials and small organs, which increase the

uncertainty in the LCI, due to Compton scattering in the phantom and to the positron range, which is increased in low-density materials. Furthermore, the lack of information about the interactions happening inside the Digimouse phantom, due to GATE simulation output for voxelized phantoms, led us to use pseudo-TOF resolution values that were not adapted to the simulated object, since the study on the distance between the third-gamma emission point and the LCI position on the LOR could not be carried out. Fig. 4.5 shows results for all the reconstructions tested: the pseudo-TOF resolution values chosen for the Digimouse reconstructions were taken from the NEMA phantom study going from the average to the maximum distance. They spanned from 70 ps (e) to 200 ps (b), which corresponds to a range from 22 to 60 mm of uncertainty on the LOR, typical state of the art TOF values for preclinical scanners.

In order to gain image quality on small animal's dimensions, we ought to work with very precise resolution. The 22-mm resolution on the LOR calculated for the NEMA phantom represents a sufficiently high value to show improvement over conventional PET reconstruction for a larger object. Lowering the resolution leads to an approximation of the 2- γ case, which can be seen in the Digimouse 3- γ image reconstruction with 200-ps of pseudo-TOF resolution, comparing Fig. 4.5 (a) and (b).

We did not observe the same improvement as for the NEMA-like analysis in the Digimouse study, neither visually nor quantitatively in the figures of merit 4.6. A higher statistics is needed for such a small and detailed phantom. As we fully complied with the regular amount of activity injected in a small animal as such [157], the only way to increment the statistics was to include the 2- γ events, that did not allow to evaluate the enhancement brought by the 3- γ technique. In the Digimouse case we faced a prohibitive low 3- γ statistics that required to include the 2- γ events reconstructed following conventional 2- γ MLEM. Contrarily, the NEMA case allowed for the reconstruction using only 3- γ events that enhanced the 3- γ reconstructed volumetric images both visually and quantitatively.

Chapter 5

Positron range correction

Summary

In Chapter 1 we already discussed the positron range problem and in Chapter 2 we presented the possible corrections or reduction of the phenomenon in PET imaging. We first introduce the state-of-the-art techniques to apply the correction in PET imaging, then we show the implementation of variant and invariant kernel convolution in CASToR framework. We get into the details of positron range correction applied to a NEMA phantom, that we reconstruct using a conventional 2- γ MLEM algorithm and also the proposed 3- γ method with Sc-44 as β^+ and γ emitter. At the end of the chapter we present the results, starting with the figures of merit employed in the image analysis and going through the comparison between 2- γ and 3- γ reconstruction with and without correction, for both variant and invariant kernel convolution.

Contents

5.1	Introduction	100
5.2	Positron range estimation	101
5.3	Positron range correction	103
5.3.1	Positron range reduction	103
5.3.2	Positron range correction pre-, post- and during reconstruction	103
5.4	Proposed correction	106
5.4.1	Simulation and phantoms	106
5.4.2	Reconstruction and positron range correction estimation	107

5.5 Results	109
5.5.1 Figures of Merit	109
5.5.2 Invariant and variant kernel convolution	110
5.6 Discussion	112

5.1 Introduction

There are several factors degrading image resolution in PET imaging: some are due to the detector's characteristics (sensitivity, scanner geometry, spatial and energy resolution), some depend on the physical interactions involved (positron range [164], Compton scattering, photon attenuation). For most of these effects correction methods have been studied in PET reconstruction, some of which are very successful (e.g. for attenuation calculation or for random coincidence).

In the positron range case, the modelization is often simplified: we consider a homogeneous medium or in most of cases, if the radio-pharmaceutical presents a submillimetric positron range, the correction is not even applied, as for F-18 imaging.

Reconstructing without correcting for the positron range means obtaining the positron annihilation distribution and not directly the positron emission distribution, which corresponds to the radio-pharmaceutical uptake in the body. As already introduced in Chapter 1, the positron range increases with the positron initial kinetic energy and decreases with the material density, thus it is an important effect in the case of energetic positrons in soft tissue. In Table 5.1 some common radionuclides with the corresponding estimation of positron range.

Isotope	Half-life [h]	E_{mean} [keV]	E_{max} [keV]	R_{mean} in water [mm]	R_{max} in water [mm]	Ref.
^{18}F	<2	250	635	0.5	2.3	[165]
^{64}Cu	12.7	216	653	0.6	2.9	[166]
^{89}Zr	78.4	403	902	1.3	4.2	[167]
^{45}Ti	3.08	442	1040	1.5	5.2	[168]
^{44}Sc	3.97	632	1474	2.4	6.9	[37, 169]
^{86}Y	14.7	640	3141	2.5	11.1	[170]

TABLE 5.1: Some positron range properties of common radioisotopes used in PET imaging.

5.2 Positron range estimation

The positron range estimation is the basis for the effect's correction. Two different approaches can be followed: an analytical modelization in which the range and other parameters are obtained through a Monte Carlo simulation, and a more experimental way based on actual measurements.

In particular positron range estimation's experiments were conducted starting in 1975 by Phelps [41], Cho [171], Derenzo (1986) [172] and Levin (1999) [38], while the interest in PET imaging was growing.

On this occasion, the words *range* and *path length* were defined: the range as the penetration depth and the path as the integral of the reciprocal of the stopping power, an approximation of the range.

In fact, since the positron undergoes several elastic and inelastic interactions while propagating in the medium, its path appears larger than its range, and due to this difference a correct estimation of the range was needed.

Early experiments were not completely successful since the resolution of the detector employed in the measurements was comparable to the positron range [173]. Derenzo experiments in 1979 [174] were centered on the measurement of the positron range in polyurethane foam and in aluminum. The idea is to remove the blurring caused by this effect through a deconvolution. The main problem with this approach is the loss of information in the deconvolution and the need for scaling the range to a water-equivalent material other than foam, since the range does not exclusively depend on the material density.

Later Palmer and Brownell [175] evaluated the positron range through an empirical formula based on β^+ energy spectra analysis. Studies on the reduction of positron range in presence of a magnetic field were carried on as well, with few results showing a slightly longer positron range in the direction of the field [176, 177, 178].

Due to the difficulties in correctly estimating the positron range analytically and empirically, there are more recent studies based on Monte Carlo simulations as for Harrison et al (1999) [179], Sanchez-Crespo (2004) [180], Champion et al (2006) [181], Alessio et al (2008) [182] and Lehnert et al (2011) [183]. The simulation of the positron range can be carried out using different frameworks and software: GATE [184] with its option *empenelope* allows accurate positron interactions, as well as PeneloPET [185] based on PENELOPE [186] and Geant4.

The simulation of a positron interacting in the matter is not a trivial problem: in fact, as we can see in Fig. 5.1, in the cross-section calculation we need to sum several types of interaction whose importance is energy-dependent [187, 188]. Scattering for a positron is considered as ionization if the energy loss is below 0.255 MeV, while it is referred to as Bhabha scattering (electron-positron diffusion) when the energy loss is higher.

One of the difficulties in simulating positron interactions is due to the amount of computation time needed to take into account every step. A positron tends to undergo scattering until it loses all its energy and is able to annihilate and the energy loss process is long and composed of very little steps. For each of them, we have a different energy loss, due to its energy dependence, thus a thick sampling would be needed to simulate a close approximation of the real interactions.

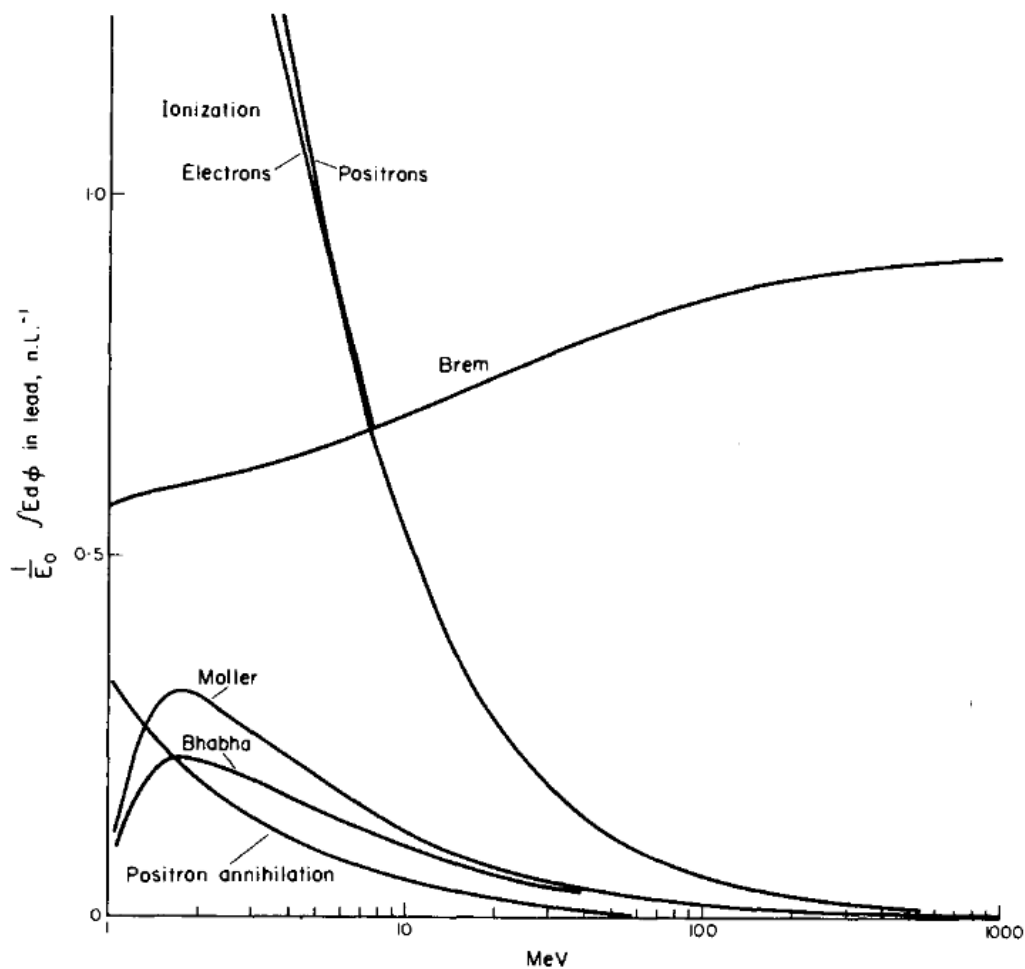


FIGURE 5.1: Fractional energy loss for positron and electrons in lead as a function of the particle energy [189].

5.3 Positron range correction

In this section, we take a look at the different approaches to deal with the positron range correction. There exist two main techniques to minimize the effect: the first is to reduce the particle range, while the second is to correct it working either on the projections, either on the reconstructed image, either on the estimated image iteration per iteration.

5.3.1 Positron range reduction

Positron are charged particle, subdued to the Lorentz force in presence of a magnetic field:

$$\mathbf{F} = q\mathbf{E} + q\mathbf{v} \times \mathbf{B}. \quad (5.1)$$

where \mathbf{F} is the Lorentz force experienced by the particle, q the particle charge, \mathbf{v} the particle velocity, \mathbf{E} the electric field and \mathbf{B} the magnetic field.

This force is applied perpendicularly to the magnetic field vector \mathbf{B} and to the velocity vector \mathbf{v} and it reaches its maximal intensity when the positron travels orthogonally to the magnetic field.

Several studies were carried out on the subject [176, 190, 191, 192, 193], showing that the particle range is enlarged and its direction changes to follow the Lorentz force as expected. Nevertheless, the magnetic field needs to be high to have a visible effect (> 3 T), which carries concerns on the cost, considering also that ferromagnetic materials cannot be employed in the construction of this type of PET system. In addition, the positron is affected only in one of the three directions, the one perpendicular to the magnetic field, ergo its range is reduced only in one of the three axis.

5.3.2 Positron range correction pre-, post- and during reconstruction

In order to apply positron range correction in distinct reconstruction steps (pre-, post- and during), we need to deal with different data types.

In the pre-reconstruction correction case, data acquisition ought to be in sinogram mode so that we can work on denoising the projections [172, 194].

Haber and Derenzo in 1990 [123], proposed a technique for which a Fourier deconvolution was applied on the projections to remove range blurring for ^{68}Ga and ^{82}Rb acquisitions. Since the point spread function (PSF) used in the

deconvolution was calculated in a homogeneous mean (water) and considered uniform in the FOV, the whole process was valid only for uniform phantoms. Another disadvantage of this technique is that the deconvolution was applied by taking the Fourier transform of the positron range function and dividing it into the transform of the data: the division in the frequency space increases the noise level damaging the overall image quality.

A similar technique can be applied to the reconstructed image which corresponds to the annihilation distribution, when not corrected for the positron range. We can think of deconvolving the distribution with a voxel-dependent PSF in order to obtain a blurred positron emission map. This technique is not often of use due to the level of noise that we reach in the image after convolution.

The main currently used approach is positron range correction during the reconstruction process. This consists of estimating and adding the positron range effect in the system matrix, which is composed as a product of matrices [195, 196], as we have already introduced in Section 2.6.3. In this way the positron range matrix can be used only during the projection operation and not the back-projection, reducing the computational time and the number of iterations needed for convergence [197]. In this case we talk about *unmatched* projector. To correct for the positron range effect we apply a convolution with a voxel-dependent kernel all along the FOV. In fact, as we have already seen, the positron range depends on the material density and on the positron energy. The kernels need to be studied *ad hoc* based on the phantom and on the employed radioisotope, which brings us to the main problem of this correction method, the memory storage. To simplify calculations and to avoid a huge matrix's memory allocation, it is often suggested to use an invariant and isotropic kernel [198] that is computed in an homogeneous phantom, often made of water. This might result in an over or under correction of the images if the positron emission happened in a non-water equivalent tissue (e.g. lungs [39] or bone). The best results are achieved when the imaged objects do not present high heterogeneity and the tumors are not on the boundary between different materials.

Several studies for positron range correction based on variant kernel convolution on anatomical MRI and CT images were also conducted [199, 200, 178, 182, 201]. Other techniques were studied for heterogeneous objects [202, 40]; Bai in 2005 [82] proposed the truncation of the PSF to reduce artifacts

due to the boundary effect. Results showed that at matched noise levels this positron range model gives better contrast, nevertheless the best trade-off between noise and resolution is achieved without truncation.

The approach of Alessio and MacDonald in 2008 [182] consisted of estimating variant kernels for all materials in a homogeneous mean and build a voxel-dependent kernel during reconstruction, interpolating the previously estimated kernels.

Monte Carlo simulations are the alternative to analytical models, although they highly extend the reconstruction time to propagate the positron interactions iteration per iteration on forward and back-projection.

FIGURE 5.2: Reconstructed images using different positron range correction, β indicates the noise level [203].

Several alternatives were proposed, especially on unmatched projectors to reduce computation: Fu in 2008 [204, 203] studied a positron range model based on Geant4, incorporated in a factorized system matrix based on residual correction every 5 image updates. The attenuation characteristics of the object

were obtained from a CT scan and the on-the-fly Monte Carlo simulation was incorporated in the forward projector. In Fig. 5.2 we show the study's results: the first row from the top presents the noiseless-data results, the second row refers to noisy data and the third row shows noisy-filtered data. This method is worth mentioning due to Fu's technique being one order of magnitude faster than the conventional Monte Carlo model and reaching good image quality after correction.

Another more recent Monte Carlo study for positron range was proposed by Autret in 2015 [124], exploiting GPUs for faster simulation.

Nowadays the increasing use of neural networks in PET imaging could lead to a positron range modelization and correction based on deep learning, since intensive PET scattering and attenuation correction studies have been carried out in the past few years [205, 206, 207].

5.4 Proposed correction

For the XEMIS2 project the interest in positron range correction concerns the use of Sc-44 as 3- γ radioisotope, whose positron range is not negligible as seen in Table 1.1 in Chapter 1.

In this section we discuss the two implemented approaches in CASToR to correct for the effect: first through an invariant kernel approach and second through a material-based variant kernel. The materials map was obtained from the GATE phantom's file.

5.4.1 Simulation and phantoms

The phantom chosen for this study is composed of a 12-cm-long cylinder with 3.5-cm radius positioned in the center of the FOV, within which we find five hot spheres, see Fig. 5.3 and Table 5.2. The materials were chosen to be water, lung and bone, to explore three mediums of very different densities (1.00 g/cm³ water, 0.26 g/cm³ lung and 1.42 g/cm³ bone) [39, 208].

Data are simulated in GATE v6 using the Penelope model. The total simulated activity is 20 kBq for a data acquisition time of 20 minutes, with a factor 15 of contrast between the hot spots and the background.

Sphere nb	Position [mm]	Radius [mm]	Material	Density [g/cm ³]
1	(0.0, 17.5, 0.0)	2	water	1.00
2	(-8.8, 15.1, 0.0)	4	water	1.00
3	(-17.5, 0.0, 0.0)	8	water	1.00
4	(0.0, -17.5, 0.0)	10	lung	0.26
5	(17.2, 3.7, 0.0)	12	bone	1.42

TABLE 5.2: Description of the spheres in the cylindrical phantom: reference number, position in mm considering the center of the FOV as the origin, and radius size.

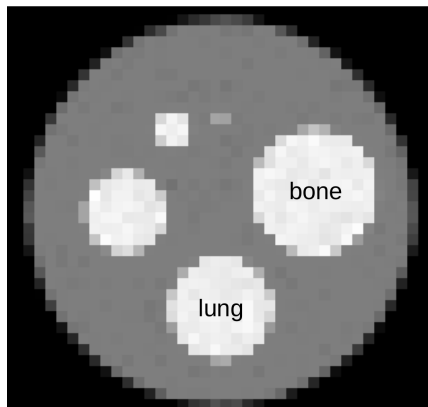


FIGURE 5.3: Axial view of the central slice of the phantom showing the three spheres of 2, 4, and 8-mm radius made of water and the two with a 10 and 12-mm radius made of lung and bone.

5.4.2 Reconstruction and positron range correction estimation

The reconstruction was carried on in CASToR using a LM-MLEM algorithm in which we implemented the positron range correction through convolution. We show results obtained with conventional 2- γ and 3- γ reconstruction to be able to compare the two approaches, with and without positron range correction.

CASToR is designed as a flexible and generic software in which we can easily develop an image convolution in any algorithm, at any point during the program execution. In particular, for a stationary kernel, the convolution is already implemented in the software, with multiple choices as of when to apply it: on the image to be forward projected, on the back-projection's correction terms, on the reconstructed image as a post-processing step, or on the current estimated image. Moreover, CASToR's convolution operation is fast since the image is saved in a padded buffer, in which zeros are added along each dimension following the maximum kernel size on the current

Material	FWHM [mm]	FOV position [mm]
Water	1.9	0, 0, 0
Bone	1.9	0, 0, -60
Lung	2.2	0, 0, 60

TABLE 5.3: Transaxial and axial FWHM values of the kernel used to correct for Sc-44 positron range in water, bone and lung.

dimension.

In our implemented correction techniques with a variant kernel, we chose to apply an isotropic convolution on the image to be forward projected at each iteration. The developed algorithm accepts 4 different kernels, for the 4 materials in the phantom, and for each of them, we can specify the number of Gaussian sigmas and the FWHM (axial and transaxial).

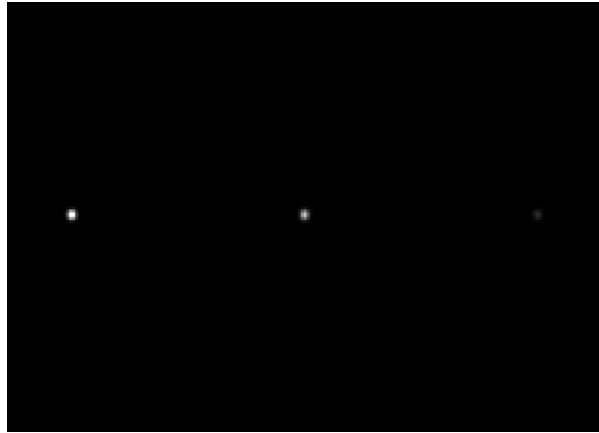


FIGURE 5.4: Transaxial view of the central slice of the PSF study phantoms showing the three point-source spheres made of bone, water and lung, from left to right.

The values of the kernels FWHM were calculated from a 20-minute simulation of three point sources, one of each material, with 1000 Bq of initial activity in each of them. In Fig. 5.4 we see the reconstructed objects, in Table 5.3 we show the values chosen for the convolution and in Fig. 5.5, 5.6 and 5.7 the Gaussian fit of the PSFs.

In order to associate the right kernel to every voxel, the convolution algorithm takes in input a labeled image with numbers from 0 to 3, each of them corresponding to a different kernel to be used during convolution. In our case the labeled image was directly obtained from the GATE phantom and based on the simulated materials.

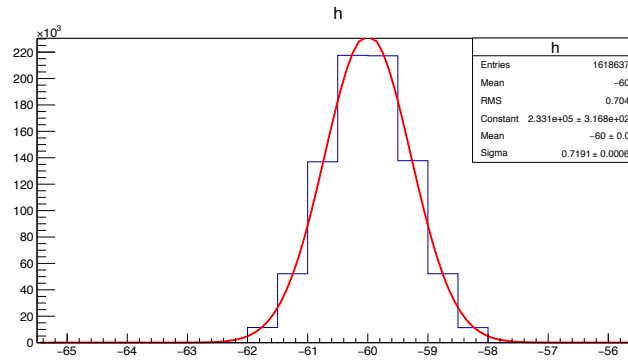


FIGURE 5.5: PSF plot and Gaussian fit for the bone sphere in $(0, 0, -60)$.

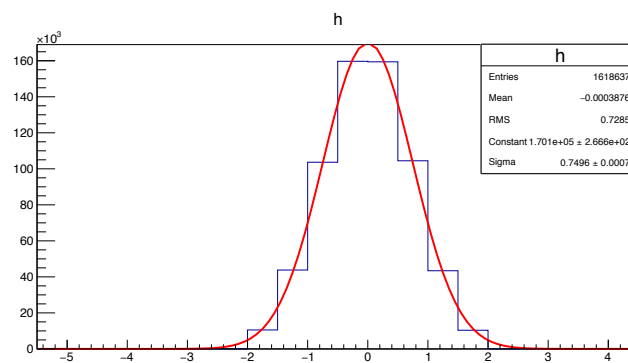


FIGURE 5.6: PSF plot and Gaussian fit for the water sphere in $(0, 0, 0)$.

5.5 Results

We begin this section showing the metrics used in the image analysis, then we present the results for both invariant and variant kernel convolution.

5.5.1 Figures of Merit

The metrics employed in the positron range image analysis are the SNR and the CNR, that were calculated as follows:

$$\text{SNR} = \frac{\mu_s - \mu_b}{\sigma_b}, \quad (5.2)$$

$$\text{CNR} = \frac{|\mu_s - \mu_b|}{\sqrt{\sigma_b^2 + \sigma_s^2}}. \quad (5.3)$$

where the label b refers to the background and the label s to the hot spot.

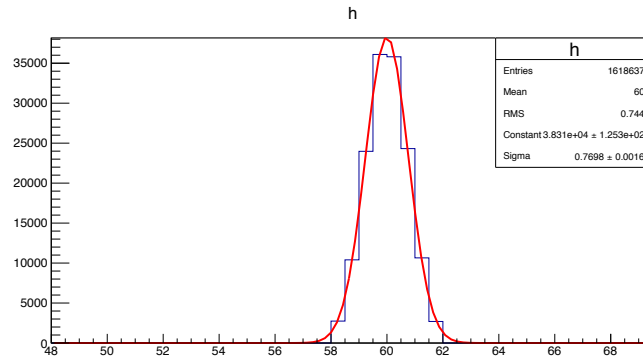


FIGURE 5.7: PSF plot and Gaussian fit for the lung sphere in $(0, 0, 60)$.

Results are plotted in function of the iteration number, considering each sphere as a separate VOI and the rest of the cylinder as the background.

5.5.2 Invariant and variant kernel convolution

We reconstructed images via conventional PET reconstruction and via pseudo-TOF reconstruction, using a 70-ps resolution. In both algorithms, we added the positron range correction through variant and invariant kernel convolution.

For the invariant kernel case we convolved with a FWHM resulting from the average of the values in Table 5.3, i.e. 2.0 mm. For the variant case, the 10-mm-radius sphere and the 12-mm-radius sphere were associated with the corresponding values in Table 5.3 and the rest of the image was convolved with a FWHM equal to 1.9 mm, considering that we are in presence of water and air.

In Fig. 5.8 we present the transaxial central slice of the phantom for the six different reconstructions on the 30-th iteration, after applying a smoothing Gaussian filter: (a) 2- γ and (b) 3- γ with no positron range correction; (c) 2- γ and (d) 3- γ with a correction through variant or material-based kernel convolution; (e) 2- γ and (f) 3- γ with a stationary kernel convolution correction.

In Fig. 5.9 we show the yellow line profiles: the line passes through the two spheres with the bone (12-mm radius) and lung (10-mm radius) density.

The plots concerning the SNR and CNR values for the three water-dense spheres are showed in Fig. 5.10 while in Fig. 5.11 we show the same results for the other two spheres.

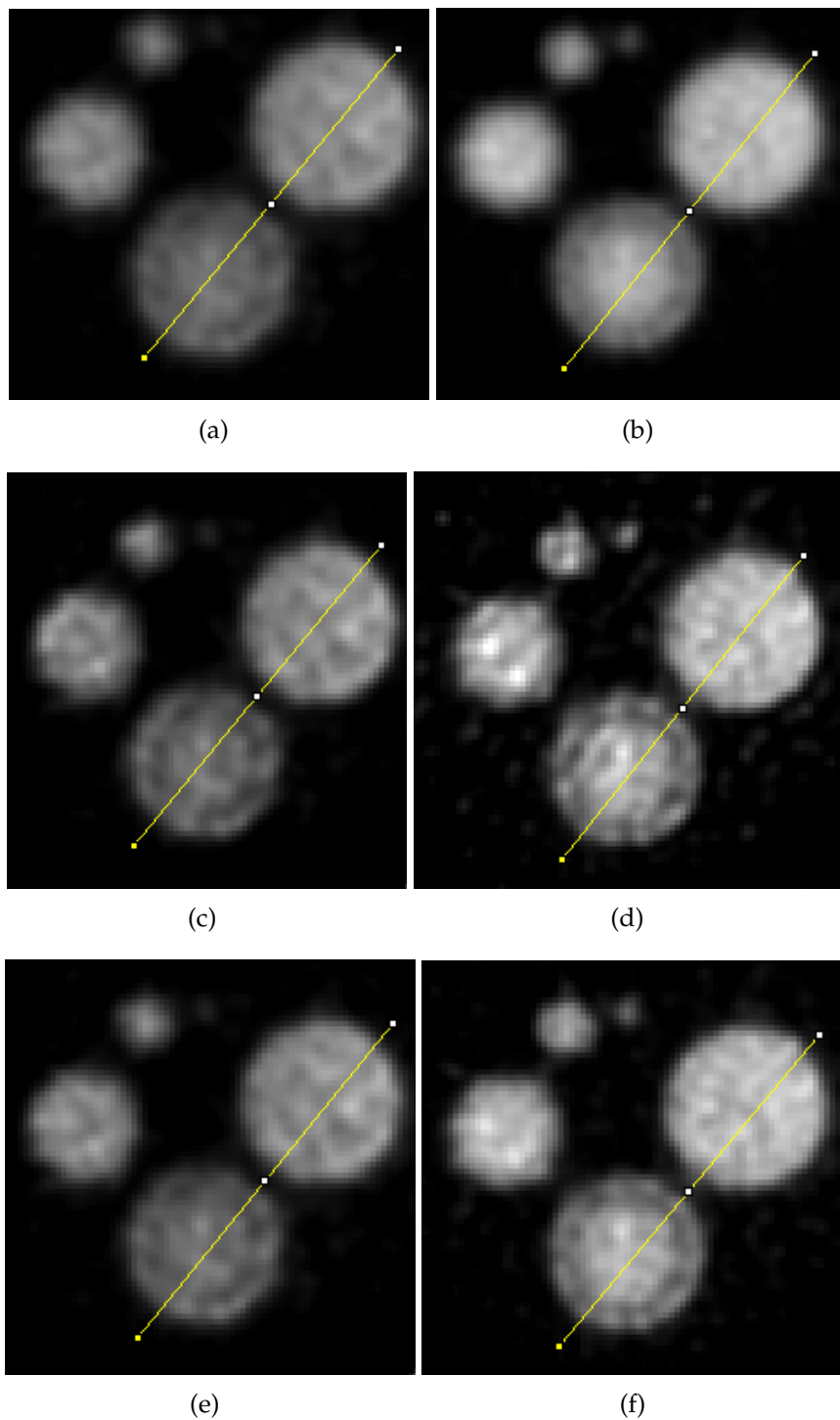


FIGURE 5.8: Transaxial view of the NEMA-like phantom, reconstructed with four different techniques: (a) conventional 2- γ PET and (b) 3- γ , with no positron range correction; (c) 2- γ and (d) 3- γ reconstruction convolved with a variant kernel, (e) 2- γ and (f) 3- γ reconstruction convolved with a stationary kernel.

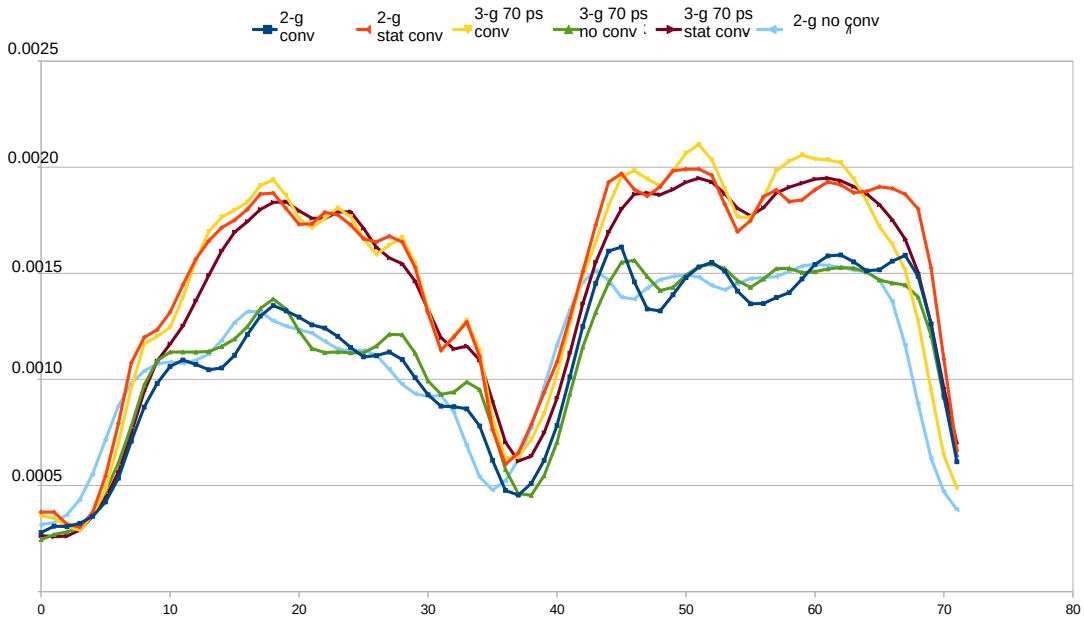


FIGURE 5.9: Plot profiles of the six different reconstructions through the yellow line seen in Fig. 5.8.

5.6 Discussion

The results in this section are obtained applying the positron range correction to the image before each iteration forward projection. We present images and plots concerning 2- γ and 3- γ reconstruction with variant and invariant kernel convolution. The variant kernel correction was based on a material study, carried out through three PSFs' simulation related to the three materials found in the phantom.

A first effect of positron range correction can be seen in Fig. 5.8, where the reconstructed images using conventional PET reconstruction (first column) and our proposed 3- γ approach (second column) are compared to the ones obtained through the same image reconstruction techniques with the positron range convolution correction.

Apart from the contrast improvement due to the use of 3- γ instead of classical PET reconstruction, the general contrast of all the five spheres is improved in the corrected images, especially for 3- γ in (d) and (f), respectively variant and invariant kernel convolution. The improvement is properly quantified in the plot in Fig. 5.9, where we show the profile along the yellow lines for all the six reconstructions. Between the profiles of the 2- γ reconstructions and the ones related to the 3- γ we have a gap of 20% on the grayscale, while there is no remarkable difference between convolved images and not corrected ones for the same image reconstruction technique.

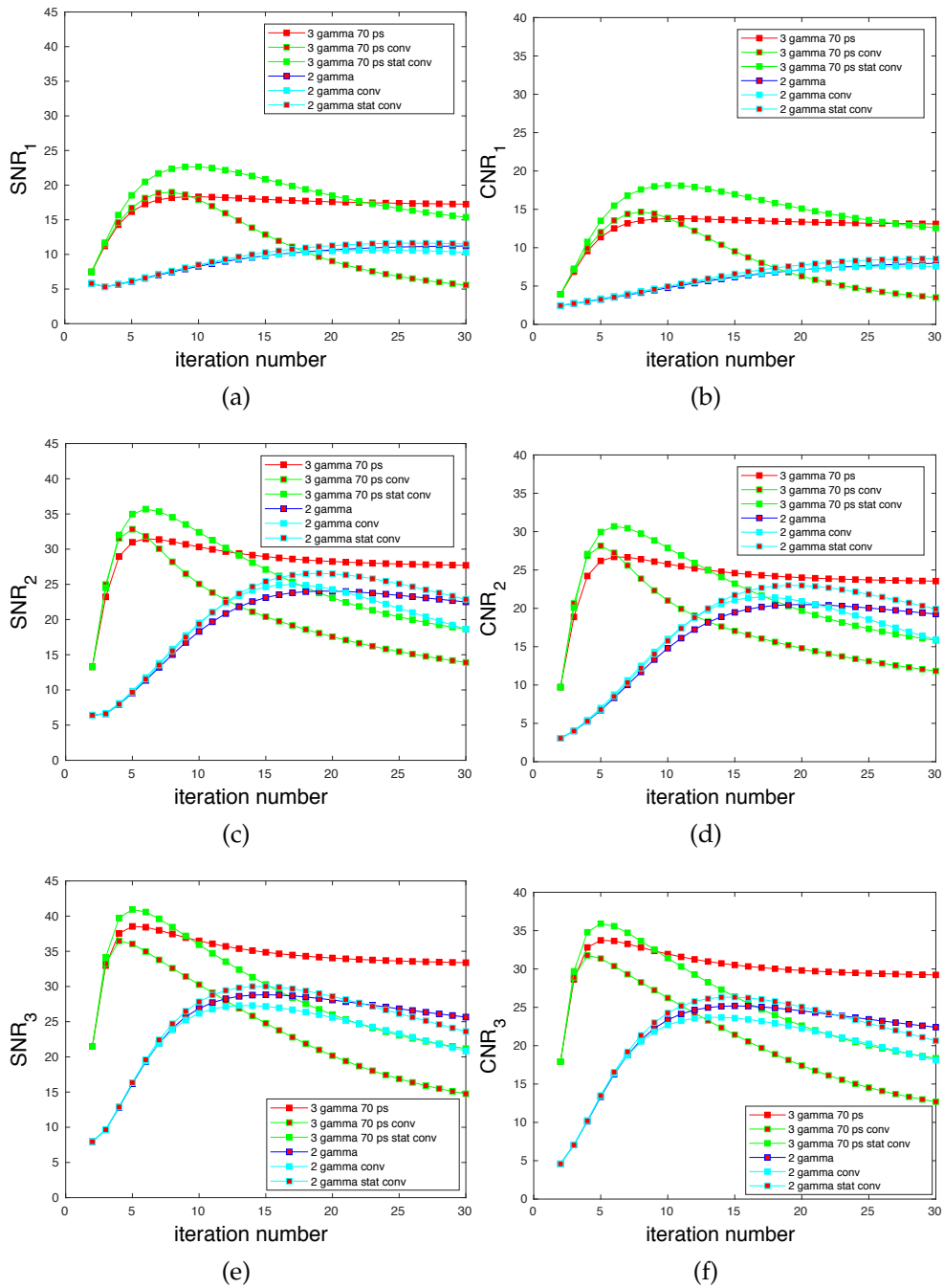


FIGURE 5.10: SNR and CNR plots of the three smallest spheres, water-made: in numerical order sphere of 2-mm, 4-mm and 8-mm radius. With "conv" we refer to variant kernel convolution, while "stat conv" refers to the invariant kernel convolution correction.

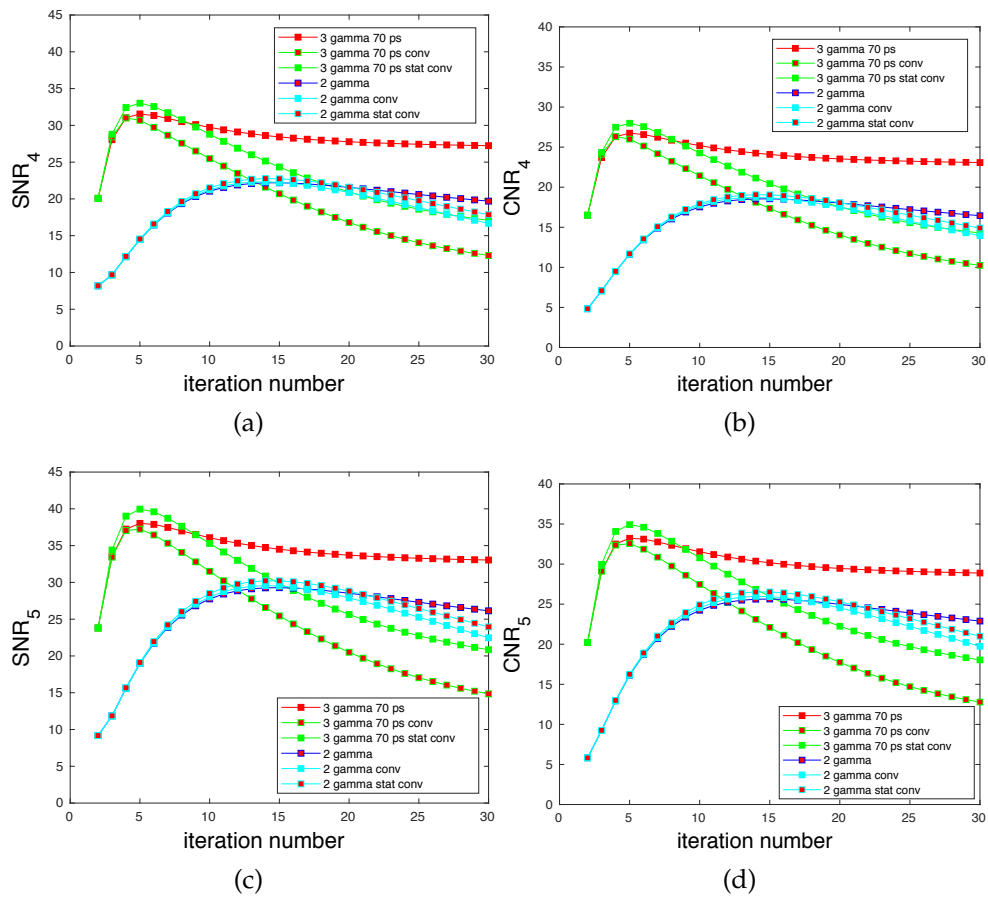


FIGURE 5.11: SNR and CNR plots of the two biggest spheres: sphere number 4, 10-mm radius with lung density and sphere number 5, 12-mm radius with bone density. With "conv" we refer to variant kernel convolution, while "stat conv" refers to the invariant kernel convolution correction.

To have a deeper image analysis we can look at the plots in Fig. 5.10 and 5.11 where we find the results related to SNR and CNR. We decided to show the results for the water sphere in the first figure 5.10 and for the sphere composed of different materials (lung and bone) in the second figure 5.11. The values are shown in function of the iteration number to follow the convergence behavior, which is faster in the $3\text{-}\gamma$ case due to the TOF-like characteristics of our proposed method. The peak values are higher for the pseudo-TOF technique and we reach convergence already around the 20-th iteration.

A proper comparison cannot be carried on between two methods so different from each other, since a very important feature in image reconstruction is the convergence rate. Indeed, the noise in the image increases with the iteration number, as well as the time needed to obtain results. Those two characteristics are of the highest importance in a medical context and cannot be ignored.

In the shown results we see that the SNR and CNR peak values are much higher for the $3\text{-}\gamma$ technique than for the conventional $2\text{-}\gamma$ reconstruction, nevertheless, the values at the 30-th iteration tend to keep up only for not-corrected $3\text{-}\gamma$ images, due to the blurring introduced by the convolution.

In this particular case, the best way to acknowledge an improvement once the correction is applied lies in the visual results in Fig. 5.8.

Conclusion and perspectives

The work presented in this thesis focused on the development of a novel reconstruction technique for 3- γ imaging, which was evaluated on the XEMIS2 imaging system geometry. The XEMIS2 study is the preclinical part of the more general XEMIS project, which already developed a first prototype, the XEMIS1. The characterization of the XEMIS1 Compton camera gave the experimental demonstration of the feasibility of 3- γ imaging, we find the previous studies in LXe Gallego-Manzano [4], Oger [5], and Grignon [6].

In this work we use the third-gamma interactions in LXe to determine a Compton cone, whose point of intersection with the LOR, obtained from the coincidence photons, allows to narrow the localization of the LOR section involved in the combined *annihilation + emission* event. The event is then reconstructed using a pseudo-TOF MLEM algorithm where the line-cone intersection is taken as the center of a Gaussian PDF used in the reconstruction, in a similar fashion as in TOF-PET, whence the denomination of the proposed method as pseudo-TOF. A main advantage associated with the proposed approach is to allow for seamless embedding of the third gamma information through existing reconstruction frameworks with TOF capability, such as CASToR. Doing so, we leverage state of the art reconstruction techniques, which is an important step towards feasibility in a real clinical setting.

We showed a simulation-based study of a realistic 20-minute data acquisition with 20 kBq of initial radioactivity in the XEMIS2 detector. We simulated a NEMA-like and Digimouse phantom and showed image quality improvement for objects of various densities and dimensions. In Chapter 3 we presented the LCI coordinate calculation, on which we base the 3- γ image reconstruction method. In particular in section 3.3.1 and 3.3.2, we discussed the mandatory detector characteristics in terms of spatial, energy and angular resolution to reduce the uncertainty on the LCI point.

The computation of the LCI coordinates is a crucial step towards the application of the proposed approach in a real clinical context. For this, one must be able to determine with sufficient accuracy the localization of

three clusters of interaction in LXe : the two clusters corresponding to the annihilation photons and the one corresponding to the third gamma.

The main challenges related to the detection of three gamma events in real data concern the clustering of the LOR and $3\text{-}\gamma$ groups, as well as the determination of the Compton angle and of the first two points of interactions for the prompt gamma used to determine the cone.

For the first issue, several clustering methods have been studied through GATE simulation. An initial approach for XEMIS2 proposed by N. Beaupère (Subatech, 2017) consists in accepting only events with at least 4 interactions, one for each coincidence photon and two for the third gamma to build the Compton cone. The division in three groups is based on a distance-study to determine a distance threshold. Through a long realistic GATE simulation he studied the distribution of distances between interactions belonging to the same photon or to different photons, and established that these cases follow two distributions partly overlapping (Fig. 5.12). The distance of $D_{\text{cut}} = 74 \text{ mm}$ is taken as the distance-cut to determine if the interaction belongs or not to the same group. The distinction between the third-gamma group and the 511-keV-photons groups is based on the group released energy amount: since the prompt gamma is more energetic (1.157 keV) the group with more than 511-keV energy is the one used to compute the Compton cone.

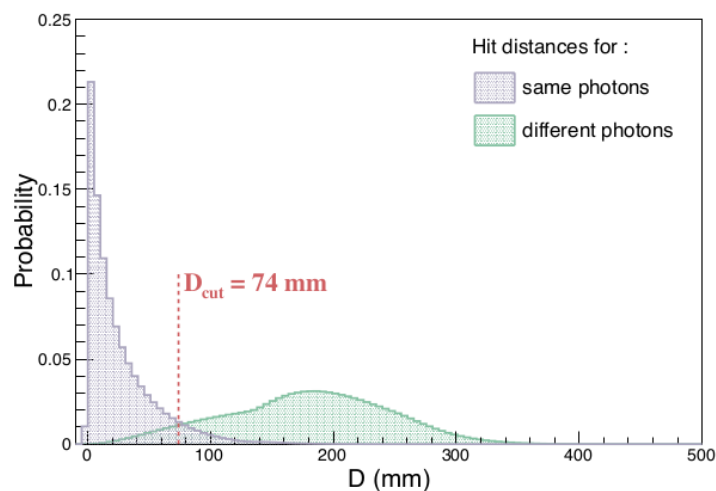


FIGURE 5.12: Distance study to determine the D_{cut} to use in the interactions clustering.

During the course of this thesis we also explored a second unsupervised clustering strategy based on k-means, which achieved similar accuracy to Beaupère's study.

The clustering step is followed by the determination of the Compton cone, whose complexity is guided by combinatorics. In real scenarios, the only information that we have access to is related to the position and to the energy loss, with their respective uncertainties. If a photon interacts N times in the LXe, $N - 1$ interactions are due to Compton scattering and one is photoelectric. There are, therefore, $N!$ possible combinations of interactions to consider while looking for the optimal path. The selected sequence of interactions is chosen using a χ^2 test on the difference between the geometrical angle and the one obtained through Compton kinematics.

The main issues with this method are the low number of events registered as 3- γ due to the many sources of error in the LCI computation process, and the long computational time associated with the determination of the right path-sequence for each event. A novel approach to improve the determination of the LCI coordinate using machine learning methods is exposed in the next section.

3- γ detection using Neural Networks

Several works have proposed to use neural networks for the determination of the interaction point in monolithic detectors [209, 210, 211, 212, 213] and some studies have also focused on establishing Compton kinematics using machine learning methods [214, 215]. These techniques are mainly based on 511-keV photons scattering as they were proposed for PET but can nevertheless be considered in the present context of 3- γ imaging.

Recent studies carried on in our group have demonstrated that an ensemble of deep multi-layer neural networks trained on extensive Monte Carlo simulations is able to robustly predict the interaction point in monolithic detectors even in the presence of imperfect geometries [209].

We suggest to leverage the predictive power of similar neural network architectures to better determine the LCI point in future XEMIS2 experiments. The LCI determination could be divided into two sub-problems related to:

1. The clustering of the three groups of interaction corresponding to a 3- γ event.
2. The reconstruction of the Compton cone from the third gamma group.

These two problems can be tackled using different feed-forward multi-layer perceptrons (MLPs) architectures.

For the clustering we can consider a 4-class MLP classifier taking as inputs the positions and energies of each interaction within an event and predicting as output the classification in four groups: two annihilation groups, one third-gamma group and one group corresponding to spurious interactions.

For the prediction of the Compton cone, two strategies may be adopted:

- Similarly to the clustering case, a MLP classifier can be trained to identify the first and second interaction within the third gamma group, followed by conventional Compton kinematics as described in this thesis.
- Alternatively, a regressor MLP could be directly trained to predict the LCI using the third gamma without explicit Compton kinematics. The criterion would be the minimization of the distance to the annihilation point through e.g. least squares.

While both classification and regression strategies can be considered, classification MLPs seem more appealing as they could directly serve as a replacement for the current clustering approach. The impact of such a procedure could be evaluated straightforwardly using the same reconstruction method developed in this thesis. In the near future, we will therefore study the potential improvements achieved by this strategy on image reconstruction quality.

Contributions

In this manuscript we presented a new image reconstruction technique for 3- γ imaging, that we called pseudo-TOF.

This thesis' work consisted in:

- the implementation of the proposed technique within an existing image reconstruction framework (CASToR);
- a GATE simulation study using Sc-44 and XEMIS2 geometry using two phantoms: a NEMA-like and a more realistic Digimouse;
- a quantitative analysis with respect to the pseudo-TOF resolution as reconstruction parameter;
- the implementation of positron range correction through variant and invariant kernel convolution in CASToR;

- a qualitative and quantitative analysis comparing conventional and pseudo-TOF reconstruction;
- realization of the first reconstructed images for XEMIS2, through conventional and 3- γ reconstruction.

Bibliography

- [1] National Institute of Standards and Technology. <https://www.nist.gov/>.
- [2] Lukas M Carter et al. "The impact of positron range on PET resolution, evaluated with phantoms and PHITS Monte Carlo simulations for conventional and non-conventional radionuclides". In: *Molecular Imaging and Biology* 22.1 (2020), pp. 73–84.
- [3] Jason P Holland et al. "⁸⁹Zr-DFO-J591 for immunoPET of prostate-specific membrane antigen expression in vivo". In: *Journal of Nuclear Medicine* 51.8 (2010), pp. 1293–1300.
- [4] Lucia Gallego Manzano. "Optimization of a single-phase liquid xenon Compton camera for 3γ medical imaging". PhD thesis. Ecole de Mines, 2016.
- [5] Tugdual Oger. "Développement expérimental d'un télescope Compton au xenon liquide pour l'imagerie médicale fonctionnelle". PhD thesis. 2012.
- [6] Cyril Grignon. "Étude et développement d'un télescope Compton au xénon liquide dédié à l'imagerie médicale fonctionnelle". PhD thesis. 2007.
- [7] Herrmann L Blumgart, Soma Weiss, et al. "STUDIES ON THE VELOCITY OF BLOOD FLOW: IV. The Velocity of Blood Flow and Its Relation to Other Aspects of the Circulation in Patients with Arteriosclerosis and in Patients with Arterial Hypertension 1". In: *The Journal of clinical investigation* 4.2 (1927), pp. 173–197.
- [8] James H Scatliff and Peter J Morris. "From Roentgen to magnetic resonance imaging: the history of medical imaging". In: *North Carolina medical journal* 75.2 (2014), pp. 111–113.
- [9] J Stauss et al. "Guidelines for ¹⁸F-FDG PET and PET-CT imaging in paediatric oncology". In: *European journal of nuclear medicine and molecular imaging* (2008).

- [10] Gunnar Brix et al. "Radiation exposure of patients undergoing whole-body dual-modality 18F-FDG PET/CT examinations". In: *Journal of Nuclear Medicine* (2005).
- [11] J. Xu et al. "200x Low-dose PET Reconstruction using Deep Learning". In: *Computing Research Repository* (2017).
- [12] W. T. Baxter et al. "Determination of signal-to-noise ratios and spectral SNRs in cryo-EM low-dose imaging of molecules". In: *Journal of Structural Biology* (2009).
- [13] J. Shtok et al. "Sparsity-based sinogram denoising for low-dose computed tomography". In: *IEEE International Conference on Acoustics, Speech and Signal Processing*. 2011.
- [14] Y. Chen et al. "Artifact Suppressed Dictionary Learning for Low-Dose CT Image Processing". In: *IEEE Transactions on Medical Imaging* (2014).
- [15] C Romo-Luque, PETALO Collaboration, et al. "PETALO: Time-of-Flight PET with liquid xenon". In: *Nuclear Instruments and Methods in Physics Research Section A: Accelerators, Spectrometers, Detectors and Associated Equipment* (2019).
- [16] Samuel Salvador, Daniel Huss, and David Brasse. "Design of a high performances small animal PET system with axial oriented crystals and DOI capability". In: *IEEE Transactions on Nuclear Science* 56.1 (2009), pp. 17–23.
- [17] Kajal Aggarwal. "Impact of preclinical PET scanner characteristics on the overall image quality". PhD thesis. Strasbourg, 2019.
- [18] L. A. Shepp and Y. Vardi. "Maximum Likelihood Reconstruction for Emission Tomography". In: *IEEE Transactions on Medical Imaging* 1.2 (1982), pp. 113–122. ISSN: 1558-254X. DOI: [10.1109/TMI.1982.4307558](https://doi.org/10.1109/TMI.1982.4307558).
- [19] K. Kacperski et al. "Three-gamma annihilation imaging in positron emission tomography". In: *IEEE Transactions on Medical Imaging* (2004).
- [20] C Lang et al. "Sub-millimeter nuclear medical imaging with high sensitivity in positron emission tomography using $\beta^+\gamma$ coincidences". In: *Journal of Instrumentation* (2014).
- [21] R Masełek et al. "Towards 2+ 1 photon tomography: Energy-based selection of two 511 keV photons and a prompt photon with the J-PET scanner". In: *arXiv preprint arXiv:1803.00996* (2018).

- [22] Pawel Moskal et al. "Feasibility study of the positronium imaging with the J-PET tomograph". In: *Physics in medicine and biology* (2019).
- [23] S. et al. Niedźwiecki. "J-PET: A New Technology for the Whole-body PET Imaging". In: *Acta Physica Polonica B* (2017).
- [24] Krzemień et al. "J-PET analysis framework for the prototype TOF-PET detector". In: *Bio-Algorithms and Med-Systems* (2014).
- [25] M Pfützner et al. "Radioactive decays at limits of nuclear stability". In: *Reviews of modern physics* 84.2 (2012), p. 567.
- [26] Robley Duglison Evans. "The atomic nucleus". In: (1955).
- [27] Joseph Louis Marc Chapdelaine. "Scattering of Positrons by Hydrogen Atoms and Formation of Positronium". PhD thesis. Faculty of Graduate studies and Research of McGill University., 1955.
- [28] Jerzy Dryzek et al. "An undergraduate experiment to test relativistic kinematics using in flight positron annihilation". In: *American Journal of Physics - AMER J PHYS* 74 (Jan. 2006), pp. 49–53. DOI: [10.1119/1.2142624](https://doi.org/10.1119/1.2142624).
- [29] Dale L. Bailey, Joel S. Karp, and Suleman Surti. "Physics and Instrumentation in PET". In: *Positron Emission Tomography: Basic Sciences*. Ed. by Dale L. Bailey et al. London: Springer London, 2005, pp. 13–39. ISBN: 978-1-84628-007-8. DOI: [10.1007/1-84628-007-9_2](https://doi.org/10.1007/1-84628-007-9_2). URL: https://doi.org/10.1007/1-84628-007-9_2.
- [30] M Kheradmand Saadi and R Machrafi. "Development of a new code for stopping power and CSDA range calculation of incident charged particles, part A: Electron and positron". In: *Applied Radiation and Isotopes* (2020), p. 109145.
- [31] Mustafa Çağatay Tufan and Hasan Gümüş. "A study on the calculation of stopping power and CSDA Range for incident positrons". In: *Journal of nuclear materials* 412.3 (2011), pp. 308–314.
- [32] William R Leo. *Techniques for nuclear and particle physics experiments: a how-to approach*. Springer Science & Business Media, 2012.
- [33] HJ Bhabha. "The scattering of positrons by electrons with exchange on Dirac's theory of the positron". In: *Proceedings of the Royal Society of London. Series A-Mathematical and Physical Sciences* 154.881 (1936), pp. 195–206.

- [34] Jens Lindhard. "On the properties of a gas of charged particles". In: *Dan. Vid. Selsk Mat.-Fys. Medd.* 28 (1954), p. 8.
- [35] RH Ritchie. "Interaction of charged particles with a degenerate Fermi-Dirac electron gas". In: *Physical Review* 114.3 (1959), p. 644.
- [36] Donald E Groom and SR Klein. "Passage of particles through matter". In: *The European Physical Journal C-Particles and Fields* 15.1-4 (2000), pp. 163–173.
- [37] Simon Ferguson et al. "Comparison of scandium-44 g with other PET radionuclides in pre-clinical PET phantom imaging". In: *EJNMMI physics* 6.1 (2019), pp. 1–14.
- [38] Craig S Levin and Edward J Hoffman. "Calculation of positron range and its effect on the fundamental limit of positron emission tomography system spatial resolution". In: *Physics in Medicine & Biology* 44.3 (1999), p. 781.
- [39] Elise C Emond et al. "Effect of positron range on PET quantification in diseased and normal lungs". In: *Physics in Medicine & Biology* 64.20 (2019), p. 205010.
- [40] Bing Bai et al. "Positron range modeling for statistical PET image reconstruction". In: *2003 IEEE Nuclear Science Symposium. Conference Record (IEEE Cat. No. 03CH37515)*. Vol. 4. IEEE. 2003, pp. 2501–2505.
- [41] Michael E Phelps et al. "Effect of positron range on spatial resolution." In: *Journal of nuclear medicine: official publication, Society of Nuclear Medicine* 16.7 (1975), pp. 649–652.
- [42] Lars Jødal, Cindy Le Loirec, and Christophe Champion. "Positron range in PET imaging: an alternative approach for assessing and correcting the blurring". In: *Physics in Medicine & Biology* 57.12 (2012), p. 3931.
- [43] James A. Sorenson "Simon R. Cherry and Michael E. Phelps". *Physics in Nuclear Imaging*. Saunders Elsevier.
- [44] DJ Thompson et al. "Calibration of the energetic gamma-ray experiment telescope (EGRET) for the Compton gamma-ray observatory". In: *The astrophysical Journal supplement series* 86 (1993), pp. 629–656.
- [45] Johann Heinrich Lambert. *Photometria sive de mensura et gradibus luminis, colorum et umbrae*. Klett, 1760.

- [46] August Beer. "Bestimmung der absorption des rothen lichts in farbigen flussigkeiten". In: *Ann. Physik* 162 (1852), pp. 78–88.
- [47] Donald F Swinehart. "The beer-lambert law". In: *Journal of chemical education* 39.7 (1962), p. 333.
- [48] FX Vollenweider et al. "Metabolic hyperfrontality and psychopathology in the ketamine model of psychosis using positron emission tomography (PET) and [18F] fluorodeoxyglucose (FDG)". In: *European neuropsychopharmacology* 7.1 (1997), pp. 9–24.
- [49] Aviral Singh et al. "Scandium-44 DOTATOC PET/CT: First in-human molecular imaging of neuroendocrine tumors and possible perspectives for Theranostics". In: *Journal of Nuclear Medicine* 56.supplement 3 (2015), pp. 267–267.
- [50] S-C Huang et al. "Quantitative measurement of local cerebral blood flow in humans by positron computed tomography and 15O-water". In: *Journal of Cerebral Blood Flow & Metabolism* 3.2 (1983), pp. 141–153.
- [51] William G Kuhle et al. "Quantification of regional myocardial blood flow using 13N-ammonia and reoriented dynamic positron emission tomographic imaging." In: *Circulation* 86.3 (1992), pp. 1004–1017.
- [52] John S Duncan. "Imaging and epilepsy." In: *Brain: a journal of neurology* 120.2 (1997), pp. 339–377.
- [53] Jens Maus. *Schema of a PET acquisition process*. 2003. URL: http://jens-maus.de/ftp/langner_mscthesi.pdfhttp://jens-maus.de/ftp/langner_mscthesi.bib.
- [54] Charles L Melcher. "Scintillation crystals for PET". In: *Journal of Nuclear Medicine* 41.6 (2000), pp. 1051–1055.
- [55] Saint-Gobain. *Organic Scintillation Materials and Assemblies*. 2020. URL: <https://www.crystals.saint-gobain.com/sites/imdf.crystals.com/files/documents/organics-plastic-scintillators.pdf>.
- [56] K Abe et al. "A measurement of the scintillation decay time constant of nuclear recoils in liquid xenon with the XMASS-I detector". In: *Journal of Instrumentation* 13.12 (2018), P12032.
- [57] M. Miyajima, S. Sasaki, and H. Tawara. "Numbers of scintillation photons produced in NaI(Tl) and plastic scintillator by gamma-rays". In: *IEEE Transactions on Nuclear Science* 40.4 (1993), pp. 417–423.

- [58] Tadayoshi Doke et al. "Let dependence of scintillation yields in liquid argon". In: *Nuclear Instruments and Methods in Physics Research Section A: Accelerators, Spectrometers, Detectors and Associated Equipment* 269.1 (1988), pp. 291–296.
- [59] Glenn F Knoll. *Radiation detection and measurement*. John Wiley & Sons, 2010.
- [60] Maurizio Conti. "State of the art and challenges of time-of-flight PET". In: *Physica Medica* 25.1 (2009), pp. 1–11.
- [61] Tom K Lewellen. "Time-of-flight PET". In: *Seminars in nuclear medicine*. Vol. 28. 3. Elsevier. 1998, pp. 268–275.
- [62] Thomas F Budinger. "Time-of-flight positron emission tomography: status relative to conventional PET". In: *Journal of nuclear medicine* 24.1 (1983), pp. 73–78.
- [63] Maurizio Conti. "Effect of randoms on signal-to-noise-ratio in TOF PET". In: *IEEE Nuclear Science Symposium Conference Record, 2005*. Vol. 3. IEEE. 2005, 6–pp.
- [64] Frederic H Fahey. "Data acquisition in PET imaging". In: *Journal of nuclear medicine technology* 30.2 (2002), pp. 39–49.
- [65] Richard Leahy and C Byrne. "Recent developments in iterative image reconstruction for PET and SPECT." In: *IEEE transactions on medical imaging* 19.4 (2000), p. 257.
- [66] Shoaib Usman and Amol Patil. "Radiation detector deadtime and pile up: A review of the status of science". In: *Nuclear Engineering and Technology* 50.7 (2018), pp. 1006–1016.
- [67] J Radon. "On the determination of functions from their integrals along certain manifolds". In: *Ber. Verh, Sachs Akad Wiss.* 69 (1917), pp. 262–277.
- [68] Magnus Dahlbom. *Physics of PET and SPECT Imaging*. Imaging in Medical Diagnosis and Therapy. CRC Press, 2017. ISBN: 1466560134,9781466560130.
- [69] Adam Alessio, Paul Kinahan, et al. "PET image reconstruction". In: *Nuclear medicine* 1 (2006), pp. 1–22.
- [70] Frank Natterer and Frank Wübbeling. *Mathematical methods in image reconstruction*. SIAM, 2001.

- [71] Ronald Bracewell. "The projection-slice theorem". In: *Fourier Analysis and Imaging*. Springer, 2003, pp. 493–504.
- [72] Andreas Maier et al. *Medical Imaging Systems: An Introductory Guide*. Vol. 11111. Springer, 2018.
- [73] Gengsheng L Zeng and Grant T Gullberg. "Can the backprojection filtering algorithm be as accurate as the filtered backprojection algorithm?" In: *Proceedings of 1994 IEEE Nuclear Science Symposium-NSS'94*. Vol. 3. IEEE. 1994, pp. 1232–1236.
- [74] Avinash C Kak and Malcolm Slaney. *Principles of computerized tomographic imaging*. SIAM, 2001.
- [75] Paul E Kinahan, Michel Defrise, and Rolf Clackdoyle. "Analytic image reconstruction methods". In: *Emission Tomography*. Elsevier, 2004, pp. 421–442.
- [76] David S Lalush and Miles N Wernick. "Iterative image reconstruction". In: *Emission tomography*. Elsevier, 2004, pp. 443–472.
- [77] Lee A Feldkamp, Lloyd C Davis, and James W Kress. "Practical cone-beam algorithm". In: *Josa a* 1.6 (1984), pp. 612–619.
- [78] Margaret E Daube-Witherspoon and Gerd Muehllehner. "Treatment of axial data in three-dimensional PET". In: *Journal of nuclear medicine* 28.11 (1987), pp. 1717–1724.
- [79] Robert M Lewitt, Gerd Muehllehner, and Joel S Karp. "Three-dimensional image reconstruction for PET by multi-slice rebinning and axial image filtering". In: *Physics in Medicine & Biology* 39.3 (1994), p. 321.
- [80] Henry Stark et al. "Direct Fourier reconstruction in computer tomography". In: *IEEE Transactions on Acoustics, Speech, and Signal Processing* 29.2 (1981), pp. 237–245.
- [81] Michel Defrise et al. "Exact and approximate rebinning algorithms for 3-D PET data". In: *IEEE transactions on medical imaging* 16.2 (1997), pp. 145–158.
- [82] Bing Bai et al. "Evaluation of MAP image reconstruction with positron range modeling for 3D PET". In: *IEEE Nuclear Science Symposium Conference Record, 2005*. Vol. 5. IEEE. 2005, pp. 2686–2689.

- [83] J G Colsher. "Fully-three-dimensional positron emission tomography". In: *Physics in Medicine and Biology* 25.1 (1980), pp. 103–115. DOI: [10.1088/0031-9155/25/1/010](https://doi.org/10.1088/0031-9155/25/1/010). URL: <https://doi.org/10.1088/0031-9155/25/1/010>.
- [84] Linda Kaufman. "Maximum likelihood, least squares, and penalized least squares for PET". In: *IEEE transactions on medical imaging* 12.2 (1993), pp. 200–214.
- [85] "Andrew Jonathan Reader". "Image reconstruction and correction techniques for positron volume imaging with rotating planar detectors". PhD thesis. "University of London", "1999".
- [86] Richard Gordon, Robert Bender, and Gabor T Herman. "Algebraic reconstruction techniques (ART) for three-dimensional electron microscopy and X-ray photography". In: *Journal of theoretical Biology* 29.3 (1970), pp. 471–481.
- [87] Rainis Haller and Ryszard Szwarc. "Kaczmarz algorithm in Hilbert space". In: *Studia Mathematica* 169 (2005), pp. 123–132.
- [88] Louis Landweber. "An iteration formula for Fredholm integral equations of the first kind". In: *American journal of mathematics* 73.3 (1951), pp. 615–624.
- [89] Arthur P Dempster, Nan M Laird, and Donald B Rubin. "Maximum likelihood from incomplete data via the EM algorithm". In: *Journal of the Royal Statistical Society: Series B (Methodological)* 39.1 (1977), pp. 1–22.
- [90] Kenneth Lange, Richard Carson, et al. "EM reconstruction algorithms for emission and transmission tomography". In: *J. Comput. Assist. Tomogr* 8.2 (1984), pp. 306–316.
- [91] Moritz Blume. "Expectation maximization: A gentle introduction". In: *Technical University of Munich Institute for Computer Science* (2002).
- [92] Miles N Wernick and John N Aarsvold. "Introduction to emission tomography". In: *Emission Tomography*. Elsevier, 2004, pp. 11–23.
- [93] H Malcolm Hudson and Richard S Larkin. "Accelerated image reconstruction using ordered subsets of projection data". In: *IEEE transactions on medical imaging* 13.4 (1994), pp. 601–609.

- [94] Jeroen Verhaeghe and Andrew J Reader. "AB-OSEM reconstruction for improved Patlak kinetic parameter estimation: a simulation study". In: *Physics in Medicine & Biology* 55.22 (2010), p. 6739.
- [95] Florent C Sureau et al. "Impact of image-space resolution modeling for studies with the high-resolution research tomograph". In: *Journal of Nuclear Medicine* 49.6 (2008), pp. 1000–1008.
- [96] Jeroen Verhaeghe, Paul Gravel, and Andrew J Reader. "Quantification task-optimized estimates from OSEM and FBP reconstructions in single-and multi-subject studies". In: *IEEE Nuclear Science Symposium & Medical Imaging Conference*. IEEE, pp. 2977–2981.
- [97] Andrew J. Reader and Habib Zaidi. "Advances in PET Image Reconstruction". In: *PET Clinics* 2.2 (2007). PET Instrumentation and Quantification, pp. 173–190. ISSN: 1556-8598.
- [98] Tsung Hsiao et al. "An accelerated convergent ordered subsets algorithm for emission tomography". In: *Physics in Medicine & Biology* 49.11 (2004), p. 2145.
- [99] Lucas Parra and Harrison H Barrett. "List-mode likelihood: EM algorithm and image quality estimation demonstrated on 2-D PET". In: *IEEE transactions on medical imaging* 17.2 (1998), pp. 228–235.
- [100] Ronald H Huesman et al. "List-mode maximum-likelihood reconstruction applied to positron emission mammography (PEM) with irregular sampling". In: *IEEE transactions on medical imaging* 19.5 (2000), pp. 532–537.
- [101] Thomas E Nichols et al. "Spatiotemporal reconstruction of list-mode PET data". In: *IEEE Transactions on Medical Imaging* 21.4 (2002), pp. 396–404.
- [102] F Lamare et al. "List-mode-based reconstruction for respiratory motion correction in PET using non-rigid body transformations". In: *Physics in Medicine & Biology* 52.17 (2007), p. 5187.
- [103] Julian Besag. "On the statistical analysis of dirty pictures". In: *Journal of the Royal Statistical Society: Series B (Methodological)* 48.3 (1986), pp. 259–279.

- [104] Jeffrey A Fessler. "Penalized weighted least-squares image reconstruction for positron emission tomography". In: *IEEE transactions on medical imaging* 13.2 (1994), pp. 290–300.
- [105] Edward J Hoffman, Sung-Cheng Huang, and Michael E Phelps. "Quantitation in positron emission computed tomography: 1. Effect of object size". In: *Journal of computer assisted tomography* 3.3 (1979), pp. 299–308.
- [106] Edward J Hoffman et al. "Quantitation in positron emission computed tomography: 4. Effect of accidental coincidences." In: *Journal of computer assisted tomography* 5.3 (1981), pp. 391–400.
- [107] Sung-Cheng Huang et al. "Quantitation in positron emission computed tomography: 2. Effects of inaccurate attenuation correction." In: *Journal of computer assisted tomography* 3.6 (1979), pp. 804–814.
- [108] John C Mazziotta et al. "Quantitation in positron emission computed tomography: 5. Physical–anatomical effects." In: *Journal of Computer Assisted Tomography* 5.5 (1981), pp. 734–743.
- [109] Simon R Cherry and Sung-Cheng Huang. "Effects of scatter on model parameter estimates in 3D PET studies of the human brain". In: *IEEE transactions on nuclear science* 42.4 (1995), pp. 1174–1179.
- [110] Marie-Louise Montandon and Habib Zaidi. "Atlas-guided non-uniform attenuation correction in cerebral 3D PET imaging". In: *Neuroimage* 25.1 (2005), pp. 278–286.
- [111] Jinyi Qi et al. "High-resolution 3D Bayesian image reconstruction using the microPET small-animal scanner". In: *Physics in medicine & biology* 43.4 (1998), p. 1001.
- [112] Jinyi Qi and Ronald H Huesman. "Effect of errors in the system matrix on maximum a posteriori image reconstruction". In: *Physics in Medicine & Biology* 50.14 (2005), p. 3297.
- [113] André Braem et al. "Feasibility of a novel design of high resolution parallax-free Compton enhanced PET scanner dedicated to brain research". In: *Physics in Medicine & Biology* 49.12 (2004), p. 2547.
- [114] VV Selivanov et al. "Detector response models for statistical iterative image reconstruction in high resolution PET". In: *IEEE Transactions on Nuclear Science* 47.3 (2000), pp. 1168–1175.

- [115] Jian Zhou and Jinyi Qi. "Fast and efficient fully 3D PET image reconstruction using sparse system matrix factorization with GPU acceleration". In: *Physics in Medicine & Biology* 56.20 (2011), p. 6739.
- [116] Steven Staelens et al. "A three-dimensional theoretical model incorporating spatial detection uncertainty in continuous detector PET". In: *Physics in Medicine & Biology* 49.11 (2004), p. 2337.
- [117] Guillem Pratx and Craig Levin. "Online detector response calculations for high-resolution PET image reconstruction". In: *Physics in Medicine & Biology* 56.13 (2011), p. 4023.
- [118] Julien Bert and Dimitris Visvikis. "A fast CPU/GPU ray projector for fully 3d list-mode PET reconstruction". In: *2011 IEEE Nuclear Science Symposium Conference Record*. IEEE. 2011, pp. 4126–4130.
- [119] Paul E Kinahan et al. "Attenuation correction for a combined 3D PET/CT scanner". In: *Medical physics* 25.10 (1998), pp. 2046–2053.
- [120] Axel Martinez-Möller et al. "Tissue classification as a potential approach for attenuation correction in whole-body PET/MRI: evaluation with PET/CT data". In: *Journal of nuclear medicine* 50.4 (2009), pp. 520–526.
- [121] Matthias Hofmann et al. "MRI-based attenuation correction for whole-body PET/MRI: quantitative evaluation of segmentation-and atlas-based methods". In: *Journal of Nuclear Medicine* 52.9 (2011), pp. 1392–1399.
- [122] NL Christensen et al. "Positron emission tomography within a magnetic field using photomultiplier tubes and lightguides". In: *Physics in Medicine & Biology* 40.4 (1995), p. 691.
- [123] SF Haber, Stephen E Derenzo, and D Uber. "Application of mathematical removal of positron range blurring in positron emission tomography". In: *IEEE transactions on nuclear science* 37.3 (1990), pp. 1293–1299.
- [124] Awen Autret. "Amélioration qualitative et quantitative de reconstruction TEP sur plate-forme graphique". PhD thesis. Telecom Bretagne, Département Image et Traitement de l'Information, 2015.

- [125] Lingxiong Shao, Richard Freifelder, and Joel S Karp. "Triple energy window scatter correction technique in PET". In: *IEEE transactions on medical imaging* 13.4 (1994), pp. 641–648.
- [126] Charles C Watson, DMEC Newport, and Mike E Casey. "A single scatter simulation technique for scatter correction in 3D PET". In: *Three-dimensional image reconstruction in radiology and nuclear medicine*. Springer, 1996, pp. 255–268.
- [127] Jinghan Ye, Xiyun Song, and Zhiqiang Hu. "Scatter correction with combined single-scatter simulation and Monte Carlo simulation for 3D PET". In: *2014 IEEE Nuclear Science Symposium and Medical Imaging Conference (NSS/MIC)*. IEEE. 2014, pp. 1–3.
- [128] Kyung Sang Kim et al. "Ultra-fast hybrid CPU–GPU multiple scatter simulation for 3-D PET". In: *IEEE journal of biomedical and health informatics* 18.1 (2013), pp. 148–156.
- [129] Kyung Sang Kim and Jong Chul Ye. "Fully 3D iterative scatter-corrected OSEM for HRRT PET using a GPU". In: *Physics in Medicine & Biology* 56.15 (2011), p. 4991.
- [130] Ramsey D Badawi et al. "First human imaging studies with the EXPLORER total-body PET scanner". In: *Journal of Nuclear Medicine* 60.3 (2019), pp. 299–303.
- [131] Simon R Cherry, Ramsey D Badawi, and Jinyi Qi. *Essentials of in vivo biomedical imaging*. CRC Press, 2016.
- [132] Z Liang, H Hart, and A Schoenfeld. "Triple gamma coincidence tomographic imaging without image processing". In: *IEEE Conf Eng Med Biol*. Vol. 9. 1987, pp. 825–826.
- [133] James D Kurfess and Bernard F Philips. "Coincident Compton nuclear medical imager". In: *2001 IEEE Nuclear Science Symposium Conference Record (Cat. No. 01CH37310)*. Vol. 2. IEEE. 2001, pp. 1166–1170.
- [134] D Thers and J Cussonneau. "Nuclear medical imaging using beta (+) gamma coincidences from Sc-44 radio-nuclide with liquid xenon as detection medium". In: *EUROPEAN JOURNAL OF NUCLEAR MEDICINE AND MOLECULAR IMAGING*. Vol. 33. SPRINGER 233 SPRING STREET, NEW YORK, NY 10013 USA. 2006, S320–S320.

- [135] L Gallego Manzano et al. "XEMIS: A liquid xenon detector for medical imaging". In: *Nuclear Instruments and Methods in Physics Research Section A* (2015).
- [136] Eiji Yoshida et al. "Whole gamma imaging: a new concept of PET combined with Compton imaging". In: *Physics in Medicine & Biology* 65.12 (2020), p. 125013.
- [137] L. Gallego Manzano et al. "XEMIS2: A liquid xenon detector for small animal medical imaging". In: *Nuclear Instruments and Methods in Physics Research Section A* (2018).
- [138] Ferid Haddad et al. "ARRONAX, a high-energy and high-intensity cyclotron for nuclear medicine". In: *European Journal of Nuclear Medicine and Molecular Imaging* (2008).
- [139] F Roesch. "Scandium-44: benefits of a long-lived PET radionuclide available from the $^{44}\text{Ti}/^{44}\text{Sc}$ generator system". In: *Current radiopharmaceuticals* 5.3 (2012), pp. 187–201.
- [140] Elisabeth Eppard. "Pre-Therapeutic Dosimetry Employing Scandium-44 for Radiolabeling PSMA-617". In: (2018).
- [141] Mateusz Sitarz et al. "Radionuclide candidates for $\beta+\gamma$ coincidence PET: An overview". In: *Applied Radiation and Isotopes* 155 (Jan. 2020), p. 108898. DOI: [10.1016/j.apradiso.2019.108898](https://doi.org/10.1016/j.apradiso.2019.108898). URL: <https://hal.archives-ouvertes.fr/hal-02301340>.
- [142] E. Aprile and T. Doke. "Liquid xenon detectors for particle physics and astrophysics". In: *Rev. Mod. Phys.* (2010).
- [143] Y. Zhu et al. "Scintillation Signal in XEMIS2, a Liquid Xenon Compton Camera with 3γ Imaging Technique". In: *Proceedings of International Conference on Technology and Instrumentation in Particle Physics*. 2018.
- [144] Y. Xing et al. "XEMIS: Liquid Xenon Compton Camera for 3γ Imaging". In: *Proceedings of International Conference on Technology and Instrumentation in Particle Physics*. 2018.
- [145] Elena Aprile et al. *Noble gas detectors*. John Wiley & Sons, 2006.
- [146] Julien Guertault. *Intersection of a ray and a cone*. 2017. URL: <http://lousodrome.net/blog/light/2017/01/03/intersection-of-a-ray-and-a-cone/>.

- [147] RK Batra and Bhupender Singh. "Difference in ranges of positrons and electrons in rare-earth metals". In: *Physical Review B* (1989).
- [148] Simone Weber and Andreas Bauer. "Small animal PET: aspects of performance assessment". In: *European Journal of Nuclear Medicine and Molecular Imaging* (2004).
- [149] William W Moses. "Recent advances and future advances in time-of-flight PET". In: *AIP Conference Proceedings*. AIP. 2010.
- [150] WW Moses. "Time of flight in PET revisited". In: *IEEE Transactions on Nuclear Science* (2003).
- [151] Wai-Hoi Wong et al. "Image improvement and design optimization of the time-of-flight PET". In: *Journal of Nuclear Medicine* (1983).
- [152] S Jan et al. "GATE V6: a major enhancement of the GATE simulation platform enabling modelling of CT and radiotherapy". In: *Physics in Medicine and Biology* (2011).
- [153] Leif Lönnblad. "CLHEP—a project for designing a C++ class library for high energy physics". In: *Computer Physics Communications* (1994).
- [154] S. Agostinelli et al. "GEANT4: A Simulation toolkit". In: *Nuclear Instruments and Methods in Physics Research* (2003).
- [155] Jonathan A Disselhorst et al. "Image-quality assessment for several positron emitters using the NEMA NU 4-2008 standards in the Siemens Inveon small-animal PET scanner". In: *Journal of nuclear medicine* (2010).
- [156] David Stout. "Creating a whole body digital mouse atlas with PET, CT and cryosection images". In: *Mol. Imaging Biol.* 4.4 (2002), S27.
- [157] Belma Dogdas et al. "Digimouse: a 3D whole body mouse atlas from CT and cryosection data". In: *Physics in Medicine & Biology* 52.3 (2007), p. 577.
- [158] T. Merlin et al. "CASToR: a generic data organization and processing code framework for multi-modal and multi-dimensional tomographic reconstruction". In: *Physics in Medicine and Biology* (2018).
- [159] Robert L Siddon. "Fast calculation of the exact radiological path for a three-dimensional CT array". In: *Medical physics* 12.2 (1985), pp. 252–255.

- [160] Filip Jacobs et al. "A fast algorithm to calculate the exact radiological path through a pixel or voxel space". In: *Journal of computing and information technology* 6.1 (1998), pp. 89–94.
- [161] Marina Filipovic, Claude Comtat, and Simon Stute. "Time-of-flight implementation for PET reconstruction in practice". In: *Physics in Medicine & Biology* (2019).
- [162] M Laval, R Allemand, and A Bouvier. *Design and performance of a new positron computed tomograph (PCT) using the time-of-flight information*. Tech. rep. CEA Centre d'Etudes Nucleaires de Grenoble, 1982.
- [163] Joel S Karp et al. "Benefit of time-of-flight in PET: experimental and clinical results". In: *Journal of Nuclear Medicine* (2008).
- [164] A Blanco. "Positron range effects on the spatial resolution of RPC-PET". In: *2006 IEEE Nuclear Science Symposium Conference Record*. Vol. 4. IEEE. 2006, pp. 2570–2573.
- [165] Jorn van Dalen et al. "Effect of the positron range on the spatial resolution of a new generation pre-clinical PET-scanner using F-18, Ga-68, Zr-89 and I-124". In: *Journal of Nuclear Medicine* 49.supplement 1 (2008), 404P–404P.
- [166] Gordon W Philpott et al. "RadioimmunoPET: detection of colorectal carcinoma with positron-emitting copper-64-labeled monoclonal antibody". In: *Journal of Nuclear Medicine* 36.10 (1995), pp. 1818–1824.
- [167] Melissa A Deri et al. "PET imaging with ^{89}Zr : from radiochemistry to the clinic". In: *Nuclear medicine and biology* 40.1 (2013), pp. 3–14.
- [168] Amy L Vavere and Michael J Welch. "Preparation, biodistribution, and small animal PET of ^{45}Ti -transferrin". In: *Journal of Nuclear Medicine* 46.4 (2005), pp. 683–690.
- [169] Elin Pauwels et al. "Somatostatin receptor PET ligands-the next generation for clinical practice". In: *American Journal of Nuclear Medicine and Molecular Imaging* 8.5 (2018), p. 311.
- [170] Frank Rösch et al. "Radiation doses of yttrium-90 citrate and yttrium-90 EDTMP as determined via analogous yttrium-86 complexes and positron emission tomography". In: *European journal of nuclear medicine* 23.8 (1996), pp. 958–966.

- [171] ZH Cho et al. "Positron ranges obtained from biomedically important positron-emitting radionuclides". In: *Journal of nuclear medicine* 16.12 (1975), pp. 1174–1176.
- [172] Stephen E Derenzo. "Mathematical removal of positron range blurring in high resolution tomography". In: *IEEE Transactions on Nuclear Science* 33.1 (1986), pp. 565–569.
- [173] Jacobo Cal-González et al. "Positron range estimations with PeneloPET". In: *Physics in Medicine & Biology* 58.15 (2013), p. 5127.
- [174] Stephen E Derenzo. "Precision measurement of annihilation point spread distributions for medically important positron emitters". In: (1979).
- [175] Matthew R Palmer and Gordon L Brownell. "Annihilation density distribution calculations for medically important positron emitters". In: *IEEE transactions on medical imaging* 11.3 (1992), pp. 373–378.
- [176] Andreas Wirrwar et al. "4.5 tesla magnetic field reduces range of high-energy positrons-potential implications for positron emission tomography". In: *IEEE Transactions on Nuclear Science* 44.2 (1997), pp. 184–189.
- [177] N Jon Shah et al. "Effects of magnetic fields of up to 9.4 T on resolution and contrast of PET images as measured with an MR-BrainPET". In: *PLoS One* 9.4 (2014), e95250.
- [178] Rebekka Kraus, Gaspar Delso, and Sibylle I Ziegler. "Simulation study of tissue-specific positron range correction for the new biograph mMR whole-body PET/MR system". In: *IEEE transactions on nuclear science* 59.5 (2012), pp. 1900–1909.
- [179] RL Harrison et al. "Positron range and coincidence non-collinearity in SimSET". In: *1999 IEEE Nuclear Science Symposium. Conference Record. 1999 Nuclear Science Symposium and Medical Imaging Conference (Cat. No. 99CH37019)*. Vol. 3. IEEE. 1999, pp. 1265–1268.
- [180] Alejandro Sanchez-Crespo, Pedro Andreo, and Stig A Larsson. "Positron flight in human tissues and its influence on PET image spatial resolution". In: *European journal of nuclear medicine and molecular imaging* 31.1 (2004), pp. 44–51.

- [181] Christophe Champion and Cindy Le Loirec. "Positron follow-up in liquid water: I. A new Monte Carlo track-structure code". In: *Physics in Medicine & Biology* 51.7 (2006), p. 1707.
- [182] Adam Alessio and Lawrence MacDonald. "Spatially variant positron range modeling derived from CT for PET image reconstruction". In: *2008 IEEE Nuclear Science Symposium Conference Record*. IEEE. 2008, pp. 3637–3640.
- [183] Wencke Lehnert et al. "Analytical positron range modelling in heterogeneous media for PET Monte Carlo simulation". In: *Physics in medicine & biology* 56.11 (2011), p. 3313.
- [184] Sébastien Jan et al. "GATE: a simulation toolkit for PET and SPECT". In: *Physics in Medicine & Biology* 49.19 (2004), p. 4543.
- [185] Samuel España et al. "PeneloPET, a Monte Carlo PET simulation tool based on PENELOPE: features and validation". In: *Physics in Medicine & Biology* 54.6 (2009), p. 1723.
- [186] Francesc Salvat, José M Fernández-Varea, and Josep Sempau. "PENELOPE-2006: A code system for Monte Carlo simulation of electron and photon transport". In: *Workshop proceedings*. Vol. 4. 6222. Universitat de Barcelona. 2006, p. 7.
- [187] Kenzo Nakamura et al. "Review of particle physics". In: *Journal of Physics G: Nuclear and Particle Physics* 37.7 A (2010), p. 075021.
- [188] F. Rohrlich and B. C. Carlson. "Positron-Electron Differences in Energy Loss and Multiple Scattering". In: *Phys. Rev.* 93 (1 1954), pp. 38–44. DOI: [10.1103/PhysRev.93.38](https://doi.org/10.1103/PhysRev.93.38). URL: <https://link.aps.org/doi/10.1103/PhysRev.93.38>.
- [189] Harry Messel and David F Crawford. *Electron–Photon Shower Distribution Function: Tables for Lead, Copper and Air Absorbers*. Elsevier, 2013.
- [190] Raymond R Raylman, Bruce E Hammer, and Nelson L Christensen. "Combined MRI-PET scanner: a Monte Carlo evaluation of the improvements in PET resolution due to the effects of a static homogeneous magnetic field". In: *IEEE Transactions on Nuclear Science* 43.4 (1996), pp. 2406–2412.

- [191] Ottavia Bertolli et al. "PET iterative reconstruction incorporating an efficient positron range correction method". In: *Physica medica* 32.2 (2016), pp. 323–330.
- [192] D Burdette et al. "A study on PET image quality using both strong magnetic fields and a ML-EM positron range correction algorithm". In: *2009 IEEE Nuclear Science Symposium Conference Record (NSS/MIC)*. IEEE, pp. 3646–3651.
- [193] Shih-ying Huang et al. "The effect of magnetic field on positron range and spatial resolution in an integrated whole-body time-of-flight PET/MRI system". In: *2014 IEEE Nuclear Science Symposium and Medical Imaging Conference (NSS/MIC)*. IEEE. 2014, pp. 1–4.
- [194] Andrew J Reader et al. "EM algorithm system modeling by image-space techniques for PET reconstruction". In: *IEEE Transactions on Nuclear Science* 50.5 (2003), pp. 1392–1397.
- [195] Michel S Tohme and Jinyi Qi. "Iterative image reconstruction for positron emission tomography based on a detector response function estimated from point source measurements". In: *Physics in Medicine and Biology* 54.12 (2009), pp. 3709–3725.
- [196] Vladimir Y Panin et al. "Fully 3-D PET reconstruction with system matrix derived from point source measurements". In: *IEEE transactions on medical imaging* 25.7 (2006), pp. 907–921.
- [197] Jacobo Cal-González et al. "Study of CT-based positron range correction in high resolution 3D PET imaging". In: *Nuclear Instruments and Methods in Physics Research Section A: Accelerators, Spectrometers, Detectors and Associated Equipment* 648 (2011), S172–S175.
- [198] Arman Rahmim et al. "Resolution modeled PET image reconstruction incorporating space-variance of positron range: Rubidium-82 cardiac PET imaging". In: *2008 IEEE Nuclear Science Symposium Conference Record*. IEEE. 2008, pp. 3643–3650.
- [199] Gerrit J Kemerink et al. "Effect of the positron range of ^{18}F , ^{68}Ga and ^{124}I on PET/CT in lung-equivalent materials". In: *European journal of nuclear medicine and molecular imaging* 38.5 (2011), pp. 940–948.
- [200] Jacobo Cal-González et al. "Positron range effects in high resolution 3D PET imaging". In: *2009 IEEE Nuclear Science Symposium Conference Record (NSS/MIC)*. IEEE. 2009, pp. 2788–2791.

- [201] Jacobo Cal González. “Positron range and prompt gamma modeling in PET imaging”. PhD thesis. 2014.
- [202] Yubin Wan et al. “Probability based positron range modeling in inhomogeneous medium for PET”. In: *2006 IEEE Nuclear Science Symposium Conference Record*. Vol. 6. IEEE. 2006, pp. 3372–3375.
- [203] Lin Fu and Jinyi Qi. “A residual correction method for high-resolution PET reconstruction with application to on-the-fly Monte Carlo based model of positron range”. In: *Medical physics* 37.2 (2010), pp. 704–713.
- [204] Lin Fu and Jinyi Qi. “A novel iterative image reconstruction method for high-resolution PET Imaging with a Monte Carlo based positron range model”. In: *2008 IEEE Nuclear Science Symposium Conference Record*. IEEE. 2008, pp. 3609–3612.
- [205] Jaewon Yang et al. “Joint correction of attenuation and scatter in image space using deep convolutional neural networks for dedicated brain 18F-FDG PET”. In: *Physics in Medicine & Biology* 64.7 (2019), p. 075019.
- [206] Jinmin Xu and Huafeng Liu. “Deep-learning-based separation of a mixture of dual-tracer single-acquisition pet signals with equal half-lives: a simulation study”. In: *IEEE Transactions on Radiation and Plasma Medical Sciences* 3.6 (2019), pp. 649–659.
- [207] Tyler J Bradshaw et al. “Feasibility of deep learning–based PET/MR attenuation correction in the pelvis using only diagnostic MR images”. In: *Tomography* 4.3 (2018), p. 138.
- [208] Jacobo Cal-González et al. “Tissue-dependent and spatially-variant positron range correction in 3D PET”. In: *IEEE transactions on medical imaging* 34.11 (2015), pp. 2394–2403.
- [209] A Iborra et al. “Ensemble of neural networks for 3D position estimation in monolithic PET detectors”. In: *Physics in Medicine & Biology* 64.19 (2019), p. 195010.
- [210] Y Wang et al. “3D position estimation using an artificial neural network for a continuous scintillator PET detector”. In: *Physics in Medicine & Biology* 58.5 (2013), p. 1375.

-
- [211] Peter Bruyndonckx et al. "Evaluation of machine learning algorithms for localization of photons in undivided scintillator blocks for PET detectors". In: *IEEE Transactions on Nuclear Science* 55.3 (2008), pp. 918–924.
- [212] Peter Bruyndonckx et al. "Neural network-based position estimators for PET detectors using monolithic LSO blocks". In: *IEEE Transactions on Nuclear Science* 51.5 (2004), pp. 2520–2525.
- [213] Andreas Zoglauer and Steven E Boggs. "Application of neural networks to the identification of the compton interaction sequence in compton imagers". In: *2007 IEEE Nuclear Science Symposium Conference Record*. Vol. 6. IEEE. 2007, pp. 4436–4441.
- [214] Peng Peng et al. "Compton PET: A simulation study for a PET module with novel geometry and machine learning for position decoding". In: *Biomedical Physics & Engineering Express* 5.1 (2018), p. 015018.
- [215] Jean-Baptiste Michaud et al. "Sensitivity in PET: Neural networks as an alternative to compton photons LOR analysis". In: *2007 IEEE Nuclear Science Symposium Conference Record*. Vol. 5. IEEE. 2007, pp. 3594–3600.

Publications and Oral Communications

Journal publications

- *A Pseudo-TOF Image Reconstruction Approach for Three-Gamma Small Animal Imaging*, D. Giovagnoli, A. Bousse, N. Beaupere, C. Canot, J-P. Cussonneau, S. Diglio, A. Iborra Carreres, J. Masbou, T. Merlin, E. Morteau, Y. Xing, Y. Zhu, D. Thers and D. Visvikis, *submitted in IEEE Transactions on Radiation and Plasma Medical Sciences*, August 2020.
- *"Solar Neutrino Detection Sensitivity in DARWIN via Electron Scattering"*, J. Aalbers, F. Agostini, S.E.M. Maouloud, M. Alfonsi, L. Althueser, F. Amaro, J. Angevaere, V.C. Antochi, B. Antunovic, E. Aprile, L. Arazi, F. Arneodo, M. Balzer, L. Baudis, D. Baur, M.L. Benabderrahmane, Y. Biondi, A. Bismark, C. Bourgeois, A. Breskin, P.A. Breur, A. Brown, E. Brown, G. Bruno, S. Brünner, R. Budnik, C. Capelli, J. Cardoso, D. Cichon, M. Clark, A.P. Colijn, J. Conrad, J.J. Cuenca-García, J-P. Cussonneau, M.P. Decowski, A. Depoian, J. Dierle, P. Di Gangi, A. Di Giovanni, S. Diglio, D. Douillet, G. Drexlin, K. Eitel, R. Engel, E. Erdal, A.D. Ferella, H. Fischer, P. Fischer, W. Fulgione, P. Gaemers, M. Galloway, F. Gao, D. Giovagnoli, F. Girard, R. Glade-Beucke, F. Glück, L. Grandi, S. Grohmann, R. Größle, R. Gumbsheimer, V. Hannen, S. Hansmann-Menzemer, C. Hils, B. Holzappel, J. Howlett, G. Iaquaniello, F. Jörg, M. Keller, J. Kellerer, G. Khundzakishvili, B. Kilminster, M. Kleifges, T.K. Kleiner, G. Koltmann, A. Kopec, A. Kopmann, L.M. Krauss, F. Kuger, L. LaCascio, H. Landsman, R.F. Lang, S. Lindemann, M. Lindner, F. Lombardi, J.A.M. Lopes, A. Loya Villalpando, Y. Ma, C. Macolino, J. Mahlstedt, A. Manfredini, T. Marrodán Undagoitia, J. Masbou, D. Masson, E. Masson, N. McFadden, P. Meinhardt, R. Meyer, B. Milosevic, S. Milutinovic, A. Molinaro, C.M.B. Monteiro, K. Morå, E. Morteau, Y. Mosbacher, M. Murra, J.L. Newstead,

- K. Ni, U.G. Oberlack, M. Obradovic, K. Odgers, I. Ostrovskiy, J. Palacio, M. Pandurovic, B. Pelssers, R. Peres, J. Pienaar, M. Pierre, V. Pizzella, G. Plante, J. Qi, J. Qin, D. Ramírez García, S. E. Reichard, N. Rupp, P. Sanchez-Lucas, J. Santos, G. Sartorelli, D. Schulte, H-C. Schultz-Coulon, H. Schulze Eißing, M. Schumann, L. Scotto Lavina, M. Selvi, P. Shagin, S. Sharma, W. Shen, M. Silva, H. Singen, M. Steidl, S. Stern, D. Subotic, P. Szabo, A. Terliuk, C. Therreau, D. Thers, K. Thieme, F. Toennies, R. Trotta, C.D. Tunnell, K. Valerius, G. Volta, D. Vorkapic, M. Weber, Y. Wei, C. Weinheimer, M. Weiss, D. Wenz, C. Wittweg, J. Wolf, S. Wuestling, M. Wurm, Y. Xing, T. Zhu, Y. Zhu, J. P. Zopounidis, K. Zuber, *submitted*, June 2020.
- "XEMIS2: A liquid xenon detector for small animal medical imaging", L. Gallego Manzano, J.M. Abaline, S. Acounis, N. Beaupère, J.L. Beney, J. Bert, S. Bouvier, P. Briend, J. Butterworth, T. Carlier, H. Chanal, M. Cherel, J-P. Cussonneau, M. Dahoumane, S. Diglio, D. Giovagnoli, J. Idier, F. Kraeber-Bodere, F. Lefevre, O. Lemaire, P. Le Ray, S. Manen, J. Masbou, H. Mathez, E. Morteau, N. Pillet, L. Royer, M. Staempflin, J.S. Stutzmann, R. Vandaele, L. Virone, D. Visvikis, Y. Xing, Y. Zhu and D. Thers, *Nuclear Instruments and Methods in Physics Research Section A: Accelerators, Spectrometers, Detectors and Associated Equipment*, Volume 912, Pages 329-332, December 2018.
 - "Gravity assisted recovery of liquid xenon at large mass flow rates", L. Virone, S. Acounis, N. Beaupère, J-L. Beney, J. Bert, S. Bouvier, P. Briend, J. Butterworth, T. Carlier, M. Chérel, P. Crespi, J-P. Cussonneau, S. Diglio, L. Gallego Manzano, D. Giovagnoli, P-B. Gossiaux, F. Kraeber-Bodéré, P. Le Ray, F. Lefèvre, P. Marty, J. Masbou, E. Morteau, G. Picard, D. Roy, M. Staempflin, J-S. Stutzmann, D. Visvikis, Y. Xing, Y. Zhu and D. Thers, *Nuclear Instruments and Methods in Physics Research Section A: Accelerators, Spectrometers, Detectors and Associated Equipment*, Volume 893, Pages 10-14, November 2018.

Conference proceedings

- "Direct Measurement of Ionization Charges in Single-phase Liquid Xenon Compton Telescope for 3γ Medical Imaging", Y. Xing, M. Abaline, S. Acounis,

- N. Beaupère, J-L. Beney, J. Bert, S. Bouvier, C. Canot, T. Carlier, H. Chanal, M. Cherel, J-P. Cussonneau, S. Diglio, D. Giovagnoli, J. Idier, F. Kraeber-Bodéré, P. Le Ray, F. Lefèvre, S. Manen, J. Masbou, E. Morteau, N. Pillet, D. Roy, L. Royer, J-S. Stutzmann, R. Vandaele, D. Visvikis, Y. Zhu and D. Thers, *2019 IEEE Nuclear Science Symposium and Medical Imaging Conference (NSS/MIC)*, **2019**.
- "XEMIS2: A liquid xenon Compton camera to image small animals", Y. Zhu, S. Acounis, N. Beaupère, J-L. Beney, J. Bert, S. Bouvier, C. Canot, T. Carlier, M. Cherel, J-P. Cussonneau, S. Diglio, D. Giovagnoli, J. Idier, F. Kraeber-Bodéré, P. Le Ray, F. Lefèvre, J. Masbou, E. Morteau, J.S. Stutzmann, D. Thers, D. Visvikis, Y. Xing, *2019 IEEE 20th International Conference on Dielectric Liquids (ICDL)*, **2019**.
 - "Scintillation Signal in XEMIS2, a Liquid Xenon Compton Camera with 3γ Imaging", J. Bert, S. Bouvier, P. Briend, J. Butterworth, T. Carlier, H. Chanal, M. Cherel, J-P. Cussonneau, M. Dahoumane, L. Gallego-Manzano, D. Giovagnoli, J. Idier, F. Kraeber-Bodere, P. Le Ray, F. Lefèvre, O. Lemaire, S. Manen, J. Masbou, H. Mathez, E. Morteau, N. Pillet, D. Roy, L. Royer, M. Staempflin, J.S. Stutzmann, R. Vandaele, L. Virone, D. Visvikis, Y. Xing and D. Thers, *Proceedings of International Conference on Technology and Instrumentation in Particle Physics 2017: Volume 2*, **2018**.
 - "XEMIS: Liquid Xenon Compton Camera for 3γ Imaging", J. Bert, S. Bouvier, P. Briend, J. Butterworth, T. Carlier, H. Chanal, M. Cherel, J-P. Cussonneau, M. Dahoumane, L. Gallego-Manzano, D. Giovagnoli, J. Idier, F. Kraeber-Bodéré, P. Le Ray, F. Lefèvre, O. Lemaire, S. Manen, J. Masbou, H. Mathez, E. Morteau, N. Pillet, D. Roy, L. Royer, M. Staempflin, J.S. Stutzmann, R. Vandaele, L. Virone, D. Visvikis, Y. Zhu and D. Thers, *Proceedings of International Conference on Technology and Instrumentation in Particle Physics 2017: Volume 2*, **2018**.
 - "XEMIS2: Liquid Xenon Medical Imaging System for Small Animal with 3γ Imaging Technique, Y. Xing, M. Abaline, S. Acounis, N. Beaupère, J.L. Beney, J. Bert, S. Bouvier, P. Briend, J. Butterworth, T. Carlier, H. Chanal, M. Cherel, J-P. Cussonneau, M. Dahoumane, S. Diglio, L. Gallego-Manzano, D. Giovagnoli, F. Kraeber-Bodéré, F. Lefèvre, O. Lemaire, P. Ray, S. Manen, J. Masbou, H. Mathez, E. Morteau, N. Pillet, D. Roy, L.

Royer, M. Staempflin, J.S. Stutzmann, R. Vandaele, L. Virone, D. Visvikis, Y. Zhu, D. Thers and J. Idier, *XeSAT 2018*, Sep **2018**, Tokyo, Japan.

- "Scintillation Signal in XEMIS2, a Liquid Xenon Compton Camera with 3γ Imaging Technique", Y. Zhu, M. Abaline, S. Acounis, N. Beaupère, J.L. Beney, J. Bert, S. Bouvier, P. Briend, J. Butterworth, T. Carlier, H. Chanal, M. Cherel, J-P. Cussonneau, M. Dahoumane, L. Gallego-Manzano, D. Giovagnoli, J. Idier, F. Kraeber-Bodere, P. Le Ray, F. Lefèvre, O. Lemaire, S. Manen, J. Masbou, H. Mathez, E. Morteau, N. Pillet, D. Roy, L. Royer, M. Staempflin, J.S. Stutzmann, R. Vandaele, L. Virone, D. Visvikis, Y. Xing and D. Thers in *International Conference on Technology and Instrumentation in Particle Physics*, **2017**.

"XEMIS: Liquid Xenon Compton Camera for 3γ Imaging", Y. Xing, M. Abaline, S. Acounis, N. Beaupère, J.L. Beney, J. Bert, S. Bouvier, P. Briend, J. Butterworth, T. Carlier, H. Chanal, M. Cherel, J-P. Cussonneau, M. Dahoumane, L. Gallego-Manzano, D. Giovagnoli, J. Idier, F. Kraeber-Bodere, P. Le Ray, F. Lefèvre, O. Lemaire, S. Manen, J. Masbou, H. Mathez, E. Morteau, N. Pillet, D. Roy, L. Royer, M. Staempflin, J.S. Stutzmann, R. Vandaele, L. Virone, D. Visvikis, Y. Zhu and D. Thers in *International Conference on Technology and Instrumentation in Particle Physics*, **2017**.

- " 3γ Medical Imaging with a Liquid Xenon Compton Camera and ^{44}Sc Radionuclide", J-P. Cussonneau, J. Abaline, S. Acounis, N. Beaupere, J. Beney, J. Bert, S. Bouvier, P. Briend, J. Butterworth, T. Carlier, H. Chanal, M. Chérel, M. Dahoumane, S. Diglio, L. Gallego-Manzano, D. Giovagnoli, J. Idier, F. Kraeber-Bodere, F. Lefebvre, O. Lemaire, P. Le Ray, S. Manen, J. Masbou, H. Mathez, E. Morteau, N. Pillet, L. Royer, M. Staempflin, J.S. Stutzmann, R. Vandaele, L. Virone, D. Visvikis, Y. Xing, Y. Zhu and D. Thers, *2nd Jagiellonian Symposium on Fundamental and Applied Subatomic Physics, Acta Physica Polonica Series, B 48*, 1661, **2017**.

Oral communications

- "A Novel Image Reconstruction Approach for 3γ Imaging", D. Giovagnoli, A. Bousse, A. Iborra Carreres, T. Merlin, N. Beaupere, J-P. Cussonneau,

-
- C. Canot, S. Diglio, J. Masbou, E. Morteau, Y. Xing, Y. Zhu, D. Thers and D. Visvikis, *IEEE NSS/MIC Manchester*, **2019**.
- *3 gamma Image Reconstruction for XEMIS2 Camera*", D. Giovagnoli, "*De la Molécule aux Matériaux*", *Journee de l'Ecole Doctorale*, Brest, February **2019**.

Titre : Reconstruction d'image pour l'imagerie TEP à trois photons

Mots clés : trois-gammas, cone Compton, reconstruction d'image

Résumé : Dans cette thèse nous présentons l'imagerie trois gammas, où le système d'acquisition repose sur un émetteur bêta+ et gamma. La justification de l'imagerie 3-gamma est que les informations de la détection du troisième gamma peuvent aider à fournir une meilleure localisation du point d'annihilation, permettant ainsi une meilleure qualité d'image et moins de dose délivrée au patient. Nous vous présentons le système 3-gamma XEMIS2, développé à Subatech, Nantes, qui est un détecteur basé sur Liquid Xenon, adapté à l'imagerie 3-gamma grâce à son stopping power, ses caractéristiques de scintillation et sa géométrie continue. Le principe de la reconstruction d'image 3-gamma est basé sur l'intersection d'une LOR, obtenue à partir des photons de coïncidence, avec un cône Compton, déterminé par le troisième gamma. L'idée est de trouver l'intersection du cône et de la LOR et de l'utiliser pour localiser la position d'annihilation la plus probable sur la ligne, comme pour la différence en temps d'arrivée en TOF-PET. Nous présentons une étude de simulation GATE de deux phantoms (NEMA et Digimouse) pour évaluer les améliorations de la reconstruction d'image 3-gamma par rapport à la TEP conventionnelle, et nous étudions aussi la correction du range du positon, qui est important pour notre émetteur Sc44.

Title : Image Reconstruction for Three-gamma PET Imaging

Keywords : Image reconstruction, three-gamma, Compton cone

Abstract: In this thesis we present three-gamma imaging, where the acquisition system relies on a beta+ and gamma emitter. The rationale of 3-gamma imaging is that the third gamma detection information may help to provide better localization of the annihilation point, thus enabling higher image quality and fewer dose delivered to the patient. We present the 3-gamma system, the XEMIS2, developed at Subatech, Nantes, that is a LiquidXenon detector suitable for 3-gamma imaging due to its stopping power, its scintillation characteristics and its continuous geometry. The principle of 3-gamma image reconstruction is based on the intersection of a LOR, obtained from the coincidence photons, with a Compton cone, determined by the third gamma. The idea is to find the LOR\cone intersection and use it to locate the most probable annihilation position on the line, as for the time difference in TOF-PET. We present a complete GATE simulation study of two phantoms (similar-NEMA and Digimouse), to assess the improvements of 3-gamma image reconstruction over conventional PET and we study the positron range correction, which is important for our beta+gamma emitter, Sc44.